JUSTUS-LIEBIG-
UNIVERSITÄT
GIESSEN

Justus-Liebig-University Giessen
Institute of Experimental Physics I

Development of a hollow cathode neutralizer with the new insert material C12A7:2e$^-$ and the corroding effect of the alternative propellant iodine on satellite components

Dissertation to obtain the doctoral degree
Dr. rer. nat.

submitted by
Daniel Zschätzsch

reviewed by
Prof. Dr. Peter J. Klar
Prof. Dr. Hans Leiter

July 10, 2023

Acknowledgments

I would like to express my deepest gratitude to Prof. Dr. Peter J. Klar for having given me this opportunity and for all his extensive support along the way of this journey. I am extremely grateful to the JLU-Ariane Group Graduate School "Radio-frequency ion thrusters" for funding my research position. Additionally, I could not have undertaken this journey without the European Union's Horizon 2020 program, which provided funding in the frame of the Projects NEMESIS and iFact.

I am also thankful to all coauthors of our published papers for the effort they put into the projects. Many thanks to Prof. Dr. Hans Leiter for reviewing my work. Special thanks to Malina Reitemeyer for her constant support in the lab and the fruitful and constructive discussions. Thanks should also got to Limei Chen and Sebastian Benz for their countless measurements. Many thanks to Elisa Monte for designing a lot of great figures for my dissertation and publications. Further, I am thankful to Prof. Dr. Jürgen Janek for his expertise on chemical reactions with iodine and to Christian Altmann for his expertise on hollow cathodes. Additionally, I would like to extend my sincere thanks to of all my current and former coworkers from the ion propulsion group.

Lastly, I would like to acknowledge my family and girlfriend for always believing in me.

Abstract

In recent years, the number of satellites launched into space has exploded. Many of these satellites have electric propulsion systems that run on the common fuel xenon. Xenon is a scarce resource with limited annual production, leading to an unabated increase in the price of xenon per kilogram. Therefore, the transition to alternative propellants is more important than ever. Iodine is one of the most prominent candidates to replace xenon as a propellant in the future. This work addresses the remaining research gaps for the operation of a fully iodine-fueled electric propulsion system and contributes to filling them.

The insert materials of conventional hollow cathode neutralizers e.g. LaB_6 or Ba-doped W are not compatible with iodine as a propellant during operation. An iodine-compatible alternative insert material is the C12A7:$2e^-$ electride of the mayenite C12A7:O^{2-}. In this work, a LaB_6 hollow cathode is modified and thermally optimized for operation with the new insert material C12A7:$2e^-$. The hollow cathode modifications successfully prevent the main problem of melting of the insert during operation. In addition, results are presented describing the material behavior of C12A7:$2e^-$ during operation while revealing other decomposition processes that lower the operating temperature of C12A7:$2e^-$ inserts below the melting temperature.

In addition, the corrosion behavior of various structural materials used on satellites in contact with iodine is investigated. The influence of contact of materials with iodine for both iodine vapors, iodine plasma, and iodine ion beams is investigated. Materials studied include various stainless steels and aluminum alloys, as well as elemental samples such as Ni, Cr, Ta, W, Nb, Mo, Al, Fe, and Ti. Unique to this study is that all sample characterization is performed under space conditions and the samples are treated in iodine atmospheres of varying densities typically found in space. In addition, this work presents an approach to scale the iodine erosion effects as a function of the particular atmospheric conditions and exposure times of up to 10 years.

Zusammenfassung

In den letzten Jahren ist die Zahl der ins All geschossenen Satelliten explosionsartig angestiegen. Viele dieser Satelliten verfügen über einen elektrischen Antrieb, der mit dem gängigen Treibstoff Xenon betrieben wird. Xenon ist eine knappe Ressource mit einer begrenzten Jahresproduktion, was zu einem ungebremsten Anstieg des Xenonpreises pro Kilogramm führt. Daher ist der Übergang zu alternativen Treibstoffen wichtiger denn je. Jod ist einer der prominentesten Kandidaten, um Xenon als Treibstoff in Zukunft zu ersetzen. In dieser Arbeit werden die verbleibenden Forschungslücken für den Betrieb eines vollständig mit Jod betriebenen elektrischen Antriebssystems behandelt und einen Beitrag zu deren schließen geleistet.

Die Insertmaterialien konventioneller Hohlkathodenneutralisatoren z.B. LaB_6 oder Badotiertes W sind im Betrieb nicht kompatibel mit dem Treibstoff Jod. Ein jodkompatibles, alternatives Insertmaterial ist das Elektrid C12A7:$2e^-$ des Mayenits C12A7:O^{2-}. In dieser Arbeit wird eine LaB_6-Hohlkathode modifiziert und thermisch für den Betrieb mit dem neuen Insert-Material C12A7:$2e^-$ optimiert. Die Modifikationen der Hohlkathode verhindern erfolgreich das Hauptproblem des Schmelzens des Inserts während des Betriebs. Darüber hinaus werden Ergebnisse vorgestellt, die das Materialverhalten von C12A7:$2e^-$ während des Betriebs beschreiben und gleichzeitig andere Zersetzungsprozesse aufzeigen, die die Betriebstemperatur von C12A7:$2e^-$-Inserts unter die Schmelztemperatur senken.

Darüber hinaus wird das Korrosionsverhalten diverser Strukturwerkstoffe untersucht, die auf Satelliten in Kontakt mit Jod verwendet werden. Es wird der Einfluss des Kontakts von Materialien mit Jod sowohl für Joddämpfe, Jodplasma als auch Jod-Ionen-strahlen untersucht. Zu den untersuchten Materialien gehören verschiedene rostfreie Stähle und Aluminiumlegierungen sowie elementare Proben wie Ni, Cr, Ta, W, Nb, Mo, Al, Fe und Ti. Einzigartig an dieser Studie ist die Durchführung der gesamten Probencharakterisierung unter Weltraumbedingungen und die Behandlung der Proben in unterschiedlich dichten Jodatmosphären, wie sie typischerweise im Weltraum herrschen. Außerdem wird in dieser Arbeit ein Ansatz zur Skalierung der Jod-Erosionseffekte in Abhängigkeit von den jeweiligen atmosphärischen Bedingungen und Expositionszeiten von bis zu 10 Jahren vorgestellt.

Declaration

I declare that I have completed this dissertation single-handedly without the unauthorized help of a second party and only with the assistance acknowledged therein. I have appropriately acknowledged and cited all text passages that are derived verbatim from or are based on the content of published work of others, and all information relating to verbal communications. I consent to the use of an anti-plagiarism software to check my thesis. I have abided by the principles of good scientific conduct laid down in the charter of the Justus Liebig University Giessen "Satzung der Justus-Liebig-Universität Giessen zur Sicherung guter wissenschaftlicher Praxis" in carrying out the investigations described in the dissertation.

Daniel Zschätzsch

Contents

List of Figures

List of Tables

1 Motivation

Space travel, exploration, utilization, and nowadays exploitation started as a race for prestige between the US and the Soviet Union. Despite the costs, the race produced fascinating new scientific insights and images of our solar system. Besides the space exploration and space travel, the missions quickly developed towards earth observation missions. In the beginning, this development was mainly driven by the military to gather information about the enemy or to use satellites for accurate position determination on earth, i.e., GPS, which started the utilization of space for navigation purposes on ground. Increasing governmental funding, technical advances, and the high interest of the public in space led to an exploding number of space missions and made space accessible for the private sector, generating countless business opportunities. Unfortunately, the high number of satellites brings us to the limit of unregulated space exploitation by blocking orbit altitudes full with space debris. Thus, a responsible handling of space flight is necessary in the future to fully explore the potential of commercial space use.

Today, space flight is indispensable in our daily live. Whether we use a navigation program, check the weather forecast, think about the latest climate change report, or watch the daily news with live broadcasts from all over the world, data from active satellites is omnipresent. Data collection and transmission work only, if a fully functional satellite is at the right spot in the sky, i.e., has the correct position and orientation in orbit. To ensure this, all complex satellites require an active attitude control and a complementary propulsion system. Generally, a satellite's propulsion system can be used for attitude control as well as orbit positioning. The required total velocity change, the thrust magnitude, the available amount of propellant mass, and the time frame of the mission predominately determine the thruster selection.

Electrical propulsion systems have the advantage of very high propellant exhaust velocities, which leads to a very effective usage of the propellant mass. On the downside, the thrust level is low due to a limited mass flow and a restricted electrical power available. This can be compensated by longer operation times of the thruster and the usage of a thruster cluster enabling large mission concepts as planned for the Lunar Gateway mission with 7 thrusters adding up to a 50 kW-class thruster system [1]. Equipping satellites with electric propulsion systems, now has a long history. It has started in 1964 with the first satellite mission SERT-1 (Space Electric Rocket Test). Since then, the number of satellites equipped with an electric propulsion system has constantly increased reaching over 500 in 2019 as shown by Holste et al. [2]. In recent years, Hall effect thrusters (HETs) and gridded ion thrusters are the preferred electric propulsion technologies, also due to their scaling ability, adapting to CubeSats as well as to large satellites such as the mentioned Lunar Gateway. Yet, these types of thrusters are not only used for exploration and demonstration missions, they are also implemented in critical infrastructure such as

telecommunication satellites or on the second generation Galileo satellites providing a European global navigation satellite system (GNSS) [3]. Further, electric propulsion is ready for mass production to provide propulsion for large satellite constellations as seen for OneWeb or Starlink with over 3000 satellites in orbit [4, 5]. Independent of the size of the satellite or type of mission, electric propulsion is increasingly the propulsion system of choice, mainly due to the very efficient usage of propellant by having a good total impulse to mass ratio.

All mentioned missions use electric thruster types, which differ in detail by having different sizes or using electric fields and/or magnetic fields in different ways to generate thrust by a plasma. However, in the end, HETs and gridded ion thrusters are creating thrust by exhausting positively charged ions. Due to a missing ground potential in space, over time, the constant loss of positive charged particles would lead to an excess of negative charge on the spacecraft and bias the satellite negatively. Hence, all these thrusters, despite their individual differences, require a neutralizer to compensate the loss of positive charge by ejecting negatively charged particles, i.e., electrons to compensate the positive ions of the plume. Consequently, the neutralizer has to provide at least the same magnitude of current as the thruster expels for thrust generation. Any further demand on the electron source depends on the thruster type. For instance, a HET requires 5 - 10 times of the electron beam current to generate a sufficient number of collisions inside the plasma [6], leaving the neutralizer with the task to produce electrons in the range from a few ampere up to 100 A [7]. The dominating neutralizer design, which has been used for all flight HETs and gridded ion thrusters so far [8], is the hollow cathode neutralizer, due to its long life and robust performance [6]. The electrons ejected by a hollow cathode originate from the insert, a low work function material and, therefore, an active electron emitter in the shape of a hollow cylinder and, thus, namesake. High temperatures provide sufficient kinetic energy for the electrons inside the material to overcome the low space charge barrier (low due to the low work function) and to leave the surface of the insert material, to be used as neutralization current for the thruster. This effect is amplified by a plasma inside the hollow cylindrical insert, which is generally fueled with the same propellant as the thruster. The minimum required insert temperature depends on the type of insert material. The first tungsten filaments had to be heated to over 2600 K [6], while modern materials such as lanthanum hexaboride (LaB_6) or barium oxide embedded in a tungsten matrix (BaO-W) operate at typical temperatures around 1700 K and 1300 K, respectively [9]. Latest advances across all thruster power classes show the wide range of application of the hollow cathode design and its importance for future missions. Potrivitu et al. [10] developed a hollow cathode for a 200 W-class HET (class of low power thrusters) operating down to a Xe mass flow of 0.1 mg/s, while providing up to 1 A of neutralization current with a total heating power below 35 W. Hollow cathodes can also be implemented in larger thruster concepts as done for the thruster chosen for the new generation of Galileo satellites. The 5 kW HET is equipped with a 20-A hollow cathode [11]. As the available electrical power on satellites increases, even larger thruster concepts ca be imagined, as, for instance, the 100 kW Nested HET developed and tested

in the frame of NASA projects [12]. Such large thruster designs require even more powerful hollow cathodes. Goebel at al. [13] showed that the hollow cathode principle is scalable to high currents by testing a design that provided up to 500 A of discharge current. The high-power cathodes require active cooling of the insert, since the power input given by plasma voltage times discharge current ($P = U \cdot I$) is very high, several kW, due to the high discharge currents. For cathodes in the medium and low power range, the main goal of the structural components is to keep the insert hot, i.e., reducing the heat flow away from the insert. A better thermal design keeps the insert hot and reduces the discharge voltage needed, which in turn lowers the total power consumption. This becomes very important for cathodes implemented in low-power thruster systems because these propulsion systems have very tight power and mass flow constraints. Especially, the cathode must reduce its propellant and power consumption, since it does not provide any thrust and all consumed resources are counted as losses. Consequently, the cathode has to sustain the self-heating mode, i.e., keeping the insert temperature above 1000 °C at low discharge currents (<1.5 A). Thus, a highly sophisticated thermal design is necessary to operate a hollow cathode with low discharge currents and low mass flows. The low power systems become increasingly important as the number of CubeSats equipped with electric propulsion systems increases [14].

As mentioned before, the predominant share of the discharge current originates from the hollow cylindrical insert at the center of the hollow cathode. Consequently, the insert forms the heart of every hollow cathode, surrounded by a support structure. The two commonly used insert materials have preferred fields of application. LaB_6 is especially suitable for high power applications and laboratory work, due to a high melting temperature above 2500 K [15] and high inertness against other gasses [16]. BaO-W has with 2.1 eV a lower work function than LaB_6 with 2.7 eV and, therefore, emits more electrons at lower temperatures [9]. The major downside about operating BaO-W is the additional time consuming tasks of necessary activation procedures as well as ensuring a highly pure propellant, since BaO-W reacts with residual oxygen or water down to a background pressures of partial pressures of 10^{-7} mbar of oxygen, $4{\cdot}10^{-7}$ mbar of water vapor, and $7{\cdot}10^{-6}$ mbar of air [17]. Consequently, BaO-W inserts are favorable for large production quantities with singular qualification procedures or for specific missions relying on a very high efficiency independent of the additional costs during the qualification.

In the end, thermionically emitted electrons from the inner surface of the insert fuel and maintain the plasma and discharge current, while the electron emitting efficiency increases with decreasing power consumption per ampere. Thus, a low plasma and sheath potential is favorable at a constant discharge current ($P = U \cdot I$) as well as low thermal losses due to conductive and radiative heat transfer. An increasing number of electrons injected to the plasma reduces the potentials. Because the electrons are originating from the insert's surface, the quantity of emitted electrons follows the law of Schottky-enhanced thermionic emission. Thus, the emitted current of the insert depends only on the temperature of the emitting surface and its work function. Higher insert temperatures as well as a lower work function lead to higher possible emitting currents. Other design parameters of the hollow cathodes such as orifice diameter or distances have only small effects on the total emitted

current in comparison with the effect of temperature and work function. However, higher temperatures lead to higher heat losses and, therefore, decrease the efficiency. While the temperature adjusts during operation to provide the desired extracted current, the work function is a given and fixed material parameter of the chosen insert material. For both mentioned insert materials, the insert temperature during operation must be above 1000 °C to provide a high enough current per emitting area. These high temperatures require the use of refractory metals such as molybdenum, tantalum, or graphite, which are expensive and difficult to machine. Also, high temperatures encourage reactions with residual gases such as oxygen and the thermal cycles between cold (turned-off) and hot (during operation) produce additional thermal stresses on the structural parts.

Overall, high temperatures are necessary to maintain the electron current, but they also induce many problems such as higher reactivity, thermal stresses, higher power consumption (radiative heat loss scales with T^4), and a lower efficiency. In addition to the general problems with high temperature, the insert materials have their individual limitations. As mentioned before BaO-W is highly reactive towards oxygen and water at high temperatures and LaB_6 has a comparatively low work function, which leads to very high operation temperatures. A sophisticated thermal design, well-adjusted plasma optics, and the usage of very clean propellants can reduce some of the problematic effects and increase the performance by a few percent. However, great performance improvements can only be achieved by using a better insert material that for example has a much lower work function or higher chemical resistance towards oxygen.

The oxygen deficient form of the mayenite C12A7, short for $12\,CaO\ {}^*7\,Al_2O_3$, known as standard material from the cement industry [18], was first reported as electride in the form of C12A7:$2e^-$ in 2003 by Matsuishi et al. [19]. The material is a promising new candidate to be used as insert material due to its unique properties. The first reported work function of the material was as low as 0.6 eV [20], which would have completely revolutionized hollow cathode design. In the beginning of this work, the hope for such a low work function was still present [21, 22]. However, with increasing attention by the cathode community and material researchers, the work function was measured with various measurement techniques, including ultraviolet photoelectron spectroscopy (UPS), photoelectron yield spectroscopy (PYS) [23], photoelectric emission [24], electric-field enhanced thermionic emission [20, 25–27], and simulations based on the density functional theory [28]. A not fully understood surface effect of the electride leads to a wide spread of work function results. Today, the accepted work function is around 2.4 eV [8, 23]. This value was also verified by our research group via electric-field enhanced thermionic emission measurements. The work function is not as low as we hopped for in the beginning; nevertheless, it is still significantly lower than the work function of LaB_6. In terms of operation temperature, this means a reduction by about 300 °C. Additionally, the electride has a high resistance against oxygen contamination (shown in this work), much higher than the insert material BaO-W. This means the electride can be stored over long timespans in air and minor propellant impurities do not destroy the function as insert. Another strong benefit of the electride C12A7:$2e^-$ are the cheap and in large

quantities available base materials Al and Ca. Combined with relatively simple manufacturing methods [29] and high-quality manufacturers in Europe, the insert material makes companies in the EU independent from countries outside of the EU and the costs are expected to be comparable with manufacturing LaB_6 inserts. Some material researchers work on further reducing the work function of the electride to increase its performance. Doping the Ca-Al matrix with other elements such as Sr or Ti yields first successful work function reductions [30, 31]. The low thermal conductivity with about 4.5 W/mK [32] of the electride is in the range of thermal insulators and often considered as great disadvantage of the material. However, a low thermal conductivity of the insert material positively acts as first heat shield and helps to keep the insert at the required emitting temperature even at low extraction currents. This is especially beneficial for low-power thrust applications, since here the main challenge is to keep the cathode hot at low power levels and extraction currents. With such a low thermal conductivity the insert stays hot even without sophisticated thermal design.

The electride as new insert material has many benefits and advantages in comparison to the established materials. In summary, the electride has a low work function, cheap base materials enable sustainable manufacturing in Europe, it possesses a high resistance against oxygen, a low thermal conductivity, and offers the chance of a further reduction of the work function in the future. Despite all benefits, the implementation and successful operation of an electride in a hollow cathode configuration is very challenging. The reason for the difficulties to operate an electride as thermionic emitter is its low melting point of about 1230 °C [33], which is close to the anticipated operation temperature based on the work function. Once having overcome the challenge of melting, the next hurdle for long operations is the decomposition of the C12A7 phase into the phases C5A3 and C3A reported for a temperature of about 1100 °C [34].

In 2010, Rand et al. [35] implemented the electride material in a hollow cathode for the first time and demonstrated tens of minutes of operation at discharge currents up to 3.6 A. In subsequent tests, Rand showed a joint operation of an electride hollow cathode with a hall thruster for 30 min [36] and with an improved cathode design it was possible to reduce the operation temperature below 650 °C at discharge currents below 2 A [37]. Supplied by the Fraunhofer Ceramics Institute (IKTS) with electride insert, Drobny et al. [38, 39] also developed a hollow cathode operating at up to 5 A of discharge current. McDonald and Caruso [40] implemented an electride insert (also provided by the IKTS) into a 20-A class (LaB_6) hollow cathode. At currents of about 150 mA, the cathode operated for over 15 h. Up to now these research groups discontinued operating classic hollow cathodes, due to issues of insert melting. Nonetheless, a detailed thermal analysis was not conducted by any research group addressing the issue of melting. Most recently (2021) Hua et al. [41] achieved an accumulated operation time of 10 h at discharge currents between 0.5 A and 2 A without insert degradation at estimated operation temperatures of 1000 to 1100 ℃.

The first successful implementations of electride inserts into hollow cathodes show the potential of the material in the low power class. Lower temperatures require less input power and increase the area of application. However, achieving operation conditions reliable enough for a satellite still requires additional research efforts and experiments.

Hollow cathodes are favorably operated with the same propellant as the thruster to reduce complexity and weight of the propellant feed system. Consequently, the cathode insert material must be compatible with the predetermined propellant for thruster operation. A widely discussed and around the world laboratory tested propellant is iodine. Iodine is a solid at ambient conditions, but it easily evaporates at elevated temperatures and reaches a sufficient pressure below 100 °C (vapor pressure of 60 mbar at 100 °C) to feed a thruster [42]. Hence, no heavy high-pressure tanks are required to store the propellant as it is necessary for noble gases such as xenon. Storing iodine as solid leads to about a three times higher storage density in comparison with high pressure xenon [43]. This is enormously important for small satellites with very tight mass and volume constraints. The first iodine propelled satellite, a CubeSat, developed by ThrustMe was launched 2020 to space and made use of these advantages. The propellant and propulsion system related costs were 100 times lower for the iodine fueled system than it would have costed flying with xenon [44]. All the benefits of iodine can only be fully explored, if all parts of the satellite survive the operation without failure. Since iodine is highly reactive and can erode many materials, including copper, iron, and aluminum [45, 46], this becomes especially challenging for hollow cathodes that operate at temperatures above 1000 °C and house a plasma. Both circumstances increase the chemical reactivity with iodine and erosion of insert and structural materials by iodine. Up to now, no hollow cathode containing a traditional insert material was able to sustain an operation with iodine for a worth mentioning timespan, which suggests that they might not be compatible with iodine [47, 48]. First laboratory tests at reduced temperatures confirm that C12A7:2e$^-$ is not only resistant against oxygen but also withstands the reactivity of iodine [49]. Hua et al. [50] as well as Rand and Williams [36] report promising first test results of an electride insert implemented into a hollow cathode running for up to 20 h fueled by iodine. The insert inspection after the tests did not show any signs of deterioration. Hence, C12A7:2e$^-$ is a strong candidate for a fully iodine operated electric propulsion system.

Although the insert material of the cathode is a very important element, it is not the only material in contact with iodine. All other structural components of the cathode, thruster, and propellant feed system are also in contact with dense iodine vapor and are subject to chemical reactions and erosion. In the course of iodine fueled thruster developments, this issue is addressed in multiple publications [45, 51–54]. The results show that iodine in fact reacts with all commonly used structural materials, such as aluminum and titanium alloys as well as with stainless steel. It stays unclear, which alloying elements react with the iodine in a space related environment, i.e., in absence of oxygen and water. Further, the effect of lower iodine partial pressures in the direct iodine atmosphere around a satellite whose thrusters operate with iodine, and its influence during long exposure times of a space mission on the components of the satellite are not investigated yet. Since iodine reacts with all common materials, the research question of interest is no longer whether a material is eroded by iodine, but rather how long may this material endure exposure to iodine without loss of structural integrity or the desired function. Figure 1.1 summarizes the current state of research and development of fully iodine-fueled

propulsion systems.

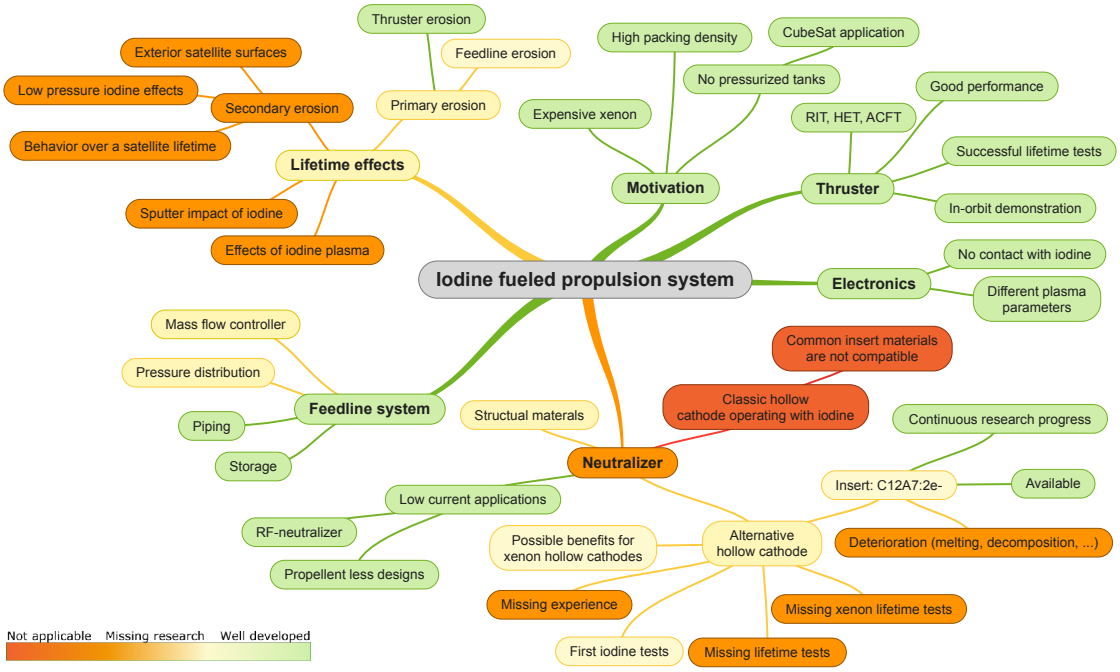

Figure 1.1: Overview showing the current state of research for a fully iodine-fulled propulsion system in a broad perspective from the author's point of view.

This work focuses on further opening the door for a new class of fully fueled iodine propulsion systems by closing research gaps in the reaction and erosion behavior of iodine in contact with different materials in dependence on time and partial pressure. Additionally, a central point is the implementation of the electride C12A7:2e$^-$ into a hollow cathode, which represents a key component to enable fully iodine-fueled electric propulsion systems. The implementation has also the chance to reduce the power, weight, and cost consumption of classic hollow cathodes fueled with xenon.

Since the electride material is obtained from the new European manufacturer Advanced Thermal Devices (ATD), the first part of this work (Section 3) deals with the determination and verification of the material properties. The second part (Section 4) includes the development and testing of a hollow cathode with a LaB_6 insert, followed by the construction of a thermal model to predict the influence of the different material parameters of the electride on the range of operational parameters. Subsequently, the electride is implemented as insert material and tested in of a fully integrated hollow cathode. Finally (also Section 4), the issue of interaction between iodine and structural materials is investigated in relation to iodine partial pressure and exposure time in a mimicked space environment.

2 Theoretical background

2.1 Electric propulsion system

The propulsion system is responsible for accelerating the spacecraft. It includes not only one or multiple thrusters but also the entire support system such as the propellant tank, propellant feedlines, sensors, valves, filters, and power supplies. The thrust generated by classic propulsion systems follows Newton's second law of motion. The change of momentum, i.e., thrust $\vec{F}$, is caused by a mass flow $\dot{m}$ at constant exhaust velocity $\vec{v}_{ex}$:

$$\vec{F} = -\dot{m} \cdot \vec{v}_{ex}. \tag{2.1}$$

Accumulated over an entire satellite mission duration, the total change of momentum, which is an important mission parameter, depends on the total propellant mass, ejected with the actually achieved exhaust velocity. The exhaust velocity is related to the of energy that the thruster transfers to every single atom or molecule of the propellant stream. In combustion rocket engines, the available energy is stored in the chemical bonds of the propellant. Inside the combustion chamber, the chemically stored energy is released via an exothermic reaction, leading to high pressures and high temperatures, i.e., high exhaust velocities. Unfortunately, the maximum achievable exhaust velocity is limited by the energy stored within the propellant. A perfectly configured combustion engine reaches exhaust velocities of a couple of kilometers per second.

The fundamental idea of electric propulsion is the separation of the propellant from the available energy. Electrical power, often collected with solar arrays, is used as energy source to accelerate the propellant flow. For example common ion thrusters use electric and magnetic fields to accelerate an ionized propellant flow and have exhaust velocities above 25 km/s [6]. Thus, much higher exhaust velocities are achieved and less propellant mass must be launched from Earth with the satellite to achieve the same total change of momentum. Electric propulsion covers a wide range of different propulsion systems, which all follow this idea but differ in their architecture and the propellant acceleration technique.

Figure 2.1a shows a schematic of an radio-frequency ion thruster. This type of thruster uses an alternating electric field induced by a coil to generate a plasma. The positively charged ions are extracted by a grid system and used to generate the thrust. The expelled positive charge is compensated by an electron flux from the neutralizer in the same magnitude. The electrons are attracted by the positive potential of the ion beam and voluntarily exit the neutralizer. Since the thruster and the neutralizer are electrically connected to a common potential, an artificial ground potential of a satellite, called secondary star ground (SSG), the electrons and ions leaving the spacecraft self-regulate, match in magnitude of their charges, and neutralize each other.

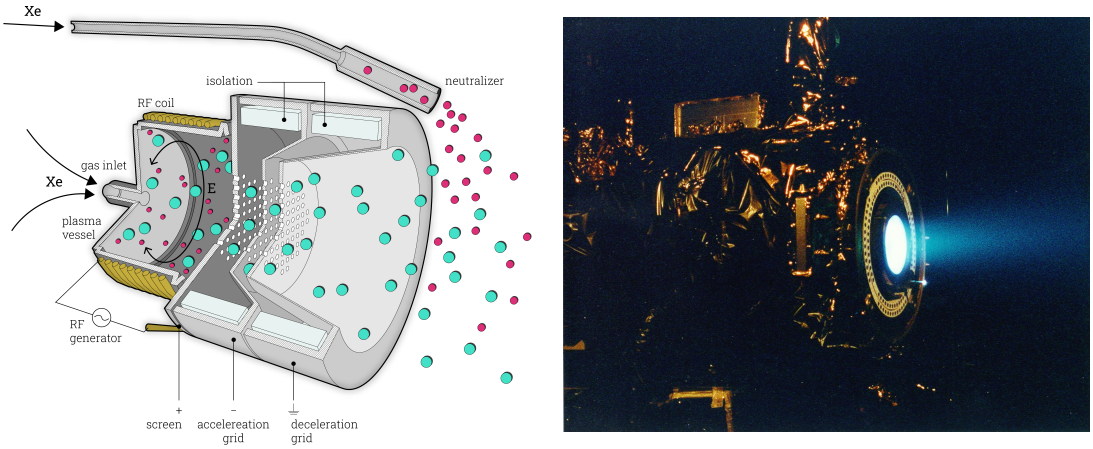

(a) (b)

Figure 2.1: (a) A sketch of a radio-frequency ion thruster (RIT) and a neutralizer in joint operation. (b) The NSTAR ion engine with thruster and neutralizer in joint operation of NASA's primary propulsion system for Deep Space 1 during a hot fire test [image: NASA/JPL[1]].

An ion thruster in operation is shown in Figure 2.1b. The gridded, 30 cm in diameter, and 2.3 kW ion thruster operates together with its neutralizer [55]. The neutralizer can be found as small bright spot below the main ion beam. For this thruster design, the neutralizer's sole task is to provide the electrons for the beam neutralization. Other thruster concepts like Hall effect thruster (HET) require an additional current flow from the neutralizer into the plasma to maintain the latter. Consequently, the neutralizer design strongly depends on the thruster concept and size implemented on the spacecraft.

2.2 Hollow cathode neutralizer

A neutralizer has the primary objective to emit a certain amount of electrons to match the current requirements set by the ion current of the thruster to keep the spacecraft neutrally charged. Some thrusters like a radio-frequency ion thruster (RIT) only need the current equivalent to the thrust generating ions, others like HETs require an additional current to maintain their plasma, which can be five to ten times higher than the extraction current [6]. Consequently, neutralizers or cathodes have to cover a large electron current range to be compatible with the needs of thrusters of either size and type.

An easy and direct way to generate free electrons is via thermionic emission. This describes the effect of bound electrons overcoming the potential barrier of the solid and leaving into free vacuum by thermal excitation. After the electrons have left the hot surface, they can be used as free electrons in plasma generation processes or for neutralization tasks. Early electron emitters were based on tungsten filaments, which had to

[1]NASA and JPL material is not copyright protected and may be used for any purpose [56, 57].

be heated to over 3000 °C to emit the required amount of electrons [6]. However, these emitters cannot provide the current levels required for modern thrusters. Hence, hollow cathode neutralizers were developed.

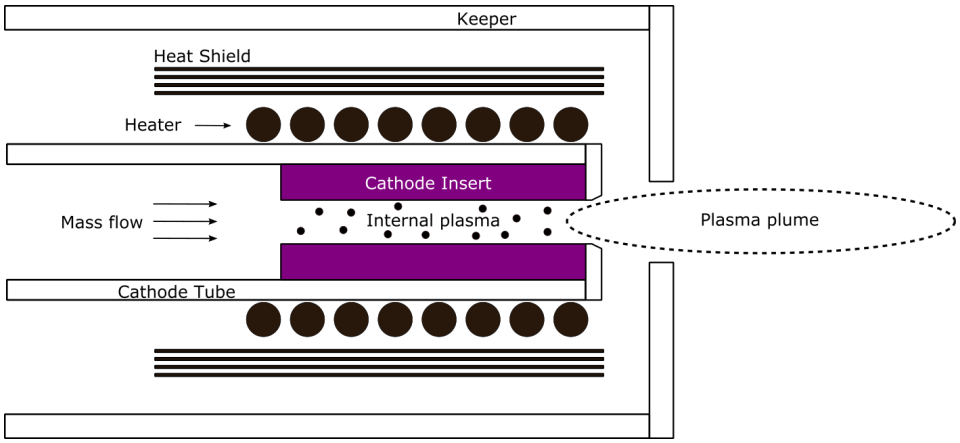

Figure 2.2: A sketch of a hollow cathode neutralizer.

A hollow cathode neutralizer is a specific type of neutralizer where the name refers to its construction. The electron emitting material, also called insert, has the shape of a hollow cylinder, of which the inner surface is the electron emitting surface. A basic sketch of a hollow cathode is shown in Figure 2.2. The insert is surrounded by a support structure, a heater, and a heat shield to keep the insert at emitting temperature. All parts are enclosed by the keeper. During operation a gas, usually the same propellant as used for the thruster, is injected into the hollow cathode, flowing through the hollow insert. The electrons, generated by thermionic emission, collide with the atoms of the propellant gas and ionize them on their way through the orifice towards the positively biased keeper or the positive potential of the anode, i.e., the thruster's ion beam, outside of the cathode. A steady state is maintained by a constant resupply of electrons leaving the emitting surface and a DC plasma establishes. The plasma heats the insert and keeps the emitting surface at a sufficiently high temperature for thermionic emission of the amount of electrons needed to replace those leaving the neutralizer towards the ion beam and keeper. This ensures a self-regulating plasma without external heating. Depending on the selected insert material, the required insert temperature can vary, but it is for all common inserts above 1000 °C (more about inserts in Section 2.2.3). Consequently, all structural materials must be manufactured from refractory materials such as molybdenum, tantalum, boron nitride, high temperature ceramics, or graphite. The surrounding keeper is usually made of graphite, at least for flight models, because graphite has a high sputter threshold and low yield [58], which minimizes the effect of energetic particles and extends the lifetime of the hollow cathode in space. The inner parts are manufactured from other refractory materials. However, some cathodes are successfully manufactured and tested, where all structural components are made out of graphite to reduce the degradation with operation time [59]. By operating a cathode with alter-

native propellants, the selected materials must also be compatible with this propellant at high temperatures, which can get tricky with the highly reactive propellants like iodine.

Independent of the selected materials and implemented design, all hollow cathodes have two major operation phases: the ignition phase, followed by the actual operation phase with the plasma discharge. The ignition phase varies for cathodes with and without implemented heater. For heated cathodes, the ignition starts by establishing a propellant mass flow followed by turning on the implemented heater element that heats the insert to its operation temperature. The gas mixed with an excess amount of electrons, originating from thermionic emission of the hot insert surface, ignites a plasma as soon as an outside positive electrical field is applied. The electrons are driven by the electric field towards its positive biased pole, i.e., keeper, anode, or thruster plume. On their way, the electrons ionize a significant amount of atoms in the propellant gas and a DC plasma establishes. The ignition voltage is in the range of tens of volts for heated cathodes. Heaterless cathodes on the other hand ignite a plasma without previous heating and are frequently investigated and tested but lack a space qualification so far [8]. This cathode type achieves an initial plasma discharge by applying hundreds to thousands of volts to the keeper at room temperature, often supported by a high mass flow, following Paschen's law for breakdown voltages [60]. The resulting high voltage plasma heats the insert to operating temperature; subsequently, the same operation conditions as for heated cathodes are possible.

A hollow cathode reaches the operation phase after the DC plasma is fully developed inside the cathode, the heater, if present, is turned off, and the applied voltages stabilize. The requirements of the thruster dictate the required emitted electron current of the hollow cathode. The maximum possible extraction current I_e is limited by the endurable temperature of the cathode components, because higher currents are accompanied by higher power inputs ($P = R_{Plasma} \cdot I_e^2$). The lower current limit is given by the lowest possible power that is sufficient to keep the insert at its operation temperature. While small thrusters require only currents below 1 A [10], larger satellites equipped with an electric thruster as main propulsion system require usually up to 20 A of neutralization current as, for example, implemented on the new generation of Galileo satellites [11]. As preparation for future missions, NASA tested a hollow cathode up to 500 A of discharge current, which is sufficient to operate a 100 kW HET [13].

In its respective current ranges, which is dictated by the chosen design, a hollow cathode can be operated in diode or triode mode as shown in Figure 2.3. In diode mode, the entire discharge current I_e flows to the keeper (also called standby mode) or entirely towards the anode/thruster with a floating keeper. If the discharge current is split up between keeper and anode, two positively biased electrodes are part of the closed circuit. This mode is called triode mode. The operation phase endures as long as the discharge current can flow to the keeper or anode. Turning of the power supplies for keeper and anode eliminates the necessary potential difference and immediately shuts down the plasma inside the cathode and the insert rapidly cools down. A re-ignition is usually only possible by following the full ignition procedure.

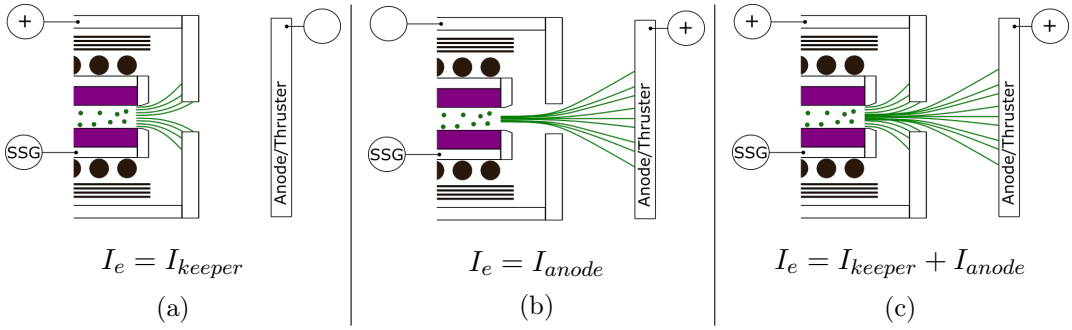

Figure 2.3: The electron stream (in green) is shown for the different operation modes of a hollow cathode: (a) diode mode with keeper, (b) diode mode with anode or thruster, and (c) triode mode with keeper and anode or thruster.

2.2.1 Self-regulating system hollow cathode

Hollow cathodes are operating in a current controlled mode, which means the current is given by the amount of positive ions leaving the thruster and by the preset current limit of the keeper power supply. The current flow starts at the cathode and insert at the reference potential SSG. From here, the current reaches the surface of the emitter material and leaves the surface due to its low work function (ϕ_{wf}) via thermionic emission (see Chapter 2.2.3). Prior to reaching the plasma inside the cathode, the electrons pass through the plasma sheath with a thickness in the order of $10^{-2}\,\mu$m [61], overcoming the potential difference between the cathode (SSG) and the plasma potential. According to the circuitry, the electrons travel through the plasma towards the orifice, exiting the cathode, and reaching keeper or anode potential. The relationship between the resulting voltages in dependence on the discharge current (I_e), material and design parameters is described by a simplified power balance equation for the insert plasma region [6]

$$R \cdot I_e + \phi_S = \frac{H(T)}{I_e} + \frac{5}{2} \cdot \frac{T_{eV}}{e} + \frac{\phi_{wf}}{e}. \tag{2.2}$$

The plasma voltage ($R \cdot I_e$) and the sheath voltage (ϕ_S) are given by the total heat loss rate of the insert in dependence of the insert temperature ($H(T)$) per discharge current (I_e), the electron temperature (T_{eV}), and the work function (ϕ_{wf}). The plasma resistance (R) is given by

$$R = \eta \frac{l}{\pi r^2}. \tag{2.3}$$

The total plasma resistance inside the insert is given by the average conduction length (l), the cross section area (πr^2), and the plasma resistivity (η). The resistivity is inversely proportional to the electron density n_e and the collision time for electrons τ_e including both electron-ion and electron-neutral collisions:

$$\eta \propto \frac{1}{n_e} \cdot \frac{1}{\tau_e}. \tag{2.4}$$

The goal for all hollow cathodes is emitting the required current and needing as little resources as possible. The resources of a propulsion system are propellant mass and electrical power. A lower sheath and plasma voltage directly reduce the consumption of electrical power. Unfortunately, a reduction of the mass flow leads to a lower plasma density inside the insert. Consequently, the plasma resistivity η and, therefore, the plasma resistance R increase, because in Equation 2.4 with the pressure reduction, n_e declines at a higher rate than τ_e increases. With an increase of the plasma resistance, the plasma voltage increases as well and raises the power consumption. Thus, for every cathode design, a compromise between mass flow and power consumption must be made. An approach for reducing the voltages is reducing $H(T)$ by developing a sophisticated thermal design and, therefore, reducing the heat loss rate to a minimum. A low work function ϕ_{wf} significantly increases the cathode's efficiency; however, this value is a material parameter of the insert material and very difficult to influence. The different insert materials and respective work functions are described in Chapter 2.2.3.

Further, Equation 2.2 describes one of the most important properties of the hollow cathode concept. Once the insert reaches its operation temperature and a plasma ignites, the plasma voltage and sheath voltage self adjust to keep the insert temperature constant and provide the demanded discharge current. For example, higher thermal losses would normally decrease the insert temperature but due to the increasing voltage, the heating power increases and keeps the insert at its operation temperature. Increasing the extraction current is accompanied by a voltage drop that reduces the input power per discharge current. The insert temperature stays constant despite the increased discharge current. Only if the discharge current demand exceeds the space charge limited current supply of the emitting surface, the insert temperature rises and provides the demanded current. The self regulating capabilities of the hollow cathode are a major benefit of this concept and a reason for its high reliability.

2.2.2 Orifice sizes and insert heating

The previous section described the behavior of the plasma inside of the hollow cylindrical insert and the influence of the surrounding structure in terms of heat loss once the plasma is ignited. A major influence on the resulting voltages and deposited power has the plasma resistance as well as the electron temperature. Both values mainly depend on the plasma density and, therefore, the neutral gas pressure. The crucial design element for presetting the pressure range of the neutral gas flow is the orifice size. Taunay et al. [62] developed an empirical relationship based on physical quantities to calculate the total pressure (P) inside a hollow cathode (insert region)

$$P(\mathrm{hPa}) = 6.77 \cdot 10^{-8} \, \frac{I_d^{0.30} \, T_g^{0.95} \, \dot{m}_{\mathrm{sccm}}^{0.57} \, L_{0,\mathrm{cm}}^{0.15} \, M_a^{0.45}}{\epsilon_{iz}^{0.20} \, \mu^{0.35} \, d_{c,\mathrm{cm}}^{1.43} \, d_{o,\mathrm{cm}}^{1.71}}, \tag{2.5}$$

where I_d is the discharge current, T_g the gas temperature, $\dot{m}$ the mass flow in sccm, L_0 the orifice length in cm, M_a the atomic mass of the propellant in u, ϵ_{iz} the ionization energy in eV, μ the dynamic viscosity in Pa·s, and d_c and d_o are the insert and orifice diameter,

respectively, in cm. Figure 2.4 shows calculations of the pressure inside the hollow cathode developed in this work based on Equation 2.5. The gas temperature is assumed to be 4800 K and the used gas is xenon. The plots show that operational parameters like discharge current or mass flow can slightly influence the pressure during operation but the largest effect on the pressure has the orifice diameter. A smaller cathode orifice increases the pressure and, consequently, reduces the cathode voltages. As a result, the

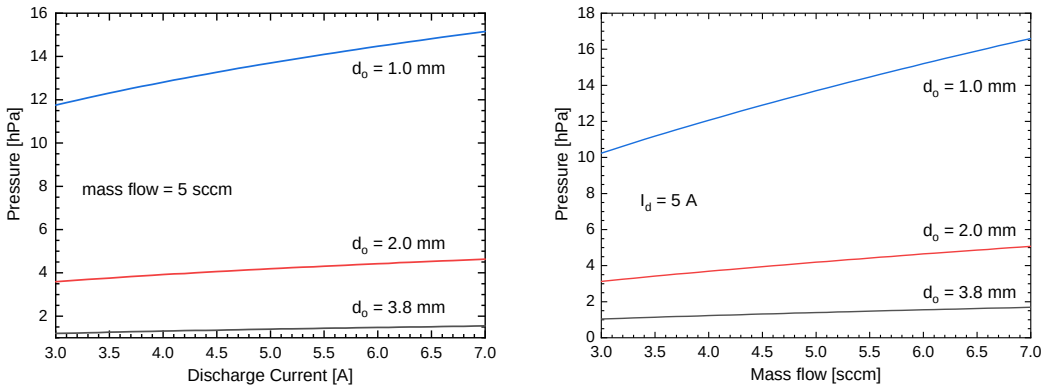

(a) (b)

Figure 2.4: Pressure inside a hollow cathode based on Equation 2.5 in dependence on (a) the discharge current and (b) the mass flow for different orifice sizes and Xe as propellant.

plasma parameters are drastically changed as well, which also influences the operational behavior. Hence, the orifice diameter d changes not only the voltage but also is the design parameter determining the transition from the stable spot mode to the unfavorable, unstable plume mode. As long as the inequation (Equation 2.6) developed by Rehn and Kaufman [63, 64]

$$\frac{J_0 \cdot \sigma\sqrt{W}}{d} \geq 13.9 \cdot 10^{-20}\,(\mathrm{A} \cdot \mathrm{m}^2 \cdot \mathrm{amu}^{0.5}/\mathrm{mm}) \tag{2.6}$$

for inert gas cathodes holds true, the respective cathode can operate in spot mode for a given neutral gas flow J_0 (equivalent neutral current in A, 1 sccm $\hat{=}$ $7.2{\cdot}10^{-2}$A). σ describes the maximum ionization cross section of the neutrals by electrons, while W is the atomic mass of the propellant used. Thus, the upper size of the orifice is limited and must be carefully selected depending on the targeted propellant flow.

Even while staying inside the limitations given by Equation 2.6, the orifice size can still be varied in a large range with respect to the inner diameter of the insert, which has an additional influence on the cathode operation besides the spot to plume mode transition. Goebel and Katz [6] extensively investigated plasma, heating, and operation effects of different orifice sizes. They defined three types of cathode designs. Type A includes all cathodes with very small orifice sizes in comparison to the inner diameter of the insert. Type B cathodes have larger orifices and describe the transition sizes towards

Type C, which has only little or no orifice. Here, the orifice is close or equal to the insert's inner diameter. Thus, Type A cathodes have high internal gas pressures, which decrease for types B and C. Examples for type A and C are shown in Figure 2.5b. As seen in

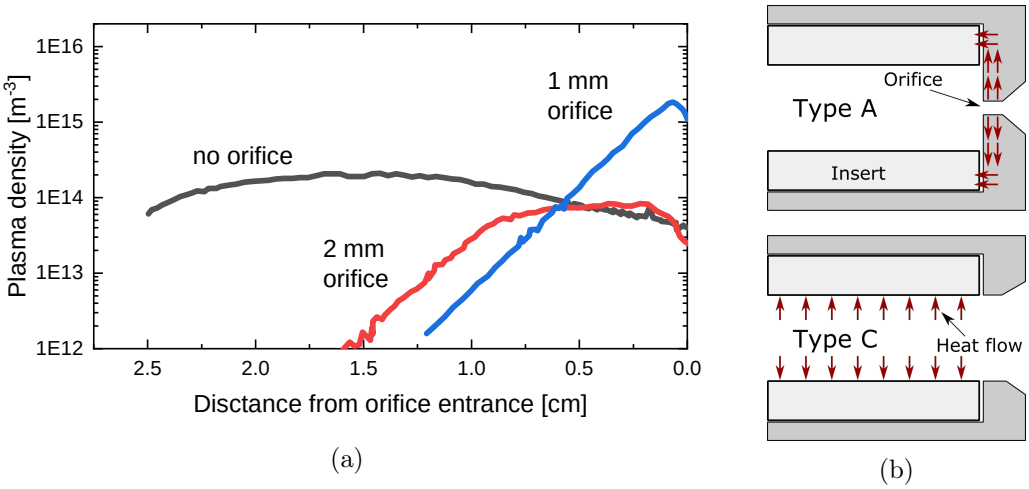

Figure 2.5: a) Plasma density for different orifice sizes at fixed discharge currents and mass flows for a cathode with a 3.8 mm inner insert diameter (data from [65]), b) Type A and C cathode designs with the dominating insert heating mechanism (inspired by [6]).

Figure 2.5a the absolute pressure magnitude increases with smaller orifice size and the plasma density is less evenly distributed. The plasma density and pressure distribution determines the dominant heating mechanism for the insert. Katz et al. [65] described the different heating mechanisms. For small orifice sizes, the plasma density peaks inside the orifice (even denser plasma than shown for the internal plasma) with more than 100 times higher values than for a type C cathode. Due to the small orifice diameter, the entire discharge current and gas must flow through a very small area. Following Equation 2.3, the plasma resistance gets very high causing high resistive heating inside the orifice. Therefore, about 80 % of the entire cathode heating power is generated inside the orifice, which is also responsible for most of the plasma production. To maintain the insert's operation temperature, the heating power must heat the insert; consequently, the heat flows as indicated in Figure 2.5b towards the insert. Thus, a good thermal conductivity of the insert material is required to approach a uniform insert temperature distribution. Cathodes with no orifice (type C cathodes) are heated differently. The equally distributed plasma density causes a low resistive Joule heating inside the plasma. The plasma is generated by electrons accelerated over the sheath potential, which is higher for larger orifice sizes (see Equation 2.2[2]). The insert, in turn, is heated by ion bombardment with ions from the plasma that are accelerated over the sheath potential towards the insert.

[2] A larger orifice decreases the pressure inside the cathode, which in turn deceases R. Since the right term of the equation remains unchanged, ϕ_S must increase to re-balance the equation.

The result is a well distributed heat input over the entire length of the insert.

2.2.3 Thermionic emission and insert materials

The insert is the central part of every hollow cathode because it provides the electrons fueling the plasma and yielding the discharge current. Generally, all electrons with sufficient kinetic energies can leave their host bulk material and can enter the surroundings, i.e., a gas or vacuum. The magnitude of the potential barrier that must be overcome by the electrons is a material specific parameter called work function ϕ_{wf}, commonly measured in eV. The effect is called thermionic emission if the electrons gain their kinetic energy by thermal heating, which is proportional to the material's surface temperature T. The amount of electrons leaving the surface is called emission current J and is quantified by the fundamental equation for field enhanced thermionic emission [66, 67]

$$J = AT^2 \cdot \mathrm{e}^{\frac{-(\phi_{wf}-\Delta\phi)}{\mathrm{k_B}T}}\,[\mathrm{A/m^2}]. \tag{2.7}$$

The base equation is called Richardson–Dushman equation. The $\Delta\phi$ includes the effects of an enhanced electron emission by an electric field. This type of emission is called Schottky emission. A is often referred as Richardson coefficient, which is a material dependent constant and k_B is the Boltzmann constant. An electric field with the strength E at the emission surface (field-enhanced thermionic emission) lowers the potential barrier for the electrons by $\Delta\phi$, given by

$$\Delta\phi = \sqrt{\frac{\mathrm{e}^3 E}{4\pi\epsilon_0}}\,[\mathrm{eV}] \tag{2.8}$$

with the elementary charge e and the dielectric susceptibility ϵ_0. Hollow cathodes often operate with a significant field enhancement if the plasma density is high and the sheath potential becomes significant [6].

The commonly used insert materials are the bulk material lanthanum hexaboride (LaB_6) and the dispenser emitter BaO-W, a tungsten matrix impregnated with barium oxide. The work functions are 2.7 eV and 2.1 eV, respectively [9]. Therefore, BaO-W emits more electrons at lower temperatures than LaB_6 as illustrated in Figure 2.6a. Typical operation temperatures are around 1700 K for LaB_6 and 1300 K for BaO-W [9]. Generally, lower work functions are favorable, because the lower operation temperatures reduce the chance of material failure, increase the life time, and safe power. However, other properties besides the work function are important as well. LaB_6 has a very high melting temperature of above 2500 K [15] and a high inertness against other gases [16]. These properties make LaB_6 ideal for high power applications (high discharge currents) or laboratory work with a higher risk of contaminated propellants. On the other hand, BaO-W has the lower work function, but it is very subsceptible to even low levels of contamination. BaO-W reacts with residual oxygen or water down to a background pressure of partial pressures of 10^{-7} mbar of oxygen, $4{\cdot}10^{-7}$ mbar of water vapor, and $7{\cdot}10^{-6}$ mbar of air [17]. Thus, after every contact to the atmosphere, a BaO-W housing cathode requires a time-consuming activation procedure and needs high purity propellant during operation.

Due to the different strengths and weaknesses of the emitters besides the work function, both insert materials have their own, though overlapping, fields of application.

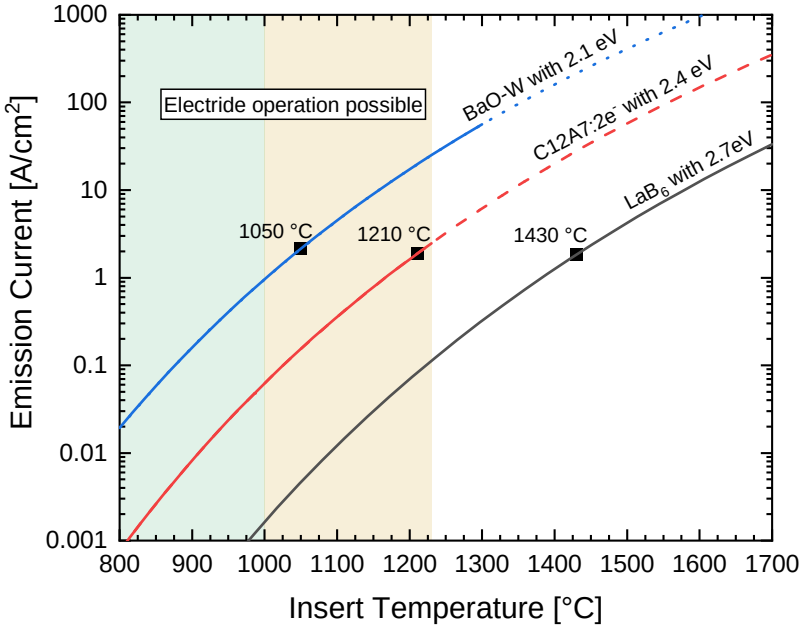

(a)

(b)

Figure 2.6: (a) Thermionic emission current of different insert materials as a function of temperature (Equation 2.7 without electric field) and all with $A = 120\,\mathrm{A/(cm^2K^2)}$. The dashed and dotted lines indicate a theoretical emission beyond material destruction. The electride can safely be operated in the green marked zone. In the yellow zone, deterioration effects have to be monitored closely. (b) two hollow cylinders made of C12A7:2e$^-$ (top) and LaB_6 (bottom).

The electride material C12A7:2e- has a comparable low work function of about 2.4 eV [8, 23] and, therefore, it is a good candidate as insert material. A comparison of the emission currents based on only the work function of the three materials is shown in Figure 2.6a. To provide about $2\,\mathrm{A/cm^2}$, a temperature of 1050 °C, 1210 °C, and 1430 °C is required for the material BaO-W, C12A7:2e-, and LaB_6, respectively. While LaB_6 is basically not limited by the temperature, BaO-W is limited by a maximum insert temperature of about 1300 °C. However, the lifetime of BaO-W drastically reduces at higher operation temperatures (factor 2 with each 40 °C above 1100 °C [6]). The electride is a bulk emitter that is limited by its melting point of about 1230 °C [33]. At operation temperatures above 1000 °C, local temperature peaks can already reach the melting temperature. Additionally, other issues can occur like decomposition of the C12A7 phase into the phases C5A3 and C3A as reported for a temperature of 1100 °C [34]. Despite the temperature limitation challenges, the C12A7:2e- has interesting properties that can

improve and enable cathodes for certain mission scenarios. The low thermal conductivity of 4.5 W/mK [32] drastically reduces the thermal loss rate $H(T)$ in Equation 2.2. Therefore, less thermal shielding is required, the cathode sheath potential decreases, and lower discharge currents are achievable. Additionally, the electride has shown a good resistance against oxygen impurities and it seems to be iodine compatible in contrast to the other two materials [36, 50]. Some researchers even work on further reducing the work function of the electride, which would further increase its performance [30, 31].

The electride C12A7:2e$^-$

The electride C12A7:2e$^-$, first reported in 2003 by Matsuishi et al. [19], is the oxygen deficient form of the mayenite C12A7, short for 12 CaO *7 Al_2O_3 or $Ca_{12}Al_{14}O_{33}$, known as a standard material in the cement industry [18]. The phase diagram of the different calcium aluminates, besides C12A7 also CA, CA2, or C3A, is shown in Figure 2.7a in dependence on the Al_2O_3 concentration. Achieving a pure C12A7 phase is only possible in a very narrow Al_2O_3-concentration and temperature range. The high phase purity is necessary for a good electron emitter material because C12A7 has a unique cage structure as shown in Figure 2.7b. The Al, Ca, and O atoms form a positively charged lattice framework with a cubic unit cell consisting of 24 Ca, 28 Al, and 64 O distributed over 12 cages and a lattice constant of 1.199 nm [29]. Each unit cell is positively charged 4+ and houses two loosely bound O^{2-} ions compensating the positively charged lattice: $[Ca_{24}Al_{28}O_{64}]^{4+}(O^{2-})_2$.

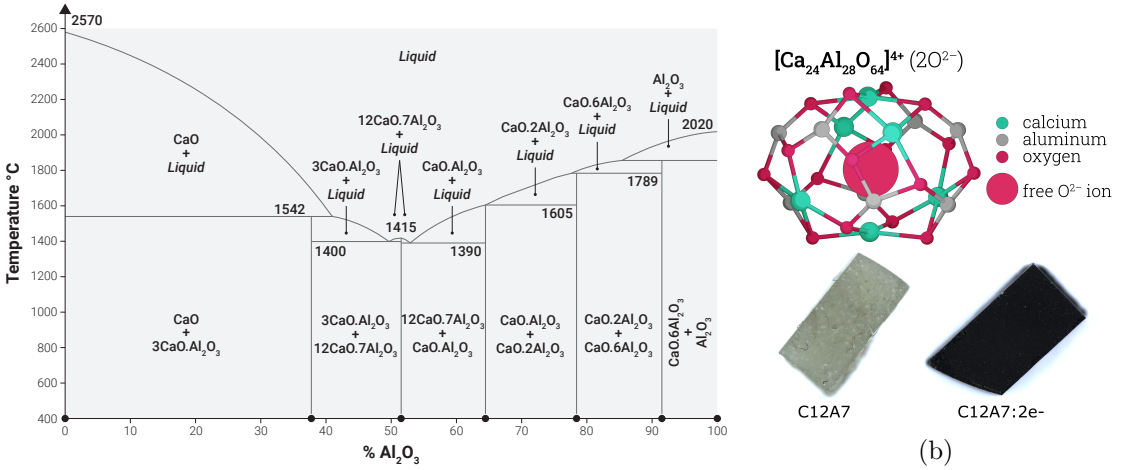

(a) (b)

Figure 2.7: a) Calcium aluminates phase diagram [68]. (b) Cage structure of C12A7 with an unbound oxygen anion [29].

The transformation from the white C12A7 (bottom left in Figure 2.7b) to the black electride C12A7:2e$^-$ (bottom right in Figure 2.7b) is achieved by extracting atomic oxygen from the crystal structure. In an environment with a very low oxygen partial pressure,

the oxygen ions O^{2-}, loosely bound inside the cages, can leave the material as atomic oxygen, leaving two free electrons e^- behind, which can be accumulated inside the cages of the positively charges $[C_{24}Al_{28}O_{64}]^{4+}$ framework. Hence, the chemical formula for the transition from C12A7 to C12A7:2e$^-$ is given by $[Ca_{24}Al_{28}O_{64}]^{4+}(O^{2-})_{2-x}(e^-)_{2x}$ with ($0 \leq x \leq 2$) [69]. Heating the C12A7 in a graphite crucible or in a closed tube together with the metals Ca or Ti leads to an extraction of the oxygen atoms because graphite, Ca, and Ti are much stronger oxygen absorbers at high temperatures than the C12A7 [70, 71]. With increasing extraction of atomic oxygen, the electron concentration increases and, simultaneously, the C12A7 turns green (medium electron concentration) at first and finally black (high electron concentration). Besides the color, other material properties change as well. The thermal conductivity slightly increases to a still low value of 4.5 W/mK, while the electric conductivity changes from values of an insulator to metallic conductivity [32]. By replacing all unbound oxygen ions ($x = 2$), a maximum electron concentration of $2.33 \cdot 10^{21}$ cm^{-3} is achievable. The transition to metallic conductivity appears above $\sim 5 \cdot 10^{20}$ cm^{-3} [72]. For a better readability in the following, all electride samples above the threshold of metallic conductivity are named C12A7:2e$^-$ in disregard of their actual electron concentration. Overall, the electron concentration is a central measure of material quality besides phase purity because it influences important properties such as the electrical conductivity.

As discussed in the previous section, the most important property for an electron emitter is its work function. The first reported work function of the electride was 0.6 eV [20]. However, with increasing attention by the cathode community and material researchers, the work function was measured with various measurement techniques, including ultraviolet photoelectron spectroscopy (UPS), photoelectron yield spectroscopy (PYS) [23], photoelectric effect emission [24], electric field enhanced thermionic emission [20, 25–27], and simulations based on the density functional theory [28]. A not fully understood surface effect of the electride leads to a wide spread of work function results. Today, the accepted work function is around 2.4 eV [8, 23]. This value was also verified by our research group via electric field enhanced thermionic emission measurements on material manufactured by Advanced Thermal Devices (ATD). The Madrid, Spain, based company provided all samples used in this work, if not indicated differently. Nevertheless, some material researchers work on reducing the work function of the electride to increase the performance of the material. Doping the Ca-Al matrix with other elements like Sr or Ti shows first successful work function reductions [30, 31]. This demonstrates the potential of this newly developed emitter material.

2.3 Iodine as alternative propellant for electric propulsion

Iodine is the heaviest stable halogen with the atomic number 53. The seven valance electrons and a relatively high electronegativity lead to the natural state of iodine in form of I_2 (always referred to as iodine) with a total molecular weight of 253.8 u (126.9 u for atomic iodine) [73]. At standard conditions (25 °C, 1 atm), iodine is a purple-black solid as shown in Figure 2.8. However, the high vapor pressure around 0.2 mbar at 20 °C of

iodine causes its sublimation even at room temperature. A decrease in pressure or an increase in temperature quickly leads to a dense, violet iodine vapor. At a temperature of 100 °C, iodine has a vapor pressure of about 60 mbar. The high vapor pressure at moderate temperatures combined with its high molecular weight, low ionization energy, and high availability (low price) are the main reasons for iodine to be considered as alternative propellant to the standard xenon. Xenon is iodine's noble gas neighbor in the

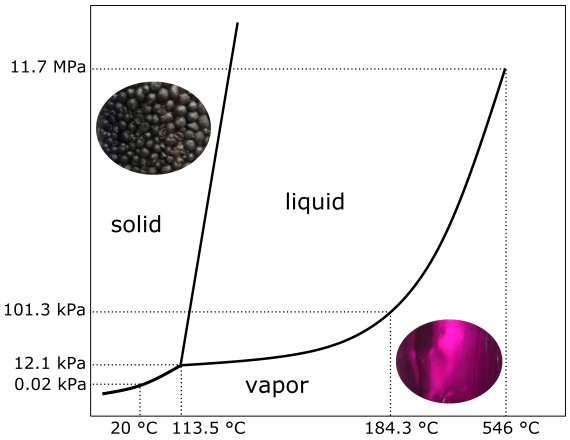

Figure 2.8: The phase diagram for iodine (I_2) with insets showing solid and vaporous iodine. The data points are taken from [73, 74].

periodic table with an atomic number of 54 and a atomic weight around 131 u. It is the heaviest naturally occurring noble gas and gaseous at standard conditions. Therefore, xenon must be stored in high-pressure propellant tanks on the spacecraft. The tanks are heavy and have an additional risk of failure. Iodine on the other hand is solid at standard conditions; hence, no heavy high-pressure tanks are required for storage. Overall, iodine as solid has an about 3 times higher storage density in comparison with high pressure xenon [43]. Furthermore, the price per kilogram is much lower for iodine, which can sum up to 100 times lower costs for the propellant and propulsion system in an iodine fed system compared to a xenon fed system [44].

The challenge, arising with the switching to iodine, is its high chemical reactivity. It reacts with and erodes many commonly used materials such as copper, iron, or aluminum [45, 46]. Although alloys based on aluminum, titanium, or iron have a naturally developed oxide layer protecting their surface from further oxidation, iodine still reacts with these materials [45, 51–54]. In reactions with iodine, water is a catalyst, promoting the reactions with iodine. Thus, when investigating the reaction behavior under space conditions, any contact with water, e.g., humid atmosphere, must be avoided right from the beginning of the iodine exposure up to the final analysis. This has not been consequently done in the studies published so far. Also unclear are the longtime effect of iodine exposure as well as the influence of different iodine partial pressures on the thruster and its surroundings in space. Both issues are addressed in this work.

2.4 Surface characterization methods

Surfaces are the boundary between two environments, e.g., they describe the contact area between a solid and its surrounding atmosphere. This area is of special interest because chemical reactions, sputtering, deposition, absorption, or adsorption takes place at this boundary. In dependence on the depth (where the analysis should take place), the sample material (to be examined), and the interaction phenomenon (to be studied), suitable characterization methods must be chosen. This chapter describes the operating principle of a couple of analyzing tools that are used in this work.

2.4.1 Raman spectroscopy

Solids can be considered a 3D network of bonded atoms, typically with saturated bonds. Such a network consisting of N atoms has $3N$ degrees of freedom, i.e., translation as rigid body (3 times), rotation as rigid body (3 times), and vibration ($3N$-6) as inner degrees of freedom. In Raman-spectroscopy, a monochromatic laser with typical wavelengths of a few hundreds of nanometers interacts with the vibrational degrees of freedom. In the so-called Stokes-Raman process, the inelastic scattering of incoming photons creates additional phonons via a third order process involving absorption and emission of light via interaction with the electronic system as well as interactions between electronic system and lattice. Therefore, the scattered photons have a smaller energy than the incoming ones. The difference in photon energy between incoming laser light and Raman scattered light corresponds to the energy (frequency) of the phonon. During a Raman measurement, a spectrometer records the intensity of the scattered photons and their energies, which reveals the frequencies of the scattered phonons. Such a Raman spectrum serves as a fingerprint of a material. It reflects the bonding structure of the solid and changes to it. Furthermore, it often reveals adsorbed molecules. Thus, Raman spectra before and after a specific sample treatment are indicative for physical adsorption as well as chemical reactions. However, not all vibrational modes of the lattice or a molecule can undergo a Raman process, i.e., are Raman active. Typically, no Raman spectra can be detected in case of metals or unbound molecular iodine.

C12A7 and intermediate phases, e.g., C5A3, C3A, or CA, are well Raman investigated in the literature since they are important for other branches of industry [18, 34, 75]. Raman spectra for the electride form C12A7:2e$^-$ are not reported to a comparable extent [33, 76]. Figure 2.9 shows typical Raman spectra of three different sample types. The top spectrum is typical for all measured C12A7:2e$^-$ samples in the metallic phase. Most characteristic is the double peak structure between 540 cm^{-1} and 640 cm^{-1} (discovered in the course of this work). This structure decreases with the absorption of oxygen and the intensity of the signal at 521 cm^{-1} [18] increases as seen in the middle graph. The bottom spectrum shows an example of an impure C12A7:2e$^-$ sample. Other phases lead to additional, clearly distinguishable Raman signals. The distinct Raman signal around 600 cm^{-1} suggests a dominant phase of C5A3 contaminating the sample [75]. This demonstrates that Raman spectroscopy is indeed a suitable technique to analyze C12A7 upon its phase composition and reduction degree.

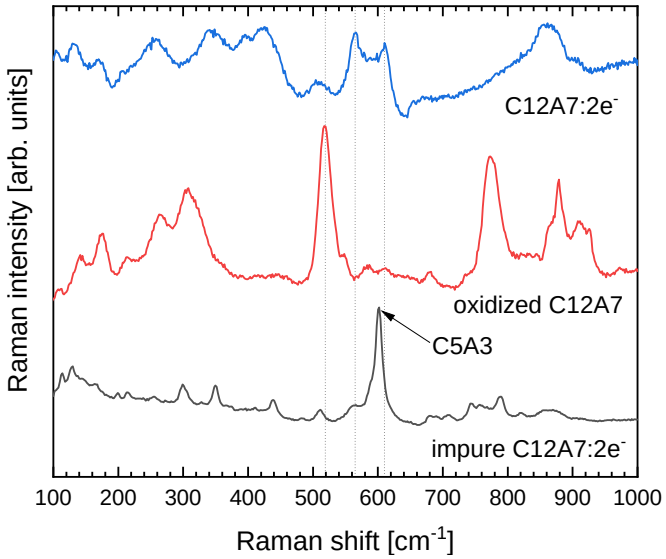

Figure 2.9: Raman spectra of a pristine C12A7:2e$^-$ sample, an impure C12A7:2e$^-$ sample contaminated with other phases, and a C12A7 sample fabricated by oxidation of a pristine C12A7:2e$^-$ sample.

2.4.2 X-ray photoelectron spectroscopy (XPS)

X-ray photoelectron spectroscopy (XPS) yields information about the chemical elements and their charge state (thus, the composition), the electronic structure, and the density of electronic states in a sample. For XPS, x-rays excite electrons residing in core level orbitals. These electrons then leave the sample and are detected by an energy-dispersive detector. The XPS spectra present the intensity of extracted electrons as a function of their kinetic energy. Based on the kinetic energy, the binding energy (characteristic for the atomic core orbital from which the electron originates or the valence band edge) of each electron is determined. The binding energy of an electron to an atomic core state depends on the chemical environment and exhibits an energy shift characteristic to its bonding state. Therefore, the measurement can yield information about chemical states and chemical reactions of the analyzed surface.

XPS is a surface analyzing method limited to surface characterization because of the short mean free path of the electrons excited from the core levels. To collect additional information from deeper layers, a depth profiling can be conducted, which is achieved by argon (Ar) etching. The measurement spot on the sample is sputtered with argon ions (here for up to 240 s and with 1 kV acceleration voltage), which removes the first few atomic layers and enables a measurement of the atomic states below the surface layer up to a depth of a few nanometers (< 10 nm). The charge neutralization is achieved during etching and data collection by compensating the electron loss with electrons from an electron-gun. Samples with a high electrical conductivity do not necessarily require the use of the electron-gun for neutralization.

Two kinds of spectra can be collected: survey or detail spectra, recorded over a wide or a narrow spectral range, respectively. Survey spectra are measured with high pass energies, collecting electrons of larger energy spread simultaneously at the detector. As a result, higher signal intensities are possible but at a low peak resolution. In contrast, the narrow spectra are collected with a lower pass energy, leading to lower intensity levels, but higher resolution resulting in longer measurement times. Individual core level signals must be measured in the narrow range to provide the data basis for correctly analyzing small peak shifts or shape changes. In addition, all recorded spectra need to be referenced during the measurement or afterwards during the evaluation. A common method for post-referencing is referencing the spectrum to the spectral component of the core level C 1s of adventitious carbon at a binding energy of 284.8 eV. Furthermore, the spectra are background corrected, in this work with a Shirley-background. The individual signals are fitted with multiple Voigt-functions to analyze the energy position and area of the core level signals. Signals of metals without chemical bonds are often non-symmetric, requiring an asymmetric fitting function such as a Lorentzian asymmetric line shape.

The composition of the sample can be determined with an uncertainty in the atomic percent range by evaluating the areas beneath the detected core level signals for the respective elements. The relative sensitivity factors (R.S.F) are used to correct the sensitivity of the detector to specific electron energies. For example, the iodine peak I $3d_{5/2}$ yields a strong signal, due to the high detector sensitivity at this energy (619.9 eV). Therefore, the R.S.F for this particular energy level is also large (R.S.F = 7.1). On the other hand, metals like Ti or Fe have a R.S.F. below 0.5, since the detector is far less sensitive at the corresponding electron energies (typically < 500 eV). The detector responds is therefore of major importance when analyzing iodine contaminated surfaces.

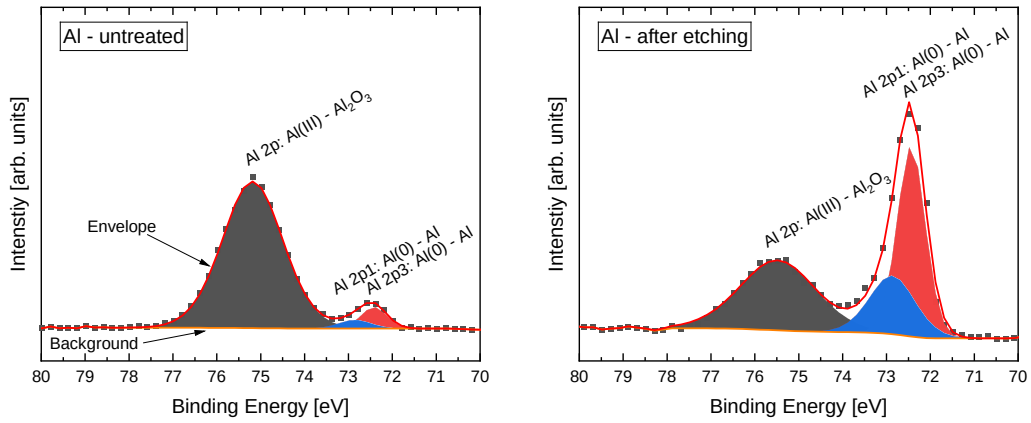

Figure 2.10: XPS spectrum of pure aluminum (purity $> 97.5\,\%$) obtained from an aluminum foil (a) without surface treatment and (b) after 240 s of argon etching.

As an example, Figure 2.10 shows two spectra from the surface of an aluminum foil. The envelope comprises the sum of the fitted functions and should match the course of

the actual measurements. The different colored areas represent the three different fitting functions where each fitting function stands for electrons originating from a specific bond, i.e., a specific energy level. The 2p: Al(III) signal are electrons excited from the 2p orbital of a 3-electron covalent bond as it occurs in Al_2O_3. 2p electrons from similar bonds in other oxides or hydroxides such as $Al(OH)_3$ or AlO(OH) have similar energy levels and can often not be distinguished [77]. However, electrons originating from the same orbital but coming from other bonding structures have a bigger variation of binding energy and can be resolved as individual signals as done for the spin-split doublet $Al\,2p_{1/2}$ and $Al\,2p_{3/2}$. The two signals are assigned to metallic aluminum [77]. Below the measured values, the fitted areas are limited by a Shirley-background. After argon etching (Figure 2.10b), the oxide signal is decreased and the metallic signals are increased, because the etching process removed the first few oxide layers. Often argon etching creates various oxides. For example, a TiO_2 (Ti(IV)-signal) fragments into Ti_2O_3 (Ti(III)-signal), TiO_2 (Ti(II)-signal), and the metallic Ti (Ti(0)-signal) [78]. Thus, the surface chemistry can be changed by etching, i.e., preferential etching in case of compound materials and alloys. Under consideration of these effects, the signal fitting and evaluation must be done thoroughly.

2.4.3 Time-of-flight secondary ion-mass spectrometry (ToF-SIMS)

Secondary ion mass spectrometry (SIMS) is also a surface sensitive characterization method. Raman spectroscopy gently excites virbational modes at the surface or in the bulk of the sample with a laser and measures the shift in photon energy (photons as information carrier). XPS measures electrons excited from the sample with X-ray radiation (electron as information carrier). Instead SIMS uses an ion beam to sputter off material at the surface of the sample, then the atoms or molecules cluster of sputtered material are ionized and detected by mass spectrometry (ions as information carrier). Thus, SIMS is a rather violent measurement technique in comparison with the previous two, but with the ability to detect all elements of the periodic table, distinguishing between different isotopes and detect molecules with a sensitivity in the ppm range [79].

During the ToF-SIMS measurement process used in this work, a primary ion gun shots ions like Ar^+, Ga^+, Cs^+ with an energy in the range of 1 - 30 keV towards the sample. Each single ion bombardment transfers the kinetic energy of the primary ion to the surface region by collisions. The transferred energy causes a collision cascade inside the solid, where some atoms involved in the collisions return back to the surface and cause the emission of atoms or atomic clusters, which are often ionized [80]. The ions originating from the sample surface are called secondary ions, which are detected by a mass spectrometer after passing ion optics to select ions in a defined energy range. Before entering the detector, the ions pass through the time-of-flight (ToF) setup. The additional ToF measurement is important to evaluate the charge-to-mass ratio of the single ions and correctly distinguish between the different elements. A very low primary ion beam current leads to a local extraction of a limited number of atoms or molecules from the top surface layer. This process is called static SIMS and provides a mass spectrum of the surface without damaging it in a practical sense. The dynamic SIMS operates with high beam current, which leads to high sputter rates with a significant material removal from the

surface, to provide information in the depth. The process provides diffusion profiles, mass spectra at different depths, and 3D mass image maps. The achievable depths are in the μm range. Modern instruments use a dual beam ion source enabling static and dynamic measurements with the same instrument.

2.4.4 Profilometer

Classic contact profilometers measure the surface profile by gently touching the surface with a diamond stylus and detecting the vertical displacement of the stylus. By moving the sample relative to the stylus in one direction, the profilometer detects the surface height data along a line, creating a 2D image of the local surface roughness. Here, a DektakXT Stylus Profiler from Bruker company was used. This instrument can achieve a vertical resolution down to 0.1 nm on rather flat surfaces. However, the diameter of the stylus tip (4 – 25 μm) limits the resolution in horizontal direction when scanning across edges with heights in the μm range.

In this work, the profilometer is primarily used to determine sputter effects on sample surfaces by xenon and iodine sputtering. The targeted value is the etch depth developed due to the material removal in the sputtering process. For assessing the etch depth, the surface profile is measured across the transition region from the sputtered to a neighboring area, which still exhibits the pristine surface as it was covered during the ion etching process. The average height difference between these two areas yields the sputter edge height (etch depth).

3 Experimental details

3.1 C12A7:2e$^-$ material characterization

3.1.1 Sputter resistance

It is important to investigate the sputter damage caused by ions inside the hollow cathode because material erosion is the main lifetime limiting factor for inserts made of a bulk material [6]. Inside a hollow cathode the inner surface of the insert is constantly in contact with the plasma. The ions are accelerated over the sheath potential and hit the surface with energies $< 100\,\mathrm{eV}$. LaB_6 inserts have proved to be resilient against sputtering and can be operated for thousands of hours. If the electride possesses a sputter resilience comparable to LaB_6, sputtering should not be an issue in longer operations. Tests with xenon and iodine are conducted because the sputtering yield is also affected by the species of the incoming ions, i.e., by the projectile, and not only by the ion energy.

The sputter tests took place in the test chamber iPott, which has an inner diameter of about 1 m and an inner height of 0.65 m. The chamber is constructed for corrosive gases with special pumps that are designed to pump corrosive gases without being damaged by chemically reactive elements such as iodine. The pumping speed adds up to about 14 000 l/s for xenon and 10 000 l/s for I_2. Prior to the ion exposure, all sample surfaces were polished. Then, the samples were subsequently installed on a sample holder, capable of holding three samples at a time, inside the chamber. The samples were then exposed to an ion beam (see Figure 3.1a). A graphite foil covered half of the sample's surface area facing the ion beam to protect the underlying pristine surface from sputter effects. One of the mounted samples was connected to a multimeter, which measured the ion current hitting the sample. The other two samples were on ground potential to avoid charging effects.

The ion beam (xenon or iodine) sputtered the unprotected area of the different samples and was generated by a sputter source of the type RIM-10, which is based on the RIT-10 technology. It was either operated with 0.37 mg/s of iodine or 0.26 mg/s of xenon. A three-grid ion optics extracts and accelerates the ions from the plasma inside the discharge vessel onto the samples. In addition, the ion optics keeps the beam focused. The ions were extracted with - 200 V from the plasma with a plasma potential of 1500 V. Therefore, the ions hit the samples at an incident angle of about 0° with an energy of about 1500 eV, which is much higher than expected inside hollow cathodes but necessary to see an effect after a reasonable exposure time. The total extracted ion beam current was about 60 mA. A current of about 0.25 $\mathrm{mA/cm^2}$ arrived at the samples. Over a time of 30 - 80 min, the samples accumulated ions in equivalence of 300 – 600 $\mathrm{mAs/cm^2}$. For comparison, the

accumulated current over time (mAs) was kept constant for all samples independent of the gases used, i.e., xenon or iodine, to provide the projectile ions.

For assessing the etch depth after sputtering, a surface profile was recorded across the transition region from the sputtered to the neighboring area, which still exhibits the pristine surface as it was covered during the ion etching process. With a profilometer, the height of the sputter edge is evaluated based on the difference of the average surface height of the protected and unprotected surface.

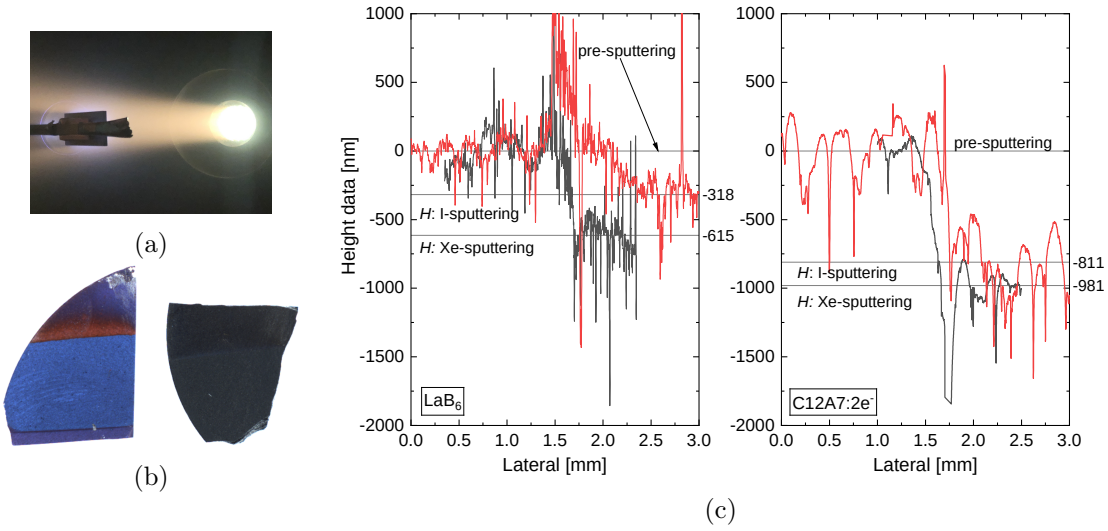

Figure 3.1: (a) Sample holder with samples inside the chamber exposed to an iodine ion current originating from a RIM-10. (b) Images of LaB_6 (left) and C12A7:2e$^-$ (right) after xenon sputtering. The pristine surface is located at the top. (c) Profilometer measurements across of the sputter edge for the samples LaB_6 and C12A7:2e$^-$ sputtered with xenon (in black) and iodine (in red).

Figure 3.1b shows a LaB_6 and an electride sample after their Xe sputter treatment. In both cases the sputtered and protected surfaces are optically distinguishable by a color difference. The sputter edge was measured perpendicular to and across the border line separating the two areas. Each measurement started at the pristine surface and extended towards the lower, sputtered surface as shown in Figure 3.1c. The sputter edge is located at 1.5 to 1.6 mm lateral distance in the plots. The height of the sputter edge H is given by the difference between the average surface height of the pristine and sputtered surface. For LaB_6, H is equal to 615 nm for Xe and 318 nm for the iodine treatment. The measurement of the electride samples gave values of 981 nm and 811 nm, respectively. The sputter damage on a sample is expressed by the sputter yield (γ). which is measured in removed target atoms n_{atom} per projectile ion n_{ions}. As less than 1% of the extracted ions of the RIM-10 are two times positively charged [81], the measured current density X on the sample is directly transformable into an ion area density without correction factor

and by accounting for the sputtering duration t:

$$n_{\text{ions}} \left[\frac{\text{ions}}{\text{cm}^2}\right] = 6.25 \cdot 10^{25} \cdot X \left[\frac{\text{mA}}{\text{cm}^2}\right] \cdot t[\text{s}]. \tag{3.1}$$

The area density of removed atoms of the sample is calculated by using the measurements of the profilometer. The determined height of the sputter edge (H) is multiplied by the density (ρ) and divided by the molar mass (M) of the sample. The result is then multiplied by the Avogadro constant:

$$n_{\text{atoms}} = \frac{H \cdot \rho}{M} \cdot 6.022 \cdot 10^{23} \left[\frac{\text{atoms}}{\text{cm}^2}\right]. \tag{3.2}$$

The sputter yield is then given by the ratio of n_{atoms} and n_{ions}:

$$\gamma = \frac{n_{\text{atoms}}}{n_{\text{ions}}}. \tag{3.3}$$

The sputter yield was calculated with 1.17 for xenon and 0.6 for iodine treatment at the LaB_6 samples, while the electride showed higher sputter yields of 1.99 and 1.64, respectively. In summary, the sputtering effect of iodine is lower than the one of xenon. Hence, sputtering is not an issue if switching to iodine as alternative propellant. LaB_6 is less affected than the electride, which might results in a lower lifetime of an electride inserts in comparison to a LaB_6 insert. However, the sputter yield is in the same order of magnitude for both materials, and it decreases proportional with the energy of incoming ions [82]. Inside a hollow cathode the ions are less energetic ($< 100\,\text{eV}$) and; therefore, sputtering seems not to be a decisive factor limiting the lifetime of the electride. However, in a hollow cathode, the operation temperature is much closer to the melting temperature of the electride, which can increase sputtering and must therefore be investigated separately to accurately predict the lifetime of an electride insert.

3.1.2 Emissivity

The emissivity for every material is very important for space application because the missing atmosphere leaves thermal conductance and thermal radiation as the only means to transport heat. While the thermal conductivity of the electride can be found in multiple publications, the emissivity was not reported so far. However, knowing all material thermal properties is important for accurate thermal modeling. The radiated total thermal power P follows the Stefan-Bolzmann law

$$P = A\epsilon\sigma T^4 \tag{3.4}$$

with A as the emitting surface, σ is the Stefan-Bolzmann constant, and ϵ is the material specific emissivity. The dependence on the temperature to the power of four T^4 causes radiation to be the dominating mechanism of heat loss at high temperatures, as those commonly encountered in operating hollow cathodes. Hence, the emissivity was measured to accurately conduct contact-free temperature measurements and to provide a value for the thermal modeling of the hollow cathode.

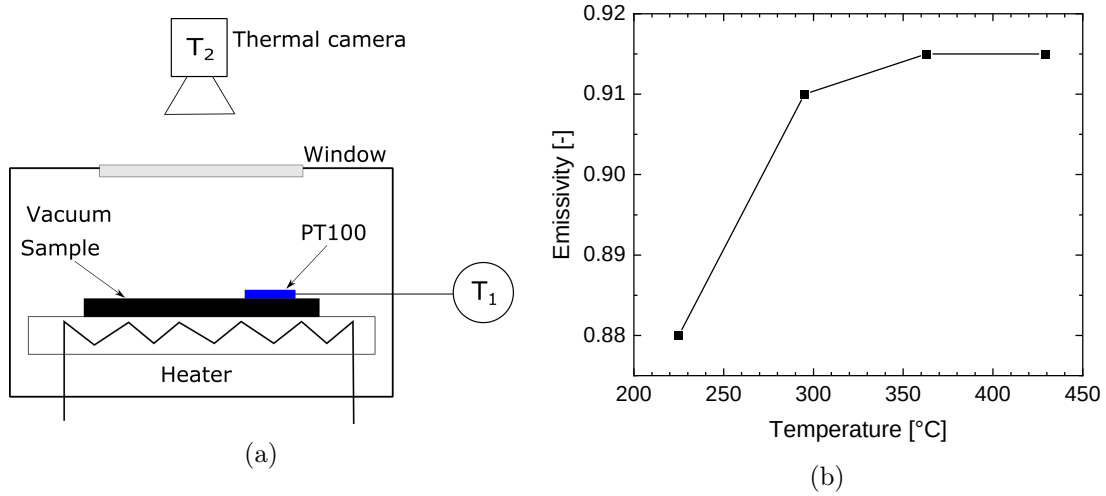

Figure 3.2: (a) A sketch of the experimental setup for measuring the emissivity of the electride. (b) The measured values for the emissivity in dependents on the temperature.

Figure 3.2a shows a sketch of the setup for measuring the emissivity of the electride. The electride sample (shown in black) is placed on a flat heater. The sample is equipped with a PT100 temperature probe, directly measuring the surface temperature T_1. The PT100 is glued to the sample's surface with a ceramic glue (Thermokitt Roth 1100 °C) to achieve a good thermal contact. The heater is located in a vacuum chamber achieving UHV conditions. From outside of the chamber, a thermal camera (TIM 400) also measures the surface temperature of the sample (T_2) through a window via radiation. The emissivity of the sample needs to be known to obtain a correct value of T_2. The camera detects radiation in the spectral range of 7.5 to 13 μm, i.e., infrared radiation. The software of the thermal camera requires the transmission factor of the window and the emissivity of the sample to accurately calculate the surface temperature T_2 based on the detected radiation. The installed window is made of zinc selenide (ZnSe) with a constant transmission factor of 0.68 in the corresponding spectral range of the camera. By adjusting the emissivity in the software to fulfill the assumption $T_1 = T_2$, the emissivity of the electride was evaluated at different temperatures.

The results are shown in Figure 3.2b. The measurements started at 225 °C, lower temperatures are neither relevant for the thermal model nor for radiation heat transport in general. Relevant for the model are the values at higher temperatures; here, the electride has an emissivity between 0.91 and 0.92, which is used in the thermal model. The results are consistent with data provided by the manufacturer.

3.1.3 Resistivity and sample contacting

As described in Section 2.2.3, the electrical conductivity of the C12A7 or C12A7:2e$^-$ mainly depends on the electron concentration and, therefore, on the quality of the man-

ufacturing process. Consequently, measuring the electrical properties yields essential information about the material's state. For the usage in a hollow cathode a high electrical conductivity or rather a low electrical resistivity are desirable to be able to transport the discharge current without significant heat production.

Resistivity measurements are accurately performed with the four-point measurement method. The sample is connected to four wires: two current carrying wires and two voltage sensing wires. A known current flows between the current carrying wires while the voltage drop is measured between the voltage sensing wires. This method provides accurate results even for low resistivity values by reducing the influence of wire and contact resistances. Applying the four-point measurement method to an arbitrary geometry, leads to the measurement method introduced by van der Pauw, which can be applied if the following requirements are fulfilled [83]:

1. The sample must have a flat shape of uniform thickness - 2D.
2. The sample must not have any isolated holes.
3. The sample must be homogeneous and isotropic.
4. All four contacts must be located at the edges of the sample.

The four contacts are numbered counterclockwise from 1 to 4. A complete set of measurements includes at least two measurements where the contacts are subsequently used for setting the current flow and measuring the voltage drop. Thus, an average resistivity ρ is measured, given in $[\Omega \cdot \mathrm{m}]$. The measurement technique is also commonly used for Hall-measurements to determine the carrier concentration and mobility. However, important for all kind of electrical measurements is a good electrical contact between the sensing wires and the sample's surface. Because of the porous surface of the C12A7 in addition

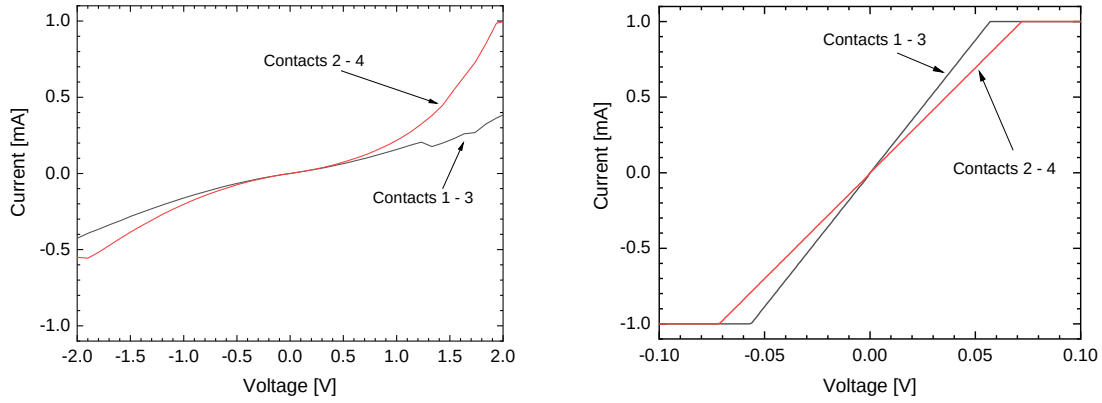

(a) (b)

Figure 3.3: Electrical contact check of an electride sample contacted via (a) contacting-silver or (b) sputtered platinum.

to an insulating surface layer, proper contacting of the sample becomes fundamental for

an accurate measurement of the intrinsic resistivity. A common method for contacting semiconductors is the usage of contacting-silver paint. Small drops of dissolved silver are planted on the samples surface. While the solvent evaporates, the silver stays behind and creates a thin surface layer with a good contact to the sample. Contacting the patches of contacting-silver were either achieved by special sample holders with screws touching the silver on the side (Figure 3.4a) or by attaching small cooper wires directly to the silver patches with super glue (Figure 3.4b). Once well adjusted, the resistivity measurements were rarely successful because both systems are very fragile, and the contacting silver generally did not overcome the insulating surface layer of the electride. This became apparent during the contact check measurements that did not show the expected linear current-voltage characteristics and the measured current levels were very low (shown in Figure 3.3a). Additionally, the super glue and the mounting mask were not temperature stable, which precludes measurements above or below room temperature. Trying to prepare contacts with contacting-platinum paint as alternative did not result in better contacts on the sample. The working principle of contacting-platinum paint is basically

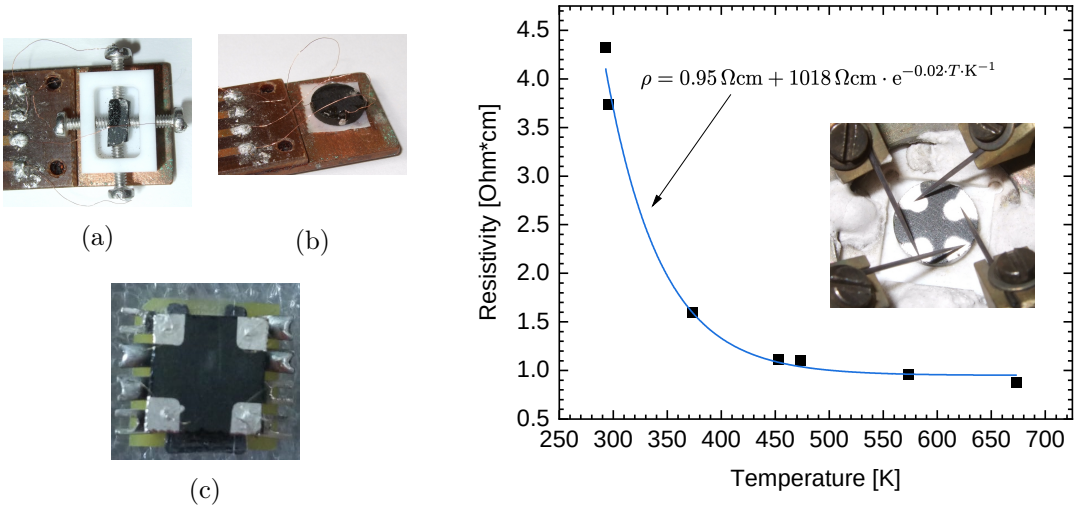

Figure 3.4: Images of differently contacted samples: (a) contacting-silver paint contacted with screws, (b) contacting-silver paint contacted with copper wires attached with super glue, and (c) platinum sputtered contact areas. (d) Temperature T dependent resistivity ρ of a C12A7:2e$^-$ sample manufactured by Fraunhofer IFAM in Dresden (fit according to Equation 3.5). The inset shows the contacted sample mounted to the measuring instrument. Contacts achieved with sputtered platinum.

the same as for contacting-silver paint, a metal solved in a solvent. Here, the solvent does not evaporate at room temperature and must be tempered. The electride requires vacuum conditions during tempering. In this environment, no good contacts were obtained, because the evaporating solvent evaporated to fast and transported the platinum away from

the sample. Thus, after the tempering no platinum was detected on the sample. Testing larger drops of contacting-platinum resulted in blurring of the drops during tempering, creating a fully covered surface. The switch to platinum sputtering for depositing contact areas solved the contacting issue. The sample was covered by a mask protecting the surface from platinum sputtering leaving out four small areas. The first sputtered sample is shown in the inset of Figure 3.4d. The areas are still quite large, but the contacts were very good without any nonlinearities (shown in Figure 3.3b). A result of the final coating procedure is shown in Figure 3.4c. The well-confined platinum surfaces promise good electrical measurements.

Figure 3.4d shows resistivity measurements for the electride sample shown in the inset. The measured resistivity at room-temperature agrees with other published results [70, 84]. The exponentially decreasing resistivity ρ with increasing temperature T follows the typical trend for the intrinsic resistivity of non-doped semiconductors in the form of [85]:

$$\rho = \rho_\infty + \rho_0 \cdot \mathrm{e}^{-\alpha T}. \tag{3.5}$$

The measured sample did not show a hysteresis of the measured resistivity for a increasing or decreasing temperature. Hence, the high temperatures in vacuum did not change the platinum contacts nor the sample structure or reduction state. Subsequent studies, measuring the electron density and resistivity via Hall-measurement for various samples of different reduction levels, are successfully building on this approach of contact fabrication by platinum sputter deposition.

3.1.4 Electron concentration via gravimetry (oxidation Part 1)

The electride C12A7:2e$^-$ absorbs oxygen and turns into mayenite C12A7 at high temperatures in an oxygen-rich environment, losing its thermionic emission properties. Since oxygen atoms are heavier than the electrons that they replace in the electride, the samples gain weight with increasing degree of oxidation. In order to use the weight gain to determine the degree of oxidation and electron concentration, all samples were weighed prior and after each heating interval with a Sartorius Supermicro scale (sensitivity 0.0001 mg). Subsequently, the weight difference was used to determine the rate of oxidation in relation to different atmospheric conditions. The final and maximum weight was then used to calculate the total electron concentration of the pristine electride material. The relative weight difference between C12A7 and fully reduced C12A7:2e$^-$ is 1.17 %.

Table 3.1 provides an overview of the different electride samples used and their oxygen exposure conditions. All samples were fabricated by Advanced Thermal Devices (ATD) in Spain. The sets of experiments under air and at ambient pressure were conducted with type C and type A.2 samples in a Nabertherm oven, which can realize temperatures between 30 °C and 3000 °C. The samples were placed in the preheated oven at a constant temperature in the range between 75 °C - 800 °C. The annealing duration varied from a few minutes (at the highest temperature) up to 14 hours at 75 °C.

The oxygen-exposure experiments at reduced oxygen pressure were performed in the vacuum chamber LEIKA, which is equipped with a pre-vacuum pump, a turbomolecular pump, a mass flow controller (MFC) and a heater stage from Tectra company. The

Table 3.1: Overview of the electride samples used in the oxidation experiments with information about size, weight, and key parameters of the oxygen exposure.

Sample Type	Dimensions	Weight Range	Exposure Condition
Type C	No specific shape	506 mg - 1 271 mg	500 °C - 800 °C in air
Type A.1	(6x3x2) mm^3	80 ± 10 mg	700 °C, $P_{O_2} = 0.1$ mbar
Type A.2	$\frac{1}{4}$ circle (r=13 mm)	489 mg - 725 mg	a) 75 °C - 800 °C in air b) 700 °C, $P_{O_2} =$ 9e-4 mbar

pumping system achieves a base pressure below 10^{-7} mbar, while the heater can heat up to 1600 °C in less than 20 seconds. The MFC can provide a maximum mass flow of 10 sccm of oxygen. This corresponds to a pure oxygen atmosphere inside the chamber of $9{\cdot}10^{-4}$ mbar or 0.1 mbar with and without operating turbomolecular pump, respectively. The samples were placed on the heater and after reaching the base pressure they were heated up to 700 °C before starting the oxygen flow. The oxygen flow was stopped after reaching the desired exposure time (1 - 10 min) and the interior atmosphere returned to its base pressure. Additionally, the samples were kept at the desired annealing temperature for an extra of 10 min without oxygen flow to achieve a homogeneous oxidation.

The mass gain of each sample was determined by weighing before and after a heating interval and is measured in percentage weight gain per exposure time: %/minute. Therefore, the oxygen uptake of the samples can be compared despite their different sizes and masses. The conversion to electron concentration of the pristine sample is done assuming to have a fully oxidized sample when no more weight increase is detected. This final weight corresponds to a reduction level of 0 % and an electron concentration of $n_e < 10^{16}\,cm^{-3}$, while a fully reduced sample has a reduction level of 100 % ($n_e = 2.33{\cdot}10^{21}\,cm^{-3}$). The reduction level of the samples investigated lies between these two values and was calculated based on Equation 3.6,

$$X = \frac{M(t) - M_{ox}}{M_{red} - M_{ox}} * 100 \tag{3.6}$$

where X represents the level of reduction in % and $M(t)$ is the actual weight of the sample at exposure time t. M_{ox} is the weight of the fully oxidized sample and M_{red} is the theoretical weight of a fully reduced sample (reduction level of 100 %). According to Equation 3.6 and the oxidation experiments, the type C samples have an initial level of reduction of about 39 % ($n_e = 9{\cdot}10^{20}\,cm^{-3}$) and the type A samples of about 24 % ($n_e = 5.5{\cdot}10^{20}\,cm^{-3}$). All hollow cathode inserts were manufactured from the type C material, the material with the higher electron concentration.

3.1.5 Oxidation behavior (oxidation Part 2)

The electride changes its color from black via green to white/grey depending on the electron concentration [29]. This behavior serves as a first qualitative reference point

when assessing the oxidation state of the sample. Figures 3.5a and 3.5b show the two samples (an A.2 and a C type sample) at an intermediate oxidation state after annealing in air. The samples oxidized very unevenly, as indicated by the variation of color. Figure 3.5c shows a fully oxidized sample with the typical color of C12A7. The samples treated with 0.1 mbar of oxygen atmosphere (not shown) did not show this behavior; thus, they presumably oxidized evenly. A detailed description of the different treatment condition are given in the previous section, Section 3.1.4, and Table 3.1.

(a) (b) (c)

Figure 3.5: (a) type A.2 and (b) type C sample partially oxidized in air. (c) type C sample fully oxidized in air.

Nevertheless, before reaching oxygen saturation, the oxidation rate of the electride at a fixed temperature is almost constant, i.e., the weight increases almost linearly with exposure time. This behavior is independent of the oxygen partial pressure as it is shown in Figure 3.6a for air and in Figure 3.6b for $P_{O_2} = 0.1$ mbar. At 800 °C in air (Figure 3.6a), the sample is fully oxidized after about 50 minutes. No more electrons can be replaced by oxygen anions and the material has turned into C12A7. The oxygen incorporation rate decreases significantly with the temperature, but the oxygen intake is approximately linear for a constant temperature before saturation is reached. The reduction level is calculated with Equation 3.6.

Figure 3.6b shows the correlation between weight gain and level of reduction at 700 °C and 0.1 mbar oxygen pressure. Both behave linearly with time. Here, the sample gained weight at a rate of about $1.8{\cdot}10^{-2}$ %/min, which is in the same order of magnitude as the rate for the oxidation in air at 700 °C ($1.1{\cdot}10^{-2}$ %/min). The temperature measurement in the LEIKA chamber is not as accurate as in the Nabertherm oven and the temperature in the LEIKA experiment was somewhat higher than the nominal 700 °C. This can explain the slightly higher oxidation value in the 0.1 mbar oxygen atmosphere. Furthermore, the ratio of surface area to volume can influence the oxidation speed. Three samples of the types A.1 and A.2 (see Table 3.1) were exposed to an oxygen pressure of 9e-4 mbar at 700 °C for more than 1 hour each. No increase in weight was detected for any of those samples.

In Figure 3.7, the rate of weight gain R is plotted versus the annealing temperature T_{an} used. The rate of weight gain was extracted from the linear part of the oxidation

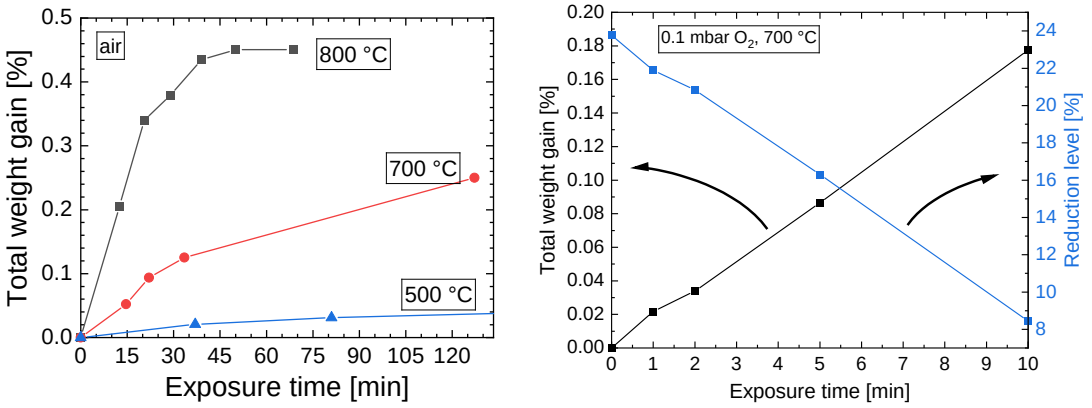

(a) (b)

Figure 3.6: (a) The total weight gain of type C samples as a function of exposure time for various temperatures in air. (b) Linear behavior of the total weight increase (black curve) and linear decrease of the reduction level (blue curve) with time of an electride sample (type A.1) at a constant temperature of 700 °C and an oxygen pressure of 0.1 mbar.

curve vs exposure time for each annealing temperature. The plot reveals an almost exponential dependence of the rate of weight gain on the annealing temperature. The sample's weight increased with about $3{\cdot}10^{-2}$ %/min at 800 °C, while it increased only with about $7{\cdot}10^{-5}$ %/min at 400 °C. The uncertainty is larger for measurements at higher temperatures because during the rather short temperature exposure times (down to 90 seconds), the heat up time from room temperature of the sample, after being inserted into the oven, becomes significant. In these cases, the heating-up time of the sample influences the oxidation rate, especially since the electride has a very low thermal conductivity and a high heat capacity [32]. Furthermore, two samples were treated in air at 75 °C for about 14 hours. None of those exhibited a detectable weight increase; therefore, this temperature was not sufficient to oxidize the electride in the given time frame. In addition, one type A.2 sample was kept at room temperature in air for 252 days. Its weight increased by 0.009 mg or 1.4e-3 %. This finding does not allow a conclusive statement about the oxidation process at room temperature. However, other measurements of long stored electride samples and other publications [23] indicate no deterioration of the material in air at ambient conditions.

All electride samples studied exhibited a non-conductive surface layer at the end of the fabrication procedure. Measured with a multimeter, the resistance between two points on the samples surface (distance of about 25 mm) was in the order of tens to hundreds of megohms. After several heating cycles in vacuum, the surface showed a good conductivity again in the order of a few ohms. Each heating cycle in vacuum comprised an exposure of the sample to temperatures between 600 °C and 800 °C for several hours. Raman spectra did not reveal a difference between samples with a non-conducting and a highly conducting

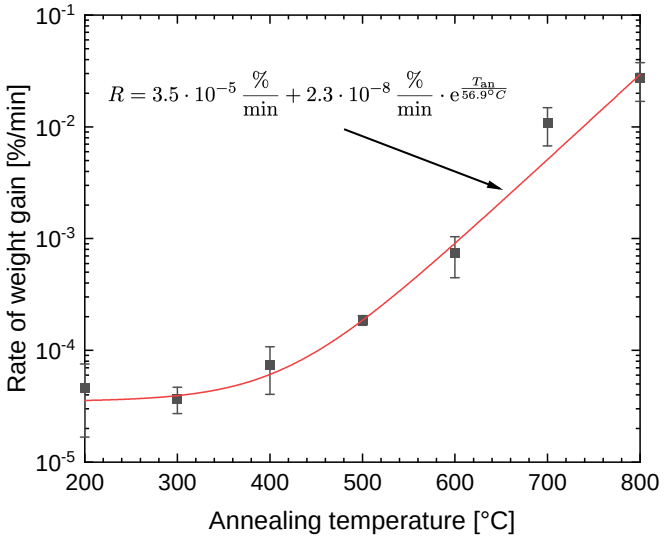

Figure 3.7: Rate of weight gain R in dependence on annealing temperature T_{an}. The oxidation rate is calculated from the linear section of the oxidation curve versus exposure time for each annealing temperature (see figures 3.6a and 3.6b).

surface, meaning that the insulating surface layer is rather thin. Two explanations seem reasonable. First, the non-conducting layer may be caused by the mechanical cutting of the sample, leaving a somewhat amorphous layer on the surface, which is cured during heat cycling. A second possible explanation is that a very thin oxide surface layer forms at room temperature. The heating in vacuum reduces the oxygen at the surface and the conductivity of the bulk material develops at the surface. A combination of both processes is also possible. However, the surface, once heat cycled, kept its good conductivity in air under ambient conditions at least for a few weeks (measured with a portable multimeter).

In summary, the electride started to gain weight at a temperature of 200 °C (no oxidation occurred at 75 °C) and increased its weight linearly with exposure time in the electron-rich regime prior to a saturation of the weight gain when approaching mayenite, i.e., having exchanged all free electrons for interstitial oxygen anions. The rate of weight gain depends exponentially on the temperature and is independent of the partial pressure of oxygen in the annealing process. Only at very low partial pressures ($9{\cdot}10^{-4}$ mbar) no oxidation was detected. The patchy color change (black to green and white) of the samples indicated a very uneven oxidation behavior in air. Nevertheless, the electride does not oxidize at room temperature, which may be due to a thin oxidized surface layer serving as protection to the bulk of the material. Overall, the electride is very resilient to oxygen. Even at high temperatures, the electride requires time and a relatively high oxygen partial pressure (in terms of conditions typical for vacuum chambers) to incorporate oxygen and to lose its unique properties. Hence, small amounts of oxygen impurities in the propellant flow should not result in a deterioration of the insert. Therefore, no

instant destruction of electride inserts should occur in case of an accident, contrary to inserts made of BaO.

3.1.6 Electron concentration determination by Raman spectroscopy (oxidation Part 3)

The determination of the level of reduction via weight gain is a simple and effective method (see Section 3.1.4). However, the technique requires the transformation of the electride into mayenite; thus, it destroys the electride. Therefore, a non-invasive method for assessing the free-electron concentration of the electride is desirable. Such a method may be presented by Raman spectroscopy, which can be used to probe the lattice vibrations of crystalline samples. In 2011, Kim *et al.* [33] reported a peak in the Raman spectrum of the electride, which varies with the level of oxidation of the sample and, thus, also with the free-electron concentration. The peak starts to appear in the Raman spectra of samples with a free-electron concentration of about $10^{20}\,\mathrm{cm}^{-3}$ and its intensity increases with increasing electron concentration. The peak is located at a Raman shift of $186\,\mathrm{cm}^{-1}$ and, according to Kim *et al.*, describes the vibration of cages containing trapped electrons [33]. It was not possible to validate the correlation between the intensity of this signal at $186\,\mathrm{cm}^{-1}$ and the electron concentration as given in the literature.

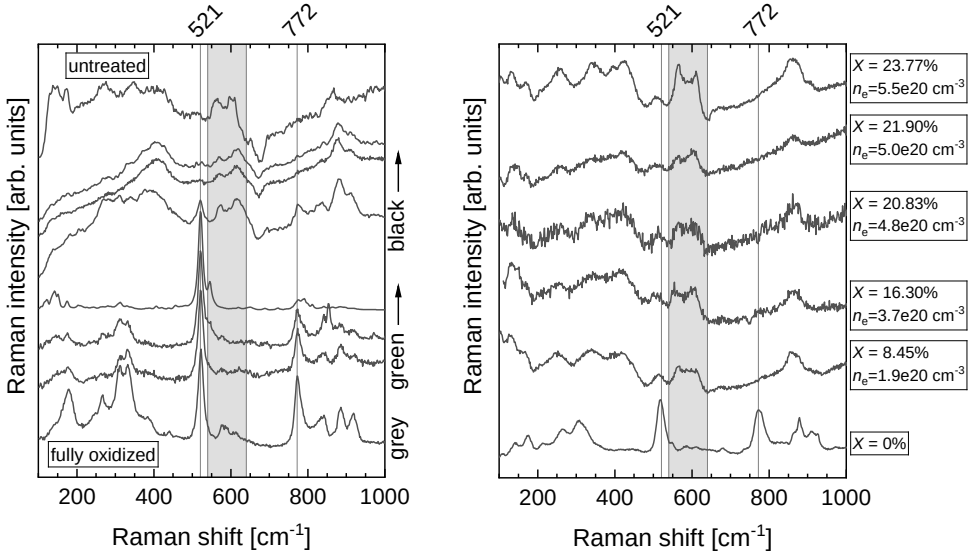

Figure 3.8: (a) Raman spectra (laser excitation wavelength $\lambda = 488\,\mathrm{nm}$) obtained from electride samples (type C, Table 3.1) treated in air. The surface color of the measurement spot is indicated. The top spectrum corresponds to the highest electron concentration and the lowest spectrum to the lowest electron concentration. (b) Raman spectra (laser excitation wavelength $\lambda = 514\,\mathrm{nm}$) of electride samples with the given electron concentrations.

Figure 3.8a shows Raman spectra of the unevenly oxidized samples of type C (refer to Section 3.1.4 and Figure 3.5). The spectra are sorted according to the surface color of the measured spot on the samples. The spectra shown at the bottom are taken from grey and greenish sample areas as well as from fully oxidized, white sample areas (Figure 3.5c). The spectra located on the top were obtained from black areas and an untreated electride sample (spectrum on the very the top). The degree of oxidation increases towards the lower spectrum corresponding to mayenite, i.e., the fully oxidized electride.

The peaks in the spectrum of the fully oxidized sample agree with the values given in the literature. Torrens *et al.* [18] assigned the two most significant peaks at $521\,\mathrm{cm}^{-1}$ and $772\,\mathrm{cm}^{-1}$ to two modes of the $AlO_4{}^{5-}$ group. With increasing electron concentration, these two peaks disappeared, while a double peak developed between $540\,\mathrm{cm}^{-1}$ and $640\,\mathrm{cm}^{-1}$. The double peak seems to increase in strength with an increasing electron concentration. Thus, the appearances of the spectra mirror the expected difference in electron concentration based on the observed color. However, in these experiments it was not possible to correlate the spectra with specific electron concentrations, since the samples oxidized unevenly as indicated by the colors and the weight gain method estimates only the average electron concentration of an entire sample. Raman spectroscopy provides local results from a small spot on the surface.

Figure 3.8b shows the spectra of evenly oxidized electride samples, which were oxidized in the LEIKA chamber at a reduced oxygen partial pressure of 0.1 mbar with a subsequent annealing time in vacuum (see Chapter 3.1.4). The samples absorbed only small amounts of oxygen (except the fully oxidized sample), leaving them all with a high electron concentration above $10^{20}\,\mathrm{cm}^{-3}$ and with their initial black color. All Raman spectra have the same characteristic appearance that was previously assigned to an electride with a high electron concentration. The spectrum of the fully oxidized sample corresponds to that of mayenite as expected. The differences between the high n_e spectra are very small; nevertheless, the top spectrum with the highest electron concentration has the most pronounced double peak. This indicates that even small differences can be detected with Raman spectroscopy. By plotting the ratio of the Raman intensity at $521\,\mathrm{cm}^{-1}$ and the maximum Raman intensity of the double peak (between $540\,\mathrm{cm}^{-1}$ and $640\,\mathrm{cm}^{-1}$) over n_e, the strong correlation between the Raman spectra and n_e becomes visible. Figure 3.9 shows the Raman-n_e correlation for the Raman spectra given in Figure 3.8b (red circles) together with results from an additional set of samples (black squares), which were reduced to different electron concentrations during the manufacturing process. The values of n_e were determined by Hall measurements.

Overall, it was not possible to validate the correlation of the intensity of the signal at $186\,\mathrm{cm}^{-1}$ with the electron concentration as given in the literature. Nevertheless, the Raman spectra exhibit distinct differences between areas of different colors that correspond to different electron concentrations, i.e., Raman spectra change with the electron concentration. First results show that the analysis of the Raman spectra correlate with the electron concentration obtained by different measurement techniques. Thus, Raman spectroscopy offers an non-invasive alternative for assessing the electron concentration of

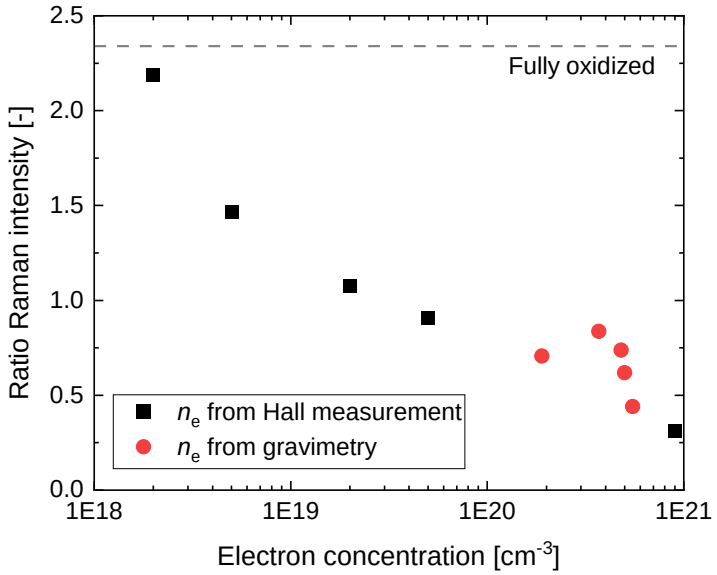

Figure 3.9: Electron concentration n_e in relation to the ratio of the Raman intensity at 521 cm^{-1} and the maximum Raman intensity of the double peak between 540 and 640 cm^{-1}. The n_e concentrations are obtained by either Hall measurements or gravimetry.

the electride material.

3.2 Cathode and RF neutralizer test chamber: Dory

For testing different kinds of neutralizers, a new test chamber, named Dory (Hollow Catho**D**e and Radi**O**-f**R**equenc**Y** neutralizer test chamber), was assembled and equipped with all necessary components to provide test capabilities for hollow cathode and radio-frequency neutralizers. This chapter provides information about the planing phase and equipment selection, which includes a background on the requirements for a hollow cathode and RF neutralizer operation.

3.2.1 Requirements

Hollow Cathodes: A hollow cathode neutralizer uses a propellant gas and its low work function insert material at high temperatures to generate a stream of electrons directed to a positive potential outside of the neutralizer as described in Chapter 2.2. Typical hollow cathodes have four electrical connections: keeper, inner-tube (insert), heater +, and heater -. The demands on the current supply are in the range of multiple ampere and the voltage output in the order of tens of volts. The inner-tube lies on ground-potential or SSG (secondary star ground) potential, which is the reference potential during joint operations with a thruster and separated from the chamber ground potential. In addition

to the electrical connections to the cathode, the anode is biased positively to imitate the thruster's ion beam. Thus, the anode also requires an electrical connection. Consequently, five electrical feedthroughs and three power supplies are required for keeper, anode, and heater. Two of them in the medium power range and one in the high-power range to provide sufficient heating power. Prototypes of hollow cathodes are often ignited by applying high voltages; consequently, a high voltage pulse must be provided by the test chamber's electrical infrastructure as well.

A hollow cathode equipped with an insert made of LaB_6 reaches operating temperatures above 1600 °C. Such high temperatures require a clean environment since the reactivity of materials generally increases with the temperature and, therefore, impurities can lead to unintended chemical reactions, such as the oxidation of the insert material. A clean environment includes a high vacuum without impurities such as oil residuals originating from the vacuum pumps. Additionally, a pure propellant flow must be ensured without contamination by air or water. The mass flows of hollow cathodes are in the range of multiple sccm (usually xenon). Prototype cathodes also need to be equipped with several temperature sensors to detect overheating at any point of testing.

Radio-frequency neutralizer: Radio-frequency neutralizers operate in an extraction-current range of milliampere by extracting electrons from an inductively coupled plasma. Since the temperatures (< 300 °C) and propellant flow (< 1 sccm) are much lower, rf neutralizer have less requirements on the test chamber and vacuum conditions as the hollow cathode. More important for rf neutralizer are very accurate and stable power supplies. In total, operation and ignition require five power supplies. The anode and collector need a power supply, which can provide up to 1 A in the medium-high voltage range with a resolution in the microampere range. The radio frequency generator (RFG) operates with one power supply for its electronics (auxiliary power supply, low voltage, < 2 A) range) and an additional power supply (5 A, min. 200 W) to generate the alternating electric field.

A rf neutralizer is ignited by an arch discharge following Paschen's law. The collector is biased to a high potential (up to 3.5 kV), followed by a pressure surge through the propellant line, which causes the electric breakdown. Consequently, the ignition phase requires a power supply, providing high voltages and a switch to control the pressure surge in parallel to the mass flow controller (MFC). The MFC itself requires accurate mass flow regulation ($\ll 0.1$ sccm) up to a maximum of 1 sccm.

3.2.2 Test chamber

The test chamber Dory itself was designed to host all anticipated neutralizer tests independent of the design and type of neutralizer. This includes the two primary cathode designs: hollow cathode neutralizer and radio-frequency neutralizer. The equipment selection is based on the requirements described in Section 3.2.1.

The entire chamber is shown in Figure 3.10. Dory has a cylindrical shape with a volume of about 0.2 m^3 (length = 0.7 m, diameter = 0.6 m). The main door completely

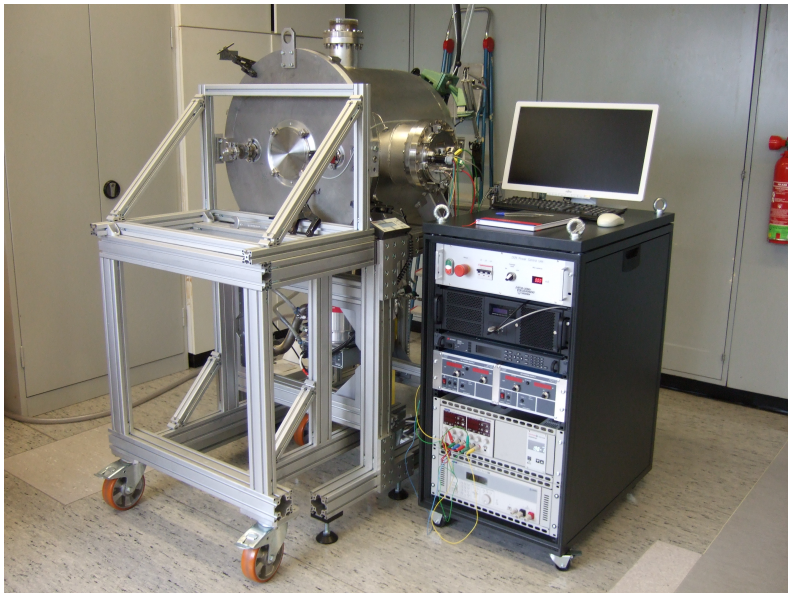

Figure 3.10: The fully equipped test chamber Dory.

opens the horizontal cylinder to one side, and the door faces a window on the other side. On the circumference are placed an additional window (on the top), all electrical feedthroughs, and the propellant feedthrough. Furthermore, a turbomolecular pump (ATH2303M, magnetic bearings) followed by a roughing vacuum pump (ACP20G, multi-stage roots pump) is also placed on the circumference, facing downwards. Both pumps are dry pumps; hence, no oil vapors contaminate the chamber. The pumping capacity is about 1000 l/s for xenon. Without propellant flow, the chamber reaches a base pressure in the lower 10^{-8} mbar. The pressure inside the chamber is measured with a full range single gauge (TPG361). For emergency shutdowns, an electrical valve is placed between the turbopump and the roughing pump. It opens and closes with the operational status (on/off) of the roughing pump. Thus, a back flow of air through the roughing pump is prevented in any case; therefore, in emergencies, the hollow cathode inside the chamber has still time to cool down.

The black rack in the front holds all the electrical equipment and the carriage left of the rack moves the lid of the chamber. Behind the rack (not visible) are stored two gas cylinders, which provide the test setup with xenon and krypton gas. The gas flows through one of two flow boards, either one with cutting ring fittings and a mass flow controller (MFC) with a range up to 10 sccm for hollow cathodes or a MFC with compression fittings and a range of up to 2 sccm (rf neutralizer) in parallel to an electrical valve (needed for a pressure surge). Compression fittings are preferred because they are easier to mount. However, some insert materials require extra clean propellant conditions and the cutting ring fittings ensure an absolute gas tight fit on the low pressure (below atmospheric pressure) side of the MFC.

Internal setup

The internal setup of the test chamber is shown in Figure3.11. The setup comprises of a base plate, a flat anode, and a generic platform for mounting a neutralizer. Behind the platform is positioned an additional platform for mounting the electrical connection.

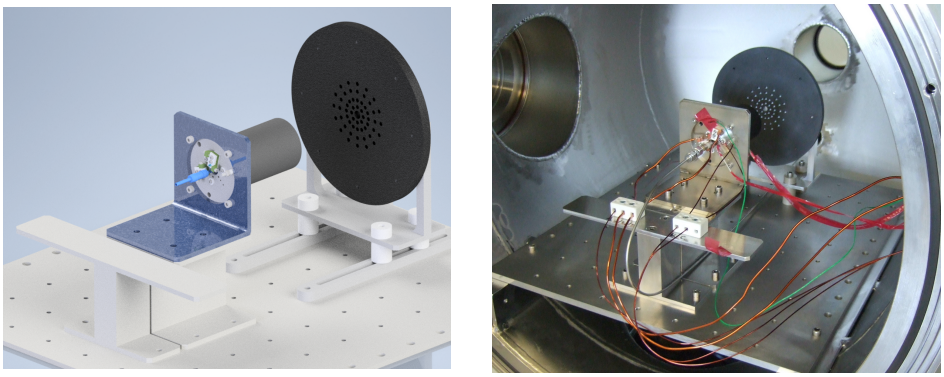

(a) (b)

Figure 3.11: The internal setup of the test chamber with integrated hollow cathode (a) as CAD drawing and (b) in reality.

The anode is a flat disc made of 10 mm thick graphite with a diameter of 180 mm. The graphite has a high thermal and electric conductivity, good resistance against sputtering, and a high emission coefficient (preventing high temperatures). Additionally, the anode is perforated to reduce the dynamic pressure in front of it. The mounting of the anode is electrically insulated from the ground (chamber) potential, and it is movable in the direction of the neutralizer axis. Thus, the distance from the neutralizer to the anode can be adjusted individually, while the anode can be biased to any potential.

Electrical setup

The electrical equipment is stored inside the black rack shown in Figure3.10. The selected power supplies with their corresponding tasks are listed in Table 3.2. They meet the previously stated requirements for operating hollow cathodes with medium-high voltages with high currents and the operation of a rf neutralizer in the low current regime but with higher voltages and high control precision requirements.

The temperature can be measured with up to three type K (up to 1250 °C) and one type C (up to 2320 °C) thermocouples. The number is limited by the number of available feedthroughs. The voltages generated by the thermocouples are translated into temperatures by the device: NI-9212. This device has eight input connectors that are insulated to each other (channel-to-channel) up to a voltage of 250 V. This is a key feature for simultaneously measuring several temperatures at different positions on a neutralizer because, during operation, the main parts are all on different electrical potentials.

Table 3.2: A list of the instruments used for the neutralizer operation at the test chamber Dory.

Instrument	Company	Capability	Function
NI-9212	National Instruments	8 Channels with 250 V channel-to-channel isolation	Temperature measurements with thermocouples.
HCP35-3500	FUG	1 Channel: 3.5 kV, 10 mA	Provides high voltage for ignitions.
Explicit for hollow cathode neutralizer			
CPX400DP	Aim-TTi	2 Channels: each 20 A, 40 V, max. 420 W	Provides the current and voltage for the operation of anode and keeper.
QPX1200SP	Aim-TTi	1 Channel 50 A, 60 V, max. 1200 W	Provides the power for the heater.
EL-Flow Select	Bronkhorst	0.2 - 10 sccm gas flow, cutting ring fitting	Controls the propellant flow.
Explicit for rf neutralizer			
2x MCP140-125	FUG	each with 1 Channel: 125 V, 1 A , 140 W	Provides the current and voltage for the operation of anode and collector.
N6775A	Keysight	1 Channel: 60 V, 5 A, 300 W	Provides the power for the RFG.
EL-Flow Prestige	Bronkhorst	0.04 - 2 sccm gas flow	Controls the propellant flow.

Usually, the keeper is only connected to its main power supply with a medium voltage range but high with currents (e.g. 60 V / 20 A). For a high voltage ignition of a hollow cathode, a high voltage pulse overlays the initial keeper voltage and causes the ignition. Dory has two ways for achieving such ignitions. First, the keeper power supply can be connected in parallel to a high voltage power supply, like the HCP-35-3500, while being protected from each other by diodes. Thus, the voltage is only applied to the keeper and not to the other power supply. This setup should enable ignitions up to 3.5 kV, which are not achieved in reality because of insufficient insulation of other components of the neutralizer.

The second possibility is the usage of a ignition box. That box is mounted in series to the keeper's main power supply and uses its voltage to charge a capacitor, which releases on command a predefined high voltage pulse (up to 2 kV). The second option requires only one power supply and operates with a well-defined pulse.

The main control box supplies all electrical equipment with the required electical power.

The box has on its backside six power sockets, distributed to the three phases of the three-phase electric input power. Therefore, all equipment can be switched off by one main switch and during operation no single phase gets overloaded. Furthermore, the main control box has two integrated power supplies for satisfying the power demands ($< 25\,\mathrm{V}$, $< 2\,\mathrm{A}$) of the MFC and the auxiliary of the RFG. Finally, the box has one switch to operate the roughing pump and the connected electrical valve. The valve closes immediately with turning off the roughing pump and opens 5 seconds after the pump is switched on to ensure a full pumping power before opening the connection to the chamber.

Software

All power supplies, the pressure gauge, the MFCs, and the temperature module are connected to the computer of the test chamber. The data is collected, processed, and stored by a LabVIEW program, which also provides access to the control of the power supplies. Depending on the kind of neutralizer (rf, hollow cathode) and its design (e.g., different inserts), the software must be individually adapted. The programs differ due to the different embedded power supplies as well. The graphical user interface (GUI) of a typical program for operating a hollow cathode is shown in Figure3.12.

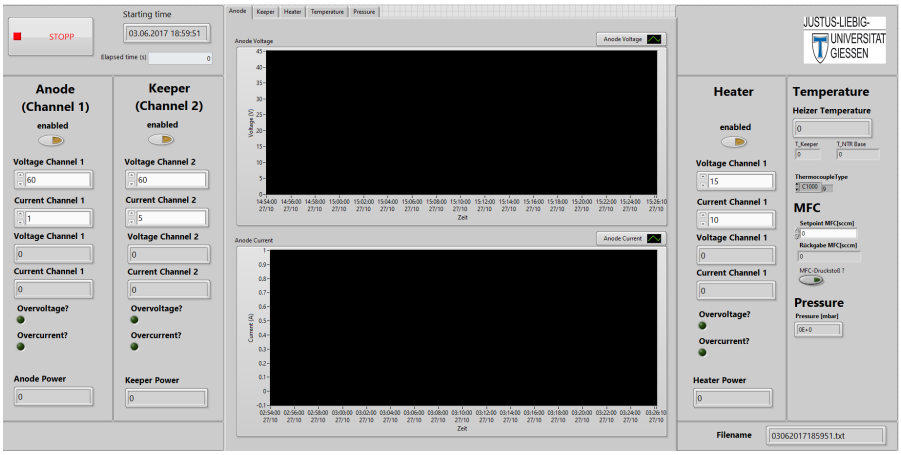

Figure 3.12: The GUI of the software to control the operation of a hollow cathode (without high voltage ignition).

The anode and keeper control panels are located on the left side. The right side shows the control panel for the heater and the readouts from the temperature and pressure sensors as well as the MFC control. The center is filled with two graphs that optionally show trends of the voltage and ampere outputs of one of the power supplies, the temperatures at the neutralizer, or the chamber pressure and mass flow. The software reads about four values each second from every connected component and stores the collected values every second in a log file with a time and date stamp.

4 Main results

The main achievements of this work focus on the development of a hollow cathode neutralizer operating with the electride C12A7:2e$^-$ as insert material and the investigation of the corrosion behavior of iodine with metals in a laboratory environment mimicking space conditions. Both topics are important to enable an fully iodine-propelled electric propulsion system in the future.

4.1 Design and operation of a hollow cathode with a C12A7:2e$^-$ insert in comparison with a LaB_6 insert

This work focuses on the implementation of the electride C12A7:2e$^-$ as insert material in a hollow cathode neutralizer with the goal of achieving endurance tests. The design of the hollow cathode presented also supports the operation of LaB_6 as insert material, which enables a direct comparison of the two materials in ignition behavior and operation. Before implementing the electride into the cathode, a thermal model of the heating and operation (discharge) phase is developed with the focus on ways to counteract the low thermal conductivity of the electride and to prevent insert melting.

4.1.1 Design of the hollow cathode

We designed and manufactured a neutralizer from scratch. Our aim is to use it as an adaptable platform allowing an easy variation of orifice (keeper/cathode) configurations and the use of inserts of different materials and spatial dimensions. The fundamental design of the neutralizer is based on the work of Goebel and Watkins [14]. Figure 4.1a shows a cross section of the designed hollow cathode with all important components, which are easily exchangeable in case of needing repairs or adaptations. The cathode orifice diameter can be altered between 0.5 mm and 3.6 mm at a thickness of 1.5 mm. The exchangeable keeper front plate has orifice diameters between 1 mm and 5 mm with a thickness of 2 mm. The distance between the cathode orifice and keeper orifice is 1 mm. All parts are manufactured by our mechanical workshop to ensure high flexibility and adaptability. Only the inserts and the insulator in the propellant feedline are purchased parts. The high flexibility of our design leads to rather large dimensions of our hollow cathode in comparison with other hollow cathodes.

The keeper is made of graphite, while the main structural components such as cathode tube, cathode orifice, and head shield holder are made of molybdenum. The heat shield and the heater wire, which is wound around a boron nitride cylinder, are made of tantalum. The base plate is machined from stainless steel and the connection insulators

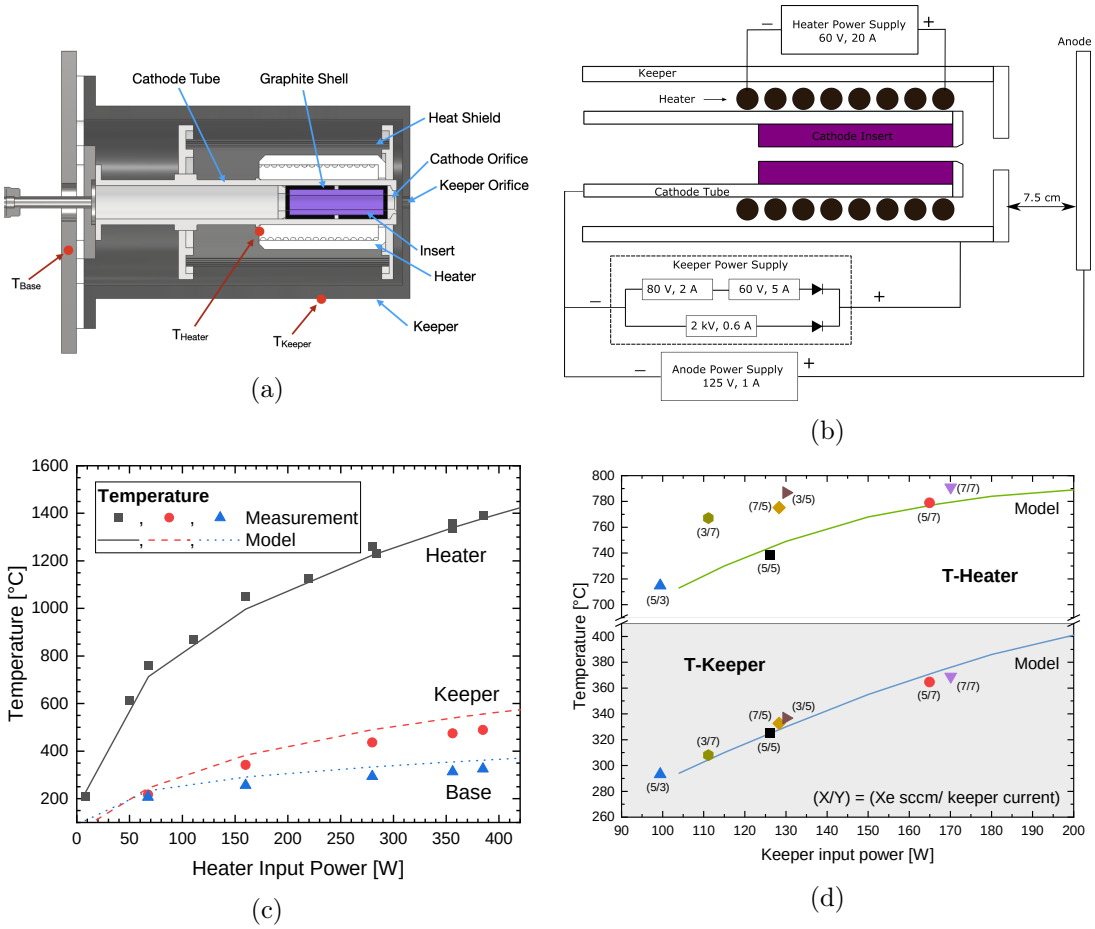

Figure 4.1: (a) Schematic cross sectional view of the developed hollow cathode neutralizer platform. The positions of the installed thermocouples are marked in red. (b) The electrical setup of the cathode during testing. Bottom: comparison of the temperature data obtained from measurements and the thermal model during (c) the heating phase as a function of the heater input power and (d) during the discharge mode at different operation points (Xe mass flow/ keeper discharge current) as a function of the input power of the keeper power supply. The positions of the temperature sensors used are indicated in (a). Operation with a LaB_6 insert and without considering current extraction to the anode.

from MACOR. The materials for all structural parts are selected to achieve an iodine compatible design for later experiments.

The LaB_6 inserts were provided by Sindlhauser Materials and the electride inserts C12A7:2e$^-$ by Advanced Thermal Devices (ATD) in Spain [15]. The LaB_6 inserts have an inner diameter of 3.8 mm, an outer diameter of 6.8 mm, and a length of 25 mm. The first batch of C12A7:2e$^-$ inserts has an inner diameter of 3.8 mm, an outer diameter of 8 mm, and a length of 24 mm (thick-walled inserts). Subsequently produced inserts have corresponding dimensions of 3.8 mm inner diameter, 6 mm outer diameter, and 10 mm length, named thin-walled inserts. All inserts are encased by graphite before inserting them into the molybdenum cathode tube.

Our test chamber for the hollow cathode tests has a cylindrical shape with an inner diameter of 0.6 m and a length of 0.7 m. The combination of a turbomolecular pump and a roughing vacuum pump provides a pumping speed for xenon of about 1000 l/s; thus, a chamber pressure in the order of 10^{-4} mbar is achieved during cathode testing. The propellant flow during testing is provided by a Bronkhorst MFC with a range up to 10 sccm. The cathode tube's potential is floating with respect to the chamber ground potential and serves as common reference potential for the keeper and anode power supplies. The graphite anode has a perforated disk shape and is placed downstream in the extraction direction at a distance of about 7.5 cm from the keeper orifice exit plane. The keeper power supply assembly comprises two separate power supplies. One with 2 kV and 600 mA is used for ignition (FUG MCP 1400-2000), the other with 60 V and 5 A (Aim-TTi CPX400DP) is used after ignition during continuous operation. If needed, a third power supply (GW Instek SPD-3606) can be used to smoothen the ignition by boosting the low voltage power supply to provide 140 V and 2 A. The electrical setup is shown in Figure 4.1b. The values, referred to in the following sections for current and voltage of heater, anode, and keeper, are directly provided by the respective power supply.

The hollow cathode is operated either in diode (only keeper) or triode (keeper and anode) configuration. In diode mode, all the discharge current extracted from the plasma, flows over towards the keeper to ground. The power input of the plasma is determined by the keeper power supply only. In triode mode, an additional current is extracted from the plasma via the graphite anode. Hence, the discharge current is composed of the keeper and anode current. The corresponding electrical power given by the sum of the products of the respective extraction currents and anode or keeper voltage.

The general cathode design was tested with a LaB_6 insert equipped with a 3.6 mm cathode orifice diameter and a 5 mm keeper orifice diameter. The test results are shown in Figure 4.1c and 4.1d. The ignition procedure starts with a heating phase of 8 to 15 min with up to 400 W heater power. The large power demands are attributed to a not fully optimized thermal design and a rather massive heater design. Nevertheless, after the heating phase, the hollow cathode ignites with a keeper voltage below 60 V and with a mass flow of 5 sccm Xe. The heater is turned off after ignition followed by the operation phase. The LaB_6 insert was operated with up to 2.5 A anode current, 3 to 7 A keeper current, and 3 to 7 sccm Xe flow. An overview of the operational parameters is given in Figure 4.1d for settings without anode current extraction. The most stable operation

settings were achieved with a keeper current of 5 A and a mass flow of 3 to 5 sccm. 3 A of keeper current was the minimum required keeper current to sustain self-heating. In addition to the isolated operation, the hollow cathode was operated successfully with a HEMP-thruster and a RIT. Overall, the operation with a LaB_6 insert has demonstrated that the hollow cathode designed by us can be operated in a wide range of parameter settings and provides a reliable test platform for testing not only different insert materials, but also various cathode and keeper orifice configurations.

4.1.2 Thermal modeling

Because of the very low thermal conductivity of about 4.5 W/(m·K) [32] and a melting point of 1230 °C of C12A7:2e$^-$ [33], the material easily overheats and the inserts tend to melt during neutralizer operation, which extinguishes the plasma and stops the plasma discharge. We have developed a thermal model of our hollow cathode design in COMSOL Multiphysics V5.3. This model allows us to identify the critical parts of the design and, thus, to reduce the risk of overheating. Based on the modeling, we define boundary conditions for the maximum power input during hollow cathode operation with C12A7:2e$^-$ as insert.

To reduce the computational time, a rotationally symmetrical model is implemented by importing a CAD file of the manufactured hollow cathode to COMSOL Multiphysics, a half of a 2-D cross-section is extracted, and overloading details are removed. The model uses the module "Heat Transfer in Solids" of COMSOL Multiphysics, which also includes "surface-to-surface heat radiation" and, therefore, covers the two important heat transport mechanisms (radiation and conduction) for thermal simulations in a vacuum environment. The geometry is compiled as assembly to include thermal contact pairs and, therefore, to simulate the conductive heat transfer more accurately. In the model, the power inputs are implemented in the 2-D cross section as line or area heat sources, which turn into area and volume heat sources, respectively, in the 3-D model during computation. The model accounts for the different materials of the various cathode components (e.g., tantalum, boron nitride, molybdenum, stainless steel, and graphite) and their temperature-dependent properties (density, heat capacity, thermal conductivity, and emissivity). We solve the corresponding heat equations for obtaining the steady-state temperatures of all parts of the hollow cathode neutralizer.

The thermal model provides results for two different operation phases: heating mode and discharge mode (after plasma ignition). The heating mode is implemented by using an area heat source (volume heat source after computation) on the cross section of the boron nitride heater as sole power input. A comparison of the modeled and measured temperatures during the heating phase is shown in Figure 4.1c. The temperature difference between model and measurement temperature at the T_{Heater}-position is below 6 %. For the two other thermocouple positions, a somewhat higher relative error below 13 % at about the same absolute temperature differences between model and experiment is observed. Overall, the agreement is satisfactory. The comparison between modeled and measured data shows that the thermal model reflects the real device well in terms of modeled material properties and thermal contact behavior between the neutralizer compo-

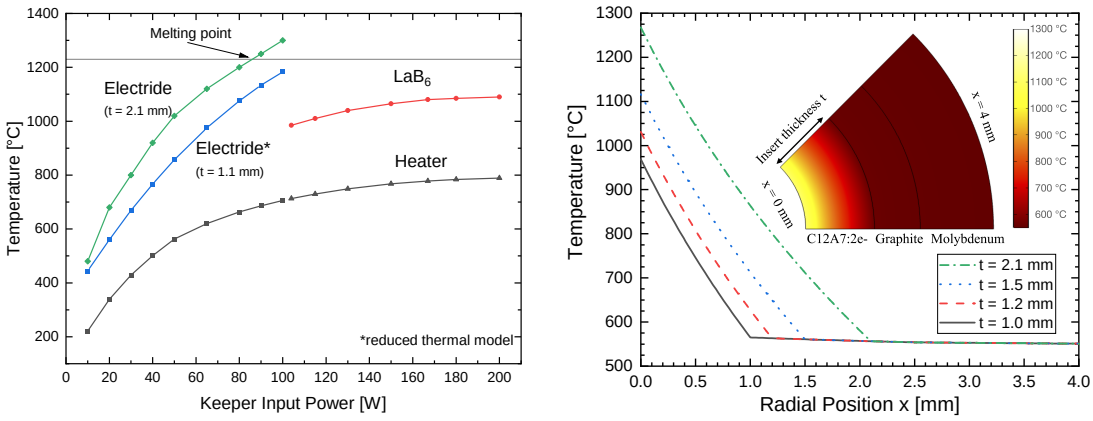

Figure 4.2: (a) The modeled heater and modeled maximal insert temperatures during the operation of a LaB_6 and C12A7:2e$^-$ (thick-walled, $t = 2.1$ mm) insert in discharge mode. (b) Influence of the C12A7:2e$^-$ insert thickness on the maximum insert temperature in a 2-D thermal model with an input power of 90 W. The inset shows the 2-D model.

nents. During the heating phase, the maximum LaB_6 insert temperature is approximately the same temperature as the heater temperature.

Accurately modeling the discharge mode of a hollow cathode by including a plasma model is very challenging and time consuming. Hence, only the power input caused by the plasma, without modeling the plasma itself, is implemented in the model. Based on Katz et al. [16], the dominating heating effect with large orifices is ion bombardment of the insert with a well distributed heating effect over most of the insert length. In our model, the discharge mode is modeled with line heat sources (area heat sources after computation) on the inner diameter of the cross sections of insert, cathode orifice, and keeper orifice. We assume the same power input in W/m^2 for insert and orifice heating [16], while assuming that the power is introduced to the first 80 % of the insert's length seen from the orifice. To further reduce the degrees of freedom, our thermal model accounts only for the extraction current of the keeper, i.e., keeper power, and neglects the current flowing towards the anode. As approximation, the entire keeper power is introduced to the discharge plasma, which in turn dissipates the provided power through three loss-channels: insert and orifice heating, keeper heating, and direct radiation to the chamber walls as well as energy transported away by ions leaving the cathode.

The exact relative heat distribution to the loss-channels remains unclear for the different configurations; particularly, since the power distribution depends not only on the orifice sizes and distances, but also on the mass flow and keeper discharge current, which cause effects not generically covered by the thermal model. The thermal model of the discharge mode is optimized for the hollow cathode configuration with a cathode orifice diameter of 3.6 mm. Here, the best results were obtained by distributing the keeper power to

the three loss-channels according to the following fractions: 0.12 direct radiation and ion loss, 0.65 – 0.44 (100 – 180 W keeper power, respectively) insert and orifice heating, and 0.23 – 0.44 (100 – 180 W keeper power, respectively) keeper heating. This approach has the advantage that no complex plasma simulation is required for obtaining results for the discharge mode. On the downside, the model cannot grab the influence of different cathode or keeper orifice configurations on the plasma distribution inside the insert, which affect the plasma-induced heating of the insert. Even with a self-consistent thermal model and omitting any plasma simulations, the thermal distribution of the discharge mode after plasma ignition is very difficult to depict. Figure 4.1d shows the modeled temperature in comparison to measured temperatures at different operation points during the discharge with an LaB_6 insert for the thermocouple positions at the heater and keeper. Despite the difficulties and uncertainties of modeling the discharge mode, the heater temperatures of the thermal model align well with the measured temperatures and verify the significance of the model. The operation modes with 5 sccm Xe flow or 5 A keeper current are predicted most accurately.

In the next step, we used the validated thermal model for predicting the heating effect on an electride insert by switching the insert's material from LaB_6 to C12A7:$2e^-$. A recalculation of the thermal model with the low thermal conductivity of the electride shows that the heating phase (without plasma) is not affected, as expected, and yields the same results as for the LaB_6 insert. However, the simulation of the temperature distribution during the discharge mode shows the challenge of having an insert with a low thermal conductivity and a low-temperature melting point, which is close to the operating temperature. Figure 4.2a shows the results of the thermal model with a thick- and thin-walled electride insert during discharge mode with respect to the keeper power. While LaB_6 required about 100 W to keep its minimum insert temperature and to maintain the discharge plasma, C12A7:$2e^-$ already reaches its melting point of 1230 °C [33] at an input power of 80 W. This reflects that the electride hollow cylinder is not capable to quickly conduct excessive insert heating by the plasma to its outside. Thus, to ensure a stable discharge without insert deterioration, the maximal keeper input power should ideally be limited to below 60 W, because Palacios et al. [34] reported that C12A7 decomposes into the phases C3A and C5A3 at 1100 °C. The subsequent tests with a thick-walled electride insert show the difficulty to stay below the power limitations. Furthermore, they prove the correctness of the predictions of the thermal model with respect to insert melting around 80 W keeper power. Therefore, we used the thermal model to identify important factors that influence the insert temperature to overcome the power limitations.

In a cathode with large orifice, the discharge-plasma directly heats the inner surface of the hollow cylindrical insert. The heat flows through the insert into the cathode's structural elements and, ultimately, to the chamber walls by conduction through the cathode holder or radiation from the cathode's outer surfaces. The insert can tolerate a higher input power, if the heat flow away from the insert's inner surface increases, i.e., the thermal barriers, presented by the thermal conductivity of the structural components, contact resistance between two components, hindering radiation, and thermal conductivity of the insert, must be reduced. Since heat transfer always depends on a temperature gradient,

the largest effects are expected close to the insert.

Increasing the thermal conductivity of the cathode tube, which transports the heat away from the insert, does not cause a significant reduction of the insert temperature. However, the contact resistance between insert to graphite shell and graphite shell to molybdenum cathode tube is crucial. Our simulations have shown that changes of the thermal contact resistance can increase the insert temperature by up to 200 °C. Once the heat flow has entered the cathode's structure, most of the heat is radiated from an outer surface to the vacuum environment. The heat shield and the surrounding keeper hinder this process. Omitting the heat shield reduces the insert temperature slightly, but drastically increases the heater power required to reach the ignition temperature; thus, the heat shield is essential in our design and cannot be omitted.

Naturally, the thermal barrier presented by the low thermal conductivity of the electride insert dominates over the other ones. Mitigating the problem of the low thermal conductivity can be achieved by modifying the chemical composition of the electride [18] or by physically reducing the thickness of the insert. Changing the composition of the electride was not in the scope of this study and will be discussed elsewhere. Instead, we investigated the effect of different insert thicknesses based on a reduced 2-D thermal model. The model comprises only an eighth of a cross sectional area perpendicular to the cathode's main axis (see inset in Figure 4.2b). The boundaries along the radial direction x are insulating, while the circular arc boundary at $x = 4$ mm is open for heat conduction. The thermal contact resistance between the materials is assumed to be zero. The materials considered are C12A7:2e$^-$, graphite, and molybdenum, respectively, from $x = 0$ mm (inside) to 4 mm (outside). The total radial thickness of the model is constant because the inner and outer radii of the cathode tube are fixed and correspond to the manufactured hollow cathode neutralizer. With decreasing thickness of the electride insert, the thickness of the graphite shell increases accordingly. Figure 4.2b shows the results of the 2-D modeling. At an input power of 90 W at the keeper, the maximum temperature of the insert varies between 1250 °C ($t = 2.1$ mm) and 950 °C ($t = 1$ mm). Hence, the effect of reducing the wall thickness of the insert is significant. To make use of this advantageous effect, a thin-walled series of inserts with a wall thickness of 1.1 mm was fabricated. Subsequent tests show the practical effect of reducing the insert wall, the input power limit during operation is increased from 80 W to above 100 W. Whether the reduction of the insert thickness limits lifetimes of the insert, is still an open question. Since the predominant problem of operating an electride insert is due to overheating, at this point, we focus on reducing the insert temperature at all costs. Generally, bulk-material inserts have a longer lifetime than dispenser cathodes. Here, the insert wear is mainly caused by material evaporation at high temperatures, while ion sputtering can increase the erosion [6]. C12A7:2e$^-$ shows a sputter resistance comparable to LaB_6 [86] and operates at lower temperatures; therefore, we do not expect lifetime to be an issue at this point. Once reaching hundreds of hours, the possible issue of evaporation must be addressed.

4.1.3 Implementation of a C12A7:2e$^-$ hollow insert

The developed hollow cathode test platform as described in Section 4.1.1 can hold inserts made of different materials and of various sizes. The switch from LaB_6 to the electride C12A7:2e$^-$ as insert material is accompanied with several changes of the insert material properties, which have an impact on the range of operation conditions. The work function reduces from about 2.7 eV for LaB_6 [9] to around 2.4 eV for C12A7:2e$^-$ [8]. Hence, the required operation temperature to provide a comparable amount of current reduces by about 300 ℃. This is very important, since the melting point of the electride is at about 1230 ℃ [33], while LaB_6 cathodes are usually operated with insert temperatures above 1300 ℃. Additionally, C12A7:2e$^-$ has a very low thermal conductivity. With about 4.5 W/mK [32] the electride is as thermally conductive as other thermal insulators and not comparable with the thermal conductivity of LaB_6 with about 47 W/mK [15]. Therefore, we performed thermal modeling as described in the previous section to estimate the effects of the reduced thermal conductivity. The modeling suggests that the discharge power must be drastically reduced to prevent the electride insert from melting. Since the cathode is operated in a discharge current controlled mode, the discharge current must be reduced to stay in the discharge power boundaries. Unfortunately, the discharge power cannot be directly controlled. After ignition hollow cathodes operate in a self-sustaining and self-regulating discharge mode. The plasma conditions determine the discharge voltage and, therefore, the discharge power for a given discharge current. In turn, the plasma is mainly influenced by the discharge current, the orifice sizes, and mass flow. The dependence between the cathode's plasma parameters and discharge current can be illustrated by a simplified power balance equation for the insert internal plasma [6]

$$\phi_\mathrm{S} = \frac{H(T)}{I_\mathrm{e}} + \frac{5}{2} \cdot T_\mathrm{eV} + \phi_\mathrm{wf} - R \cdot I_\mathrm{e}, \tag{4.1}$$

where R is the plasma resistance, I_e the discharge current, ϕ_S is the plasma sheath potential, $H(T)$ the heat loss by the insert as function of its temperature, T_eV is the electron temperature, and ϕ_wf is the work function of the insert material. Since the plasma sheath potential as part of the discharge voltage is the determining factor for insert heating, this value must be kept low.

We now compare the operation conditions of a LaB_6 insert at regular discharge currents (around 5 A, discharge power about 130 W) and the operation of an electride insert with half of the LaB_6 insert's length and at lower discharge currents (to stay below the simulated discharge power limits). The heat loss ($H(T)$) of the insert drastically decreases due to the low thermal conductivity of the electride and due to the lower required operation temperature caused by the lower work function. However, I_e must be decreased and weakens the positive effect of the reduced $H(T)$. The work function of the electride is lower and directly reduces ϕ_S. Unfortunately, a reduced discharge current directly lowers the neutral gas pressure inside a cathode [62] that leads to a higher T_eV and a lower plasma resistivity (R). Therefore, the last term in Equation 4.1 is drastically reduced by the factor of the discharge current reduction as well as the reduction of R. R on the other hand decreases due to the reduction of neutral gas pressure in addition to a

factor of 0.5 due to the halving of insert length. A low R causes less Joule heating of the plasma that is directly tied to higher sheath potentials. In summary, the lower thermal conductivity and lower work function are positive parameters with positive effects on the plasma conditions; nevertheless, the necessary discharge current reduction negates the positive effects and causes, overall, a rise of the plasma sheath potential, which increases the insert heating and endangers the insert.

Increasing the neutral gas pressure inside the cathode increases R and lowers the T_{eV}, which counteract the negative effects of the discharge current reduction by lowering the sheath potential. Taunay et al. developed an empirical relationship to describe the neutral gas pressure inside a cathode. The findings show that the orifice diameter has by far the largest effect on the pressure and that other parameters such as mass flow or orifice length have secondary effects. Therefore, a smaller orifice than that used for LaB_6 is necessary to operate a C12A7:2e$^-$ insert in this configuration. Unfortunately, the minimal and maximal orifice size is constrained by the different heating mechanisms inside a hollow cathode and the spot to plume mode transition.

Usually, decisive for selecting an orifice size for a hollow cathode is the targeted mass flow while maintaining spot mode [63]. In our setup, the mass flow is only limited by the capabilities of the mass flow controller to 10 sccm. Based on the derived correlation by Rehn and Kaufman [63], 10 sccm allow a cathode to operate in spot mode with an orifice size larger than 3.8 mm, which is larger than the size of the insert's inner diameter. Thus, the orifice size selection is not limited by the spot mode criterion. When operating a C12A7:2e$^-$ insert, spot or plume mode is not the only criterion for the orifice selection. The low thermal conductivity of 4.5 W/(m K) [32] requires uniform heating of the insert; hence, the influence of the orifice size on the plasma heating mechanism of the insert becomes a crucial selection parameter. A large orifice leads to an evenly distributed plasma density over the entire length of the insert with insert heating dominated by ion bombardment from the plasma to the inner surface [16]. Here, the ions are accelerated across the plasma sheath potential and the heating is dominated by the magnitude of that potential. A large active length of the insert and an evenly distributed insert heating is achieved. Hence, a large orifice is preferable to be used in combination with a C12A7:2e$^-$ insert. However, a large orifice is accompanied by a lower internal neutral gas pressure that leads to higher discharge and sheath voltages and, thus, higher power inputs to the insert at equal discharge currents as discussed above. The benefit of a small orifice is a high neutral gas density, which helps to operate at lower voltages and, thus, reduces the total input power at a given discharge current. Here, the cathode heating is dominated by resistive plasma heating, while the plasma density is maximum in front of the orifice plate. Accordingly, a small orifice yields a short active length of the insert and most of the heat flow is introduced at the orifice plate [65]. The insert is predominantly heated indirectly by the orifice plate via radiation and conduction. While a small orifice is generally favorable for low current cathodes, this is an undesirable way of heating a C12A7:2e$^-$ insert. Most of the heating power is introduced locally at the end of the insert close to the orifice and cannot be conducted through the insert's bulk material to the rest of the insert due to its low thermal conductivity. The result is a local hot spot at the tip of the insert where

melting of the electride is the consequence. Hence, we try to find a small, but not too small, cathode orifice to increase the internal gas pressure but without compressing the plasma at the orifice. For this purpose, we tested cathode orifices with diameters of 3.6 mm, 2 mm, and 1 mm.

Figure 4.3 summarizes the results from testing different orifice diameters and different wall thicknesses of the electride insert (the thermal modeling predicted higher possible input powers for thinner inserts). The 1 mm orifice led to high internal gas pressures, predicted to be above 10 mbar based on the empirical relationship of Taunay et al. for the given discharge currents and mass flow rates. Hence, the resulting discharge voltage and respective discharge powers were the lowest for all tested configurations. Unfortunately, the operation of an electride insert with a small cathode orifice of 1 mm in diameter could only be maintained for a maximum of 10 – 15 min and always led to melting of the front side of the insert, which is in contact with the orifice, as seen in the left inset of Figure 4.3. About the first mm of the insert length melted during the discharge and sealed the insert gas tight. Even reduced extraction currents did not prevent the melting nor ensured a stable plasma operation. A decoupling of the insert from the orifice by leaving a small gap between those two did not resolve this issue. The radiative insert heating by the orifice plate is still too high and insert melting occurs. The melting occurred at much lower keeper input power, below 50 W, as predicted by the thermal model, since the model was optimized for large orifice diameters. Consequently, a 1 mm or smaller orifice is not suitable for operating an electride insert with our cathode design. A different thermal design, which can transport large quantities of thermal power away from cathode tip and orifice, might reduce this issue.

Using the same insert thickness of 2.1 mm as before but switching to a 3.6 mm orifice size leads to higher discharge voltages caused by the lower internal gas pressures, to be estimated between 1 to 2 mbar. The individual test trails lasted up to 30 min before deliberately turning off the operation to prevent overstepping the power limits triggered by a rising keeper voltage or the tests ended with a melted insert after operating above the power limit. Operating the cathode at different settings for discharge current and mass flow did not change the behavior of the constantly rising keeper voltage. Generally, a rising keeper voltage is often observed after ignition since the cathode has its maximum temperature during ignition where heater and discharge heating add up. The cooling phase after heater turn off leads then to rising discharge voltages to compensate a high $H(T)$, an increasing T_{eV}, and a decreasing R (see Equation 4.1) with a higher discharge power. Therefore, we increased the tolerable power input of the electride insert by reducing its wall thickness to 1.1 mm. The higher power input limitations allow the cathode to have a wider range of discharge voltages for stabilizing. The tests were also conducted with an orifice of 3.6 mm. Overall, the discharge voltage was slightly higher as for the tests with the thicker insert wall thickness. This is caused by a higher $H(T)$ due to the better absolute thermal conduction of the thinner insert wall. The design changes resulted in multiple successful tests (marked in blue in Figure 4.3) with a reliable ignition behavior and a maximum operation time of 90 min (2 A, 7 sccm). A reliable and repeatable operation was not given in this configuration and a high discharge current was

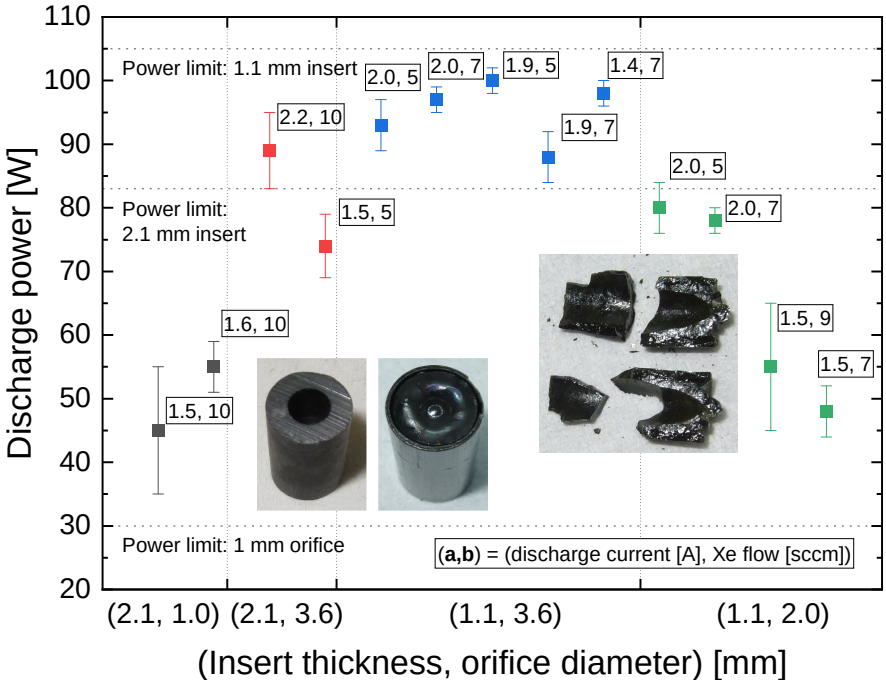

Figure 4.3: The resulting power input to the hollow cathode by the discharge current in dependence on insert wall thickness and orifice size. All given points are taken from operation points without additional heating (HP = 0 W) and with 5 – 10 sccm Xe flow. The colors of the symbols correspond to the (insert thickness, orifice diameter) configurations given on the ordinate. The given power limits are estimated based on the operation tests and are valid for short test periods with respect to melting. The insets show melted insert after being operated above the respective power limits. Left, an insert before and after the operation with a 1 mm diameter orifice and right, a split-open insert after the operation without orifice.

required to sustain the operation. Hence, the discharge power was always close to the estimated power limit, which was estimated to 105 W based on the tests results (100 W predicted by the thermal model). Due to the small margin to the power limit, the inserts regularly melted. The melting starts from the back (shown in the right inset in Figure 4.3) and transports the molted material towards the orifice, showing a well distributed plasma density.

The 2 mm orifice in combination with the 1.1 mm thick insert provided the best operational results. The higher internal gas pressure (estimated to be 3 – 4 mbar) reduces the discharge voltages at the same discharge currents. Nevertheless, the internal pressure is low enough to stay in the range of ion bombardment heating without the plasma density peaking at the orifice. The smaller orifice led to lower discharge voltages and allowed lower discharge currents and is therefore selected for all further tests. Nevertheless, the

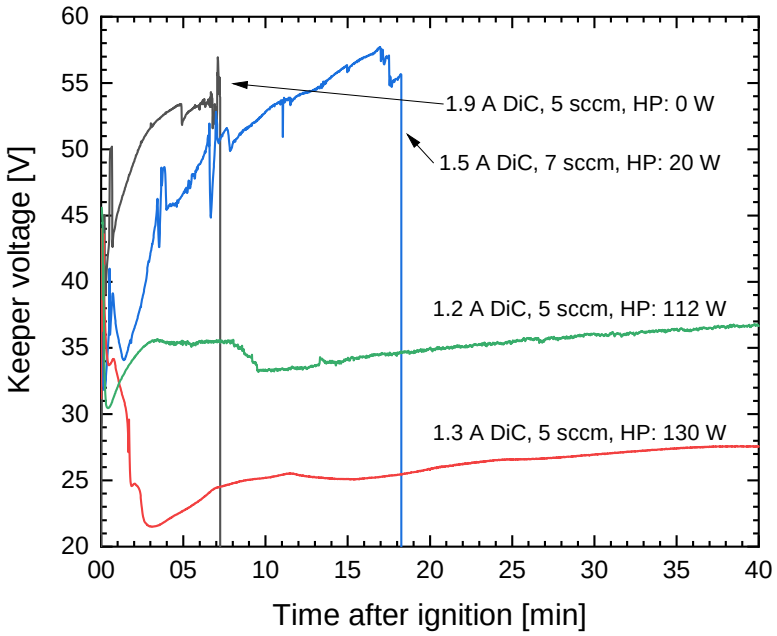

Figure 4.4: Exemplary keeper voltage curves of the first minutes after ignition with respect to different additional heat powers (HP), discharge currents (DiC), and Xe mass flows.

repeatability and the constantly rising discharge voltage was still a problem. Since the insert temperature is sufficiently high (melting issue), a possible reason for the persisting voltage increase could be explained by a too high heat loss of the plasma to the surrounding structure such as orifice, keeper, and cathode tube. The plasma cools at a rate that cannot be compensated by the low extraction currents. The issue could not be resolved with higher extraction current without damaging the insert. To reduce the heat loss, the heater was only turned down instead of being shut off after ignition. The additional heater power (HP) keeps the cathode structures at higher temperatures and ensures a hotter plasma. The effects on the operation are shown in Figure 4.4. Except for a few ignitions with extended operation times of up to 90 min, most ignitions did not stabilize without additional heater power at a keeper voltage level below the limits and ended with a forced shut down after 1 – 10 min of operation represented by the shown curve for HP: 0 W. The additional heater power stabilized the keeper voltage at lower values, extended the operation time, and supported the assumption of a too high heat loss by the plasma. As shown in Figure 4.4, operating the cathode with 112 W or 130 W of additional heater power extends the operation well above a few minutes reaching easily above 10 hours of operation. Further, adding a heat source besides the discharge heating helps the insert to maintain a more uniform temperature by reducing large temperature gradients between the inner and outer diameter. This reduces thermal stresses, promotes an even plasma distribution, and allows a reduction of the discharge current. In future

designs, an iterative thermal design could possibly resolve the issue of the cooling plasma without needing to use the additional heater.

A mass flow reduction increases the discharge voltage due to a lowering of the internal gas pressure. Hence, the lower limit is given by the discharge power, while the hard upper limit is only given by the MFC. However, higher mass flows increase the risk of pushing the plasma towards the orifice and creating dangerous plasma density peaks, which can lead to local overheating of the insert. A detailed investigation of the best mass flow values was not conducted. Nevertheless, during the tests with a 2 mm orifice and discharge current between 1 and 2 A, a mass flow of 5 to 7 sccm proved to be most effective with the most stable discharge conditions. As part of the discharge current, anode currents up to 0.5 A were achieved without entering the plume mode for an operation time in the order of minutes.

Insert degradation and failure mechanisms

One recurring reason for insert melting was the thermal contact between the insert and its support structure. As simulated with the thermal model, the thermal contact between the insert and the cathode has a significant impact on the temperature of the insert's inner surface at equal power input. The model showed a temperature difference of up to 200 °C on variation of the thermal contact resistance. The cathode operation showed the predictions to be correct. During operation, a high thermal contact resistance in a small area of the insert-graphite interface led to an overheating of the insert's inner surface radially beneath this area with the bad thermal contact. Experience shows, that once a section of the inner surface is damaged due to local overheating, the keeper voltage quickly increases, while the inner surface of the insert further deteriorates. Finally, the insert melts.

In the beginning, the thin-walled inserts were just tightly wrapped in multiple layers of graphite foil to fill the larger gap between cathode tube and insert, which replaced the graphite shells of the thick-walled and LaB_6 inserts. This setup lead to multiple molten inserts. To reduce the total thermal contact resistance, the electride inserts were placed inside a graphite holder with almost the length of the cathode tube to ensure a good thermal contact between graphite holder and cathode tube. A good thermal contact between the insert and the graphite holder was achieved by a single layer of graphite foil wrapped around the insert, ensuring a tight fit of the insert inside the graphite holder. Additionally to a good thermal contact of the outer surface of the insert, it is necessary to ensure a good thermal contact of the entire insert's surfaces including the end faces. Hence, the additional length of the graphite holder has the same inner diameter as the insert. With these measures, melting was no issue anymore. However, other issues appear only after hours of operation.

For a temperature of 1100 °C, Palacios et al. [34] reported a decomposition of the C12A7 phase into the phases C3A and C5A3. In this experiment, the decomposition started after 2 hours and over a course of the following 6 hours the C12A7 phase reduced from 100 % to about 30 %.

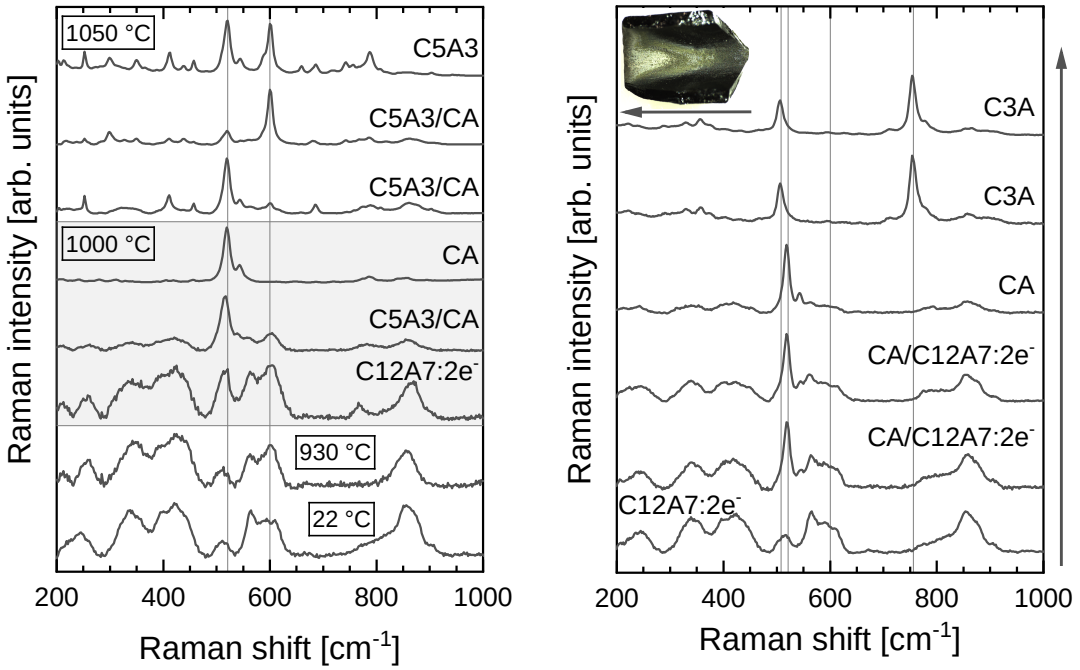

(a) (b)

Figure 4.5: (a) Raman spectra of different C12A7:2e$^-$ samples heated in ultra-high vacuum for 24 h at the given temperature. (b) Raman spectra of the inner surface of an electride insert after been operated at high temperatures (spectra collected along the direction of the indicated arrow). The inset shows the inner surface of the C12A7:2e$^-$ insert (usually black). The left side was in contact with the orifice. The grey, white, and green area indicate decomposed electride phases.

To further assess the issue of decomposition, C12A7:2e$^-$ samples were heated to 930, 1000, and 1050 ℃ under ultra-high vacuum conditions with a hold time of 24 hours at the respective temperature. Up to a temperature of 930 ℃ the temperature was accurately measured by a thermal camera with a direct view on the electride sample. Higher temperatures were only achieved by fully covering the sample with a heat shield and the temperature measurement is based on the heater temperature measured with a type-C thermocouple on the side of the heater. Consequently, the given temperature values have a large uncertainty and the samples were not necessary at an uniform temperature. Subsequent to the annealing, the surfaces of the samples were analyzed using Raman spectroscopy. Figure 4.5a shows the the measured Raman spectra from different points on the surface. The spectra taken prior to the annealing (22 ℃) are similar to all spectra taken from the surface heated to 930 ℃. Hence, no decomposition appeared at this temperature. The spectra obtained from the 1000 ℃ sample reveal a mix of the phases C12A7:2e$^-$, CA, and C5A3. The phases CA and C5A3 were identified based on the work

of Ruszak et al. [75] with the published main peaks for CA: 546 and 521 cm^{-1} and C5A3: 600 and 521 cm^{-1}. In case of the sample heated to about 1050 ℃ it was not possible to find a remaining C12A7:2e$^-$ phase. The recorded spectra show only Raman shifts typical for the phases C5A3 and CA. Hence, the electride is fully decomposed, which confirms the results published by Palacios et al. Consequently, the melting temperature of the electride is not the limiting temperature for long insert operations, which are required for hollow cathodes. The decomposition process limits the electride's operation temperature to a temperature below 1000 ℃.

After the operation for multiple hours (>15 hours) of single inserts implemented inside the hollow cathode, the inner surface of the inserts does not show any signs of decomposition, indicating an operation temperature below 1000 ℃. By omitting the front heat shield holder, the heat transport away from the orifice plate is restricted and the insert temperature is deliberately increased locally at the tip of the insert, which is in contact with the orifice plate. The cathode modification did not lead to insert melting, but later analysis showed a decomposition of the electride phase.

The inset of Figure 4.5b shows an image of inner surface of the insert after operating for three hours in the modified cathode. The left side of the insert, where the higher tip temperature developed, was in contact with the orifice plate during operation. The hot spot at the tip of the insert slowly ruins the electride material without melting it and as consequence, the keeper voltage steadily increased over the course of operation. The coloring of the insert's inner surface changed from the usual jet black to grey, green, and white. The shown conical, discolored area expands from the tip of the insert upstream towards the end of the insert. Around the full diameter were located three such discolored, conical areas. The conical shape indicates that the discoloring started at the tip and expanded with increasing operation time to the interior of the insert.

A closer analysis of the discolored areas by Raman spectroscopy confirmed a decomposition of the electride phase. Figure 4.5b shows Raman spectra recorded from different spots across the inner surface. Based on the results of Torréns-Martín et al. [18] and Ruszak et al. [75] the recorded Raman spectra show the typical Raman shifts of the phases C3A (508, and 756 cm^{-1}) and CA (521 and 546 cm^{-1}). Indications of the phase C5A3 (521 and 600 cm^{-1}) as seen in the previously described heating experiment were not identified. The spectra showing less or no remaining C12A7:2e$^-$ phase were recorded from the white/grey/green surface spots. The remaining black surface areas show clear electride spectra (bottom spectrum). The results indicate that the issue of decomposition at temperatures above 1000 ℃ is serious, as the decomposition temperature is lower than the melting temperature (1230 ℃) of the electride.

C12A7:2e$^-$ insert operation

According to the preliminary investigations described above, the hollow cathode was configured and operated with an orifice diameter of 2 mm, a keeper orifice diameter of 3 mm, a discharge current of up to 1.5 A, an additional heater power of 120 W, and a mass flow of about 6 sccm. The implemented insert was a C12A7:2e$^-$ insert with a wall

thickness of 1.1 mm (inner diameter: 3.8 mm, length 10 mm). The insert was placed in the extended graphite insert holder.

In this configuration, the tested inserts operated for about 20 hours without showing signs of deterioration. The inset at the bottom right of Figure 4.6b shows such an insert after the operation of 15 h. The insert does not show any signs of melting, cracking, or other marks of deterioration. However, each test duration was accompanied with an constantly rising keeper voltage, while all other parameters were kept constant. This is an indicating that the insert does deteriorate under the given operation conditions.

To further asses the issue of deterioration, an insert was cut in half after being operated for about 20 hours with an average keeper power of 67 W (48 V, 1.4 A) plus the additional heater power of 120 W. No more stable operation was possible at the end of the 20 hours. The cross section of the insert with a view on the inner surface is shown in the inset of Figure 4.6a. The optical inspection of the inner surface does not show signs of melting or decomposition. However, the surface was shinier than before the testing. The surface was also analyzed with Raman spectroscopy. Multiple spectra were recorded from different spots along the length axis of the insert, that starts ($x = 0$) at the insert's tip, i.e., the side facing the orifice plate. The recorded spectra are shown in Figure 4.6a. At all measured x-positions, the spectra align with the typical spectrum of C12A7:2e$^-$. This shows that no decomposition took place and the operation temperature must have been below 1000 °C for most of the operation time. Since melting and decomposition of the insert was ruled out, the most likely cause of the deterioration is sputtering.

The operational tests in which the insert was thermally overloaded by too high input powers, insert melting did occur. The melting started at the downstream end of the insert and, from there, the molten material traveled upstream towards the orifice. Hence, the plasma heating is well distributed over the entire length of the insert. To reduce the thermal loads by using the high temperatures at the downstream end of the insert, a subsequent test was conducted with a modified cathode setup. Two inserts were placed in a row inside the graphite holder. Now, the total insert length adds up to 20 mm (same length as the originally used LaB_6 insert), which doubles the available electron emitting surface area. The other configurations were unchanged.

Figure 4.6b shows the keeper voltage recorded during 29 hours of operation with a keeper current of 1.3 A. The average keeper voltage dropped by about 10 V in comparison to the average keeper voltage during the previous tests with a single insert. Therefore, the double insert was operated with an average of 49 W (38 V, 1.3 A) plus an additional heater power of 110 W. After 16 hours of operation the cathode turned off after a few instabilities. The following ignition was successful with a keeper voltage below 60 V and the operation continued for 1.5 hours (total 17.5 hours) before, unexpectedly, shutting down again without instabilities. The inspection revealed that the side of keeper orifice plate facing the cathode plasma was covered with a nonconductive layer (inset top left in Figure 4.6b). All cathode structural materials in contact with the plasma such as molybdenum, graphite, and tantalum are always electrically conductive, whereas surface layers of sputtered electride have shown to be insulating. Therefore, the insulating surface

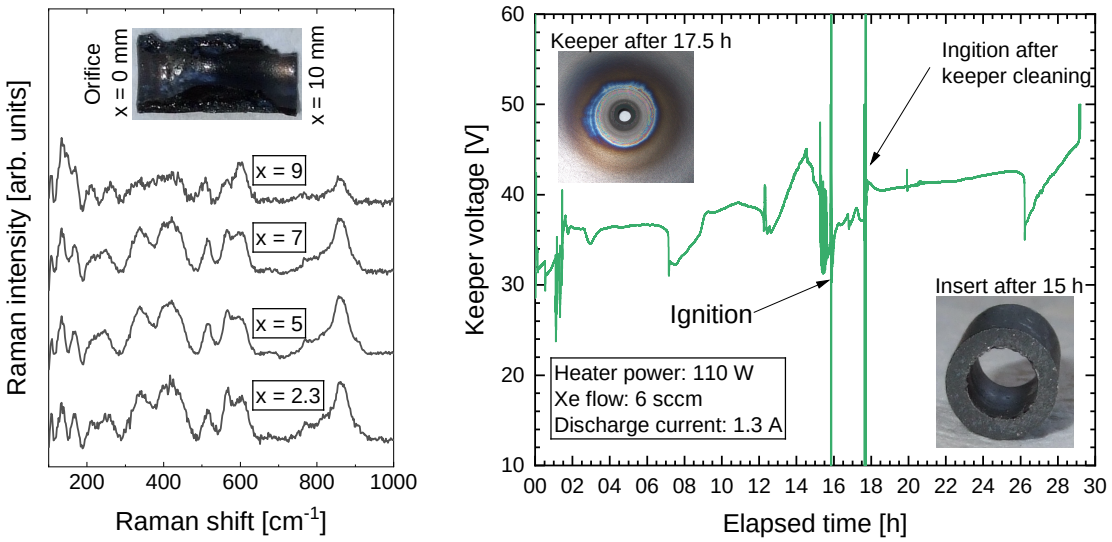

Figure 4.6: (a) Raman spectra obtained from the inner surface of an insert after 20 h of operation. The inset shows a cross section of the insert. (b) A 29 h test run with two electride inserts at a discharge current of 1.3 A, with a mass flow of 6.0 sccm, and an additional heater power of 110 W. The first inset (top left) shows the inner keeper surface around the keeper orifice after about 17.5 h. The second inset (bottom right) shows an insert after being operated for 15 h in a comparable test.

layer must be sputtered electride material.

After cleaning the keeper, the operation continued at slightly elevated keeper voltages reaching 29 hours before shutting down again. The subsequent insert inspection did not show sings of deterioration. The keeper was cleaned again and the cathode was put back into the vacuum chamber. Unfortunately, an operational mistake melted the insert in the first seconds after re-ignition.

The long operation tests were conducted without anode current extraction because the deterioration of the electride insert caused a transition into plume mode after multiple hours of testing and without an automated shut down procedure in place, operations without continuous personal supervision would not have been possible. Nevertheless, anode currents of up to 0.5 A were extracted over short periods of time, while staying below 1.5 A of total extraction current.

Comparison of the ignition behavior of LaB_6 and C12A7:$2e^-$

To ignite the hollow cathode with a LaB_6 insert, the heater power was set to 400 W for about 8.5 min until the heater reached a temperature of 1400 °C. Subsequently, the Xe flow of 5 sccm started and a voltage was applied at the keeper. As shown in Figure 4.7, the ignition voltage was below 60 V for the given settings. By reducing the heater power and, consequently, the temperature, the ignition voltage increased. At a heater power of 203 W (T = 1110 °C), the hollow cathode did not ignite even with a propellant flow of up to 10 sccm and a keeper voltage up to 2 kV. A slight increase in heater power (226 W, T = 1150 °C) led to a successful ignition at 1.5 kV keeper voltage and 8 sccm Xe flow or 1 kV and 10 sccm. At a heater power of 252 W (T = 1200 °C) the ignition keeper voltage dropped below 500 V at 5 sccm of propellant flow.

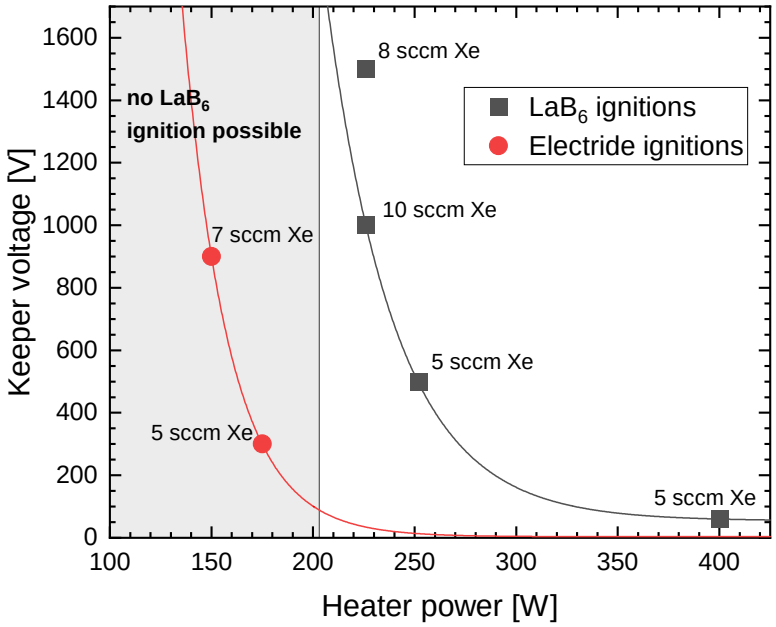

Figure 4.7: Heater power vs. keeper voltage required for igniting the hollow cathode. The ignition behavior for the insert materials LaB_6 and the electride are given for the minimal required Xe mass flow. The keeper voltage was increased to a maximum of 2 kV at points without ignition.

The identical hollow cathode with a built-in C12A7:$2e^-$ insert ignited at lower temperatures. The ignition procedure was extended to 1.5 to 2 h with a stepwise increase of heater power to reduce thermal stresses on the insert caused by an uneven temperature distribution. The final heater power setting was 175 W, yielding a temperature slightly above 1000 °C of heater temperature. The first ignition of a new C12A7:$2e^-$ insert was usually more difficult than the subsequent ones. Often the keeper voltage had to be increased to up to 900 V or a pressure surge was necessary to ignite the discharge. Lengthening the last heating interval seemed to have a positive effect on the ignition behavior. The first

ignition was followed by a bumpy operation lasting for tens of minutes (see operation at 0 to 2 hours in Figure 4.6b). Subsequent ignitions reliably occurred with a Xe mass flow of 5 sccm and an ignition keeper voltage below 300 V at 175 W heater power as shown in Figure 4.7. These ignitions were followed by a smooth cathode operation (see ignition at 18 hours in Figure 4.6b). The electride seems to form a passivation layer during the manufacturing process, which is removed during the first minutes of operation. This layer did not form again after an exposure of the insert to the atmosphere for a couple of hours.

Overall, the C12A7:2e$^-$ ignites at much lower temperatures than the LaB_6, which reflects the lower work function and underlines this benefit of the electride material.

4.1.4 Conclusion: cathode operation with an C12A7:2e$^-$ insert

Preliminary tests showed that the operation temperature of the electride is limited by the melting temperature of 1230 °C for short temperature exposure durations. For long operation duration, the insert's maximum temperature limit reduces to below 1000 °C due to a decomposition of the C12A7 phase into CA, C3A, and C5A3.

A hollow cathode developed for inserts made of the material LaB_6 was modified to hold C12A7:2e$^-$ inserts. Based on a series of tests, thermal modeling, and data analysis, the issues of overheating, melting, and decomposition of the electride insert during operation were successfully mitigated. Operation durations of up to 29 hours were achieved at a discharge current of 1.3 A without showing signs of melting or decomposition. The remaining insert deterioration mechanism was identified as sputtering of the electride insert, which can possibly be reduced with an iterated cathode design, optimized for the operation of an electride insert.

In a direct comparison of a LaB_6 and a C12A7:2e$^-$ insert, tested in the same cathode without major modifications, the electride showed a better ignition behavior, ignition at lower temperatures, than the LaB_6 insert material.

4.2 Additional Results - Hollow cathode operation with krypton

The previous sections showed and explained the behavior of a hollow cathode operating with different insert materials at a wide range of operational settings. However, all experiments were conducted with xenon as propellant. Other propellants, such as the alternative propellants krypton or iodine, change the operational parameters of a hollow cathode as well. This section shows results from the hollow cathode with a LaB_6 insert operating with krypton as propellant.

Krypton is the lighter noble gas neighbor of xenon with an atomic mass of about 83.8 u (131.3 u for xenon). The higher availability of krypton in the atmosphere of Earth leads to a much lower price per kilogram in comparison with xenon. Unfortunately, using krypton for electric propulsion is often associated with lower thrust levels and higher power consumption [87, 88], due to the lower atomic mass and higher ionization energy (krypton: 14.0 eV, xenon: 12.1 eV) [89]. A hollow cathode operating on krypton is expected to show

a higher power consumption for a given neutralization current compared to xenon, because the lower atomic mass and higher ionization energy reduce the internal pressure of the cathode according to Equation 2.5, which increases the power consumption.

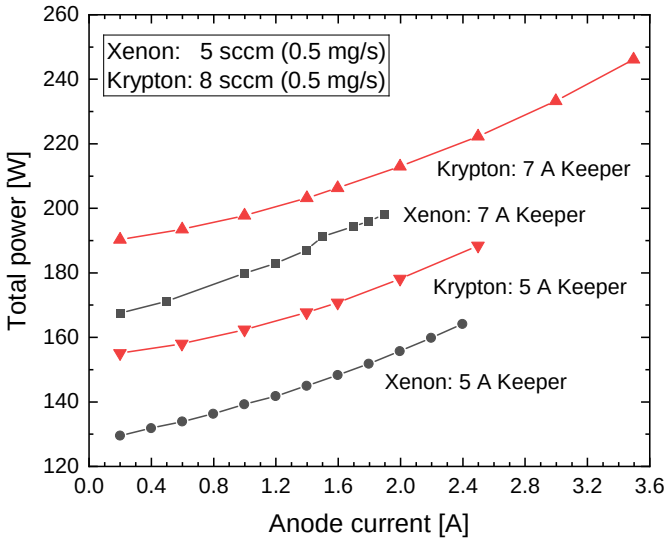

Figure 4.8: The total power consumption (including keeper and anode power) with respect to the anode current of the hollow cathode neutralizer (LaB_6 insert) operating with the propellants krypton and xenon.

In this set of experiments, the developed hollow cathode is equipped with a LaB_6 insert and it is operated subsequently with krypton and xenon as propellant without a change of the cathode configuration. Figure 4.8 shows the total power consumption of the cathode at 5 and 7 A keeper current with respect to the anode current for xenon and krypton as propellant. The cathode operated with a propellant flow of 5 sccm xenon or 8 sccm krypton, which are both correspond to a mass flow of 0.5 mg/s. The internal gas pressure is with 1.40 mbar and 1.45 mbar, respectively, alike (calculated with Equation 2.5). Even at similar internal pressures, the operation with krypton requires a higher power input, i.e., the voltage level of the keeper and anode are higher and the hollow cathode operates less efficiently. The higher power consumption also results in higher insert temperatures. Hence, krypton is not attractive when operating the hollow cathode neutralizer with an electride insert, due the problem of insert overheating and melting.

4.3 Corrosion of metal parts on satellites by iodine exposure in space

This section was published by the author of this work in the *Journal of Electric Propulsion* with the title "*Corrosion of metal parts on satellites by iodine exposure in space*" [46].

4.3.1 Abstract

Iodine becomes increasingly popular as alternative propellant for electric propulsion (EP) systems offering several advantages over established xenon. However, iodine is also a reactive and corrosive element. Thus, a careful material selection for the EP system itself, but also for components employed on the satellite is required in the light of typical space mission durations of several years. Here, we carefully define an approach for mimicking long-term interaction of material specimens with iodine in a space environment. The space conditions cover typical iodine atmospheres (10^{-1} to 10^{-4} Pa), which occur in the vicinity of a satellite employing an iodine-fed EP system, and exposure times, which correspond to 10 years of mission duration. The approach is used to expose a wide range of metal specimens commonly used on spacecraft to iodine. Chemical modifications of the surfaces of the treated samples are analyzed by x-ray photoelectron spectroscopy (XPS). The elemental metals Fe, Ti, Al, and Nb chemically react with iodine, whereas the elemental metals Ni, Cr, Ta, W, and Mo are basically inert. The stainless-steel and aluminum metal alloys show the same behavior as the corresponding dominant elemental specimens, i.e., Fe and Al, respectively. Somewhat surprisingly, Cr as constituent in stainless steel reacts with iodine, in contrast to elemental Cr. Nevertheless, our studies reveal that long-term exposure to low-pressure iodine atmospheres is not critical for the macroscopic structural integrity of all tested specimens even over space mission durations of several years. The reaction with iodine is macroscopically a surface effect, which mainly affects the optical appearance.

4.3.2 Introduction

During the last decade electric propulsion (EP) systems, have developed from a niche technology into a mass product [2] enabling a large variety of scientific and commercial space missions. EP systems are used today on satellites ranging from nanosatellites [90] to large satellites [14] and are even considered as main propulsion systems for manned deep space missions [91]. The most widely used propellant in EP is the heavy noble gas xenon. However, xenon is a scarce resource and, therefore, expensive. Iodine is a possible alternative, since it is also a heavy atom, but much cheaper than xenon. In addition, no pressurized storage tanks are required for iodine, which further reduces the total costs and enables an easier implementation into small satellites [44, 92]. Recently, Rafalskyi et al. [44] demonstrated the first satellite with an iodine-fed propulsion system in space. Satellites of mega constellations or cube sats are likely candidates to be equipped with iodine-fed EP systems. Therefore, it may be anticipated that the number of iodine-fed EP systems will significantly increase in the near future, in particular, if the potential

danger of the corrosive nature of iodine can be controlled. Dedicated studies for assessing the effect of an iodine-rich space environment on typical materials used by space industry on satellites need to be conducted. An important aspect in this context is the definition of iodine-rich space conditions and their realization in terrestrial experiments since the reactivity of iodine may be strongly influenced by the presence of other substances. For example, water, which is typically not present in space, enhances the reactivity of iodine immensely [93].

General corrosive effects of iodine have been extensively investigated in the late twentieth century in the context of nuclear power plants [94–98]. Obviously, these studies did not mimic the particularities of space environments anticipated for iodine-fed satellites. In recent years, in the light of iodine as alternative EP propellant, first new studies were conducted to investigate the effects of iodine on materials used in the space industry [45, 52–54]. These experiments have shown that iodine vapor can erode a wide range of materials on rather short time scales compared with typical spacecraft mission times of several years [51]. These experiments were mostly performed with dense iodine vapors or with a gas mixture, e.g., of iodine and an inert gas, with high iodine partial pressure. Such conditions correspond to those inside propellant feedlines and the thruster itself. However, these publications have not dealt with the effects of iodine on the outer surfaces of the satellite where the iodine densities or partial pressures are much lower. By expelling iodine, the amount of iodine in the spacecraft's surroundings is increased. The entire outer shell of the spacecraft will be in contact with the residual iodine. At such low iodine partial pressures, the exploratory focus is altered. The research question of interest is no longer whether a material is eroded by iodine, but rather how long may this material endure exposure to iodine without loss of structural integrity or the desired function.

In this work, we focus on the corrosive effect of iodine on a wide range of different metals. The exposure conditions used mimic the low-pressure environment in space experienced by satellites with iodine-fed EP systems over long mission durations. The first section explains and justifies how the space conditions are realized by terrestrial experiments. Furthermore, it gives details of the experimental setup and the samples studied. The following section presents the results of the analysis of the effect of iodine on the specimens studied. The last section summarizes the results and concludes the paper.

4.3.3 How to mimic space environment of satellites with iodine-fed EP systems?

Standard spacecraft components during satellite operation experience typically temperatures between - 100 and + 100 °C [99]. Higher temperatures generally promote chemical reactions; hence, we chose the upper limit of + 100 °C in our experiments as it presents the worst-case scenario. Furthermore, when operating an iodine-fed EP system, different parts of the satellite are exposed to different iodine partial pressures. Typical partial pressures inside the propellant feed system will be 2 to 6 kPa [44] and inside of the thruster about 1 to 2.5 Pa [100]. Outside the thruster, typical iodine partial pressure inside the plume will be about 1e-3 Pa and will decrease with increasing distance from the satellite

down to high vacuum conditions. A corresponding situation is illustrated in Figure 4.9.

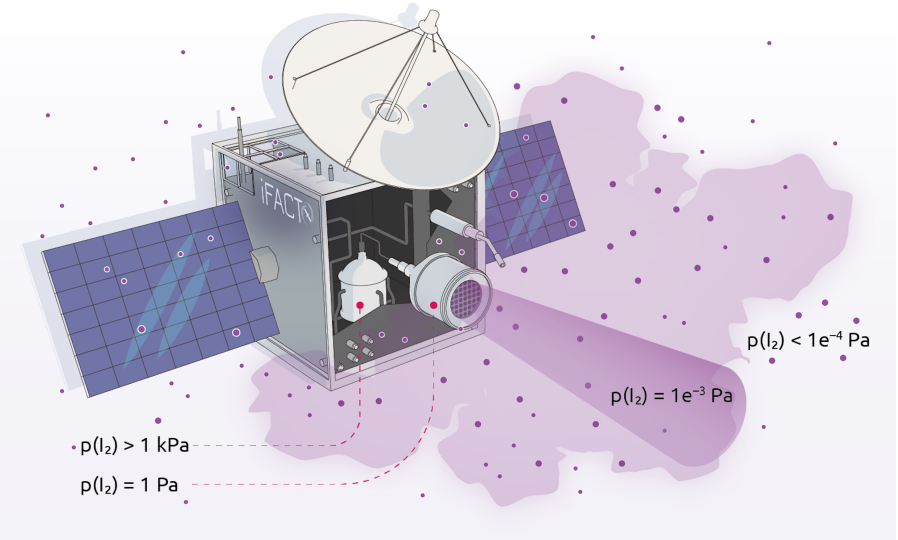

Figure 4.9: A sketch of a satellite operating an iodine-fed electrical propulsion system. Typical iodine partial pressures are indicated.

A prerequisite for a chemical reaction to occur is that the reaction partners come into contact. This implies microscopically that a collision between the reaction partners takes place. In our case, one of the reaction partners is a surface atom, which is bonded to other atoms of the solid, whilst the other one is a microscopic species of the atmosphere surrounding the satellite and colliding with its surface. Basically four microscopic species are generated by the electric thruster operating with iodine as propellant, for example, a radiofrequency ion thruster (RIT). These are the neutrals atomic I and molecular I_2 and the corresponding ionized species I^+ and I_2^+. Molecular and atomic iodine ions, I^+ and I_2^+, play a minor role in the context of surface erosion by the atmosphere as the plasma of an ion thruster is usually a low-temperature plasma. For example, global modelling of RITs operating with iodine as propellant reveals that only a few percent of the species inside the plasma vessel are ionized, the others are the neutral species [81, 101]. The same can be assumed for the species exiting the plasma vessel, either by diffusion or extraction by the grid system of the RIT. The main difference between ionic and neutral species is that the former move away from the thruster at high speed, typically several 10 km/s. Thus, the likelihood for ionic species to return to the satellite is rather low, in particular, as the ion beam is also neutralized by electrons. Therefore, ions will only cause erosion or sputtering if the ion beam extracted from the thruster directly hits the satellite surfaces. This will only occur unintentionally or by system failure. However, ion sputtering experiments on metallic and other samples demonstrate that, at typical ion energies of 1000 eV, the effect of ion etching by I^+ and Xe^+, which possess comparable mass, is rather similar. Xenon ions are used for comparison as Xe is

the still most commonly used EP propellant. The similarity of the etching results implies that the etching process is not chemical, but dominantly physical by collisions [86]. Thus, the neutral species dominate the chemical behavior of the iodine atmosphere fed by the thruster and surrounding the satellite. There are the two types of neutral species which form the atmosphere around the satellite, molecular I_2 and atomic I. In the iodine plasma inside a RIT, both neutral species occur in roughly equal numbers whereas in our iodine gas treatment we have almost 100 % I_2. In the atmosphere surrounding the thruster, the atomic iodine will react to I_2 upon collision of atomic iodine, thus, will be lower than inside the thruster. However, it cannot be ruled out that in the steady state established in the atmosphere atomic iodine is still present. The fraction of iodine in the atmosphere, will depend on the operational conditions of the thruster and the mission scenario. If the thruster is not operated, the atmosphere will turn into an I_2 gas. We will show that this is not important in our considerations because the thermo-chemical considerations yield for the reaction of both species with the metals large and negative changes of the Gibbs free energy indicating that almost every collision triggers a chemical reaction and a back reaction is extremely unlikely. Therefore, a treatment of the metal surfaces with pure I_2 gas or a I_2 with a fraction of I should yield comparable results. Therefore, we only consider I_2 as reaction for the metals in what follows.

As pointed out above, a collision of an I_2 molecule with the surface is a prerequisite for the I_2 molecule to undergo a chemical reaction with the metal atoms of the surface. At low temperatures, the I_2 molecule may even be adsorbed. However, at the chosen temperature of 100 °C, the saturation vapor pressure is p* = 6 kPa, which is much higher than the anticipated pressure in the satellite surroundings. Therefore, adsorption of iodine on the surface may be ruled out and the dominant contact mechanism of iodine molecules and the surface will be by collision. Not every collision leads to a chemical reaction. However, the likelihood of a chemical reaction to occur in a given time span is proportional to the collision frequency of the gas molecules with the surface per surface area, i.e., the particle current density and the exposure time Δt. The particle current density $J_{\mathrm{Collision}}$ impinging on the surface can be described assuming that the ideal gas equation is valid [102],

$$J_{\mathrm{Collision}} = \frac{p}{4\mathrm{k_B}T} \cdot \sqrt{\frac{8\mathrm{k_B}T}{\pi M}}\ [\text{collision per s and m}^2] \tag{4.2}$$

where T is the absolute temperature, p the partial pressure of the gas species, here iodine I_2, $\mathrm{k_B}$ the Stefan-Boltzmann constant, and M is the molecular mass of the gas species (254 u = 4.22e-25 kg in case of I_2).

The terrestrial experiments mimicking the effect of iodine on a solid will be performed with the solid located inside a vessel of volume V with a gas mixture of iodine and the noble gas argon (see Figure 4.10). Considering that no chemical reaction takes place between chemically inert Ar and I_2 in the gas mixture, both species are individually describable by the ideal gas equation $p_i V = N_i \mathrm{k_B} T$ (i = 1, 2), where p_i and N_i denote the partial pressure and the number of particles, respectively, of species i inside V. Total pressure is the sum of the partial pressures $p_{\mathrm{tot}} = p_1 + p_2$. This relation holds for gas mixtures of iodine and argon, despite the strong reactivity of iodine, if we assume an ideal

gas solution.

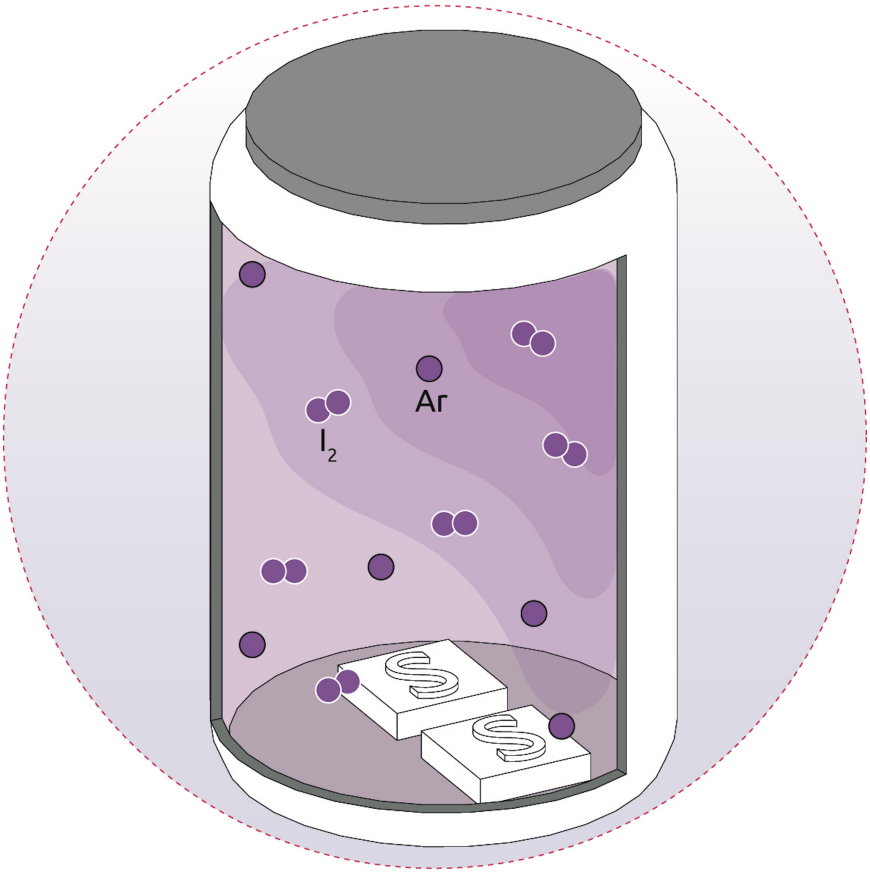

Figure 4.10: Laboratory experiments for realizing different space scenarios representing the conditions in the surroundings of a satellite with an iodine-fed EP system. The samples are treated at 100 °C in a sealed glass vessel containing a defined amount of iodine and argon. The vessel V was loaded inside a glove box with a dry argon atmosphere at room temperature with the desired amount m of solid iodine and the cleaned samples, afterwards it is sealed. Heating the sample up to 100 °C allows one to fully or partially evaporate the iodine yielding partial pressures of iodine $p \leq p*$.

At 100 °C (373 K), iodine confined in a vessel of finite volume V will have a saturation vapor pressure of about $p* = 6$ kPa as iodine partial pressure, as long as the inequality

$$m/V \geq (M \cdot p*)/(N_A \cdot \mathrm{k_B} \cdot T) \tag{4.3}$$

holds for the mass m of solid iodine stored inside the finite volume V. Partial pressures of iodine gas inside the reaction vessel, which are lower than its saturation vapor pressure $p*$, can be obtained, if the mass m is smaller than that yielding equality in Eq. (2). In

these cases, all the iodine in the vessel is in the gaseous state and its partial pressure is given by

$$p = \frac{m \cdot T \cdot N \cdot \mathrm{k_B}}{V \cdot M} \tag{4.4}$$

Here, the number of surface atoms of the solid reacting with the impinging iodine molecules at a given temperature T is to a first approximation proportional to $J_{\mathrm{Collision}} \propto p$ (where p denotes the partial pressure of iodine) and the exposure time Δt. This implies that pairs (p,Δt) yielding the same value for the product $p \cdot \Delta t$ will have a similar effect on the surface. The approximation is particularly suitable to mimic the effects in low-pressure iodine environments over long periods of time, as experienced in space missions, by choosing higher pressures and shorter exposure times in the terrestrial experiments.

At 100 ℃ (373 K), iodine reaches its saturation vapor pressure $p*$ of about 6 kPa only if a sufficient amount of solid iodine is located in the finite volume V. The corresponding $J_{\mathrm{Collision}}$ multiplied with an exposure time $\Delta t = 3$ h leads to a value of about 6e29 collisions per m^2 with a solid surface in contact with the gas. The same total number of collisions per m^2 is obtained for another (p,Δt)-pair, namely p = 0.1 Pa at 100 ℃ and $\Delta t = 10$ years, which is typical for what satellite components outside, but in the vicinity of the iodine-fed EP system, may experience.

In this fashion, we designed a set of exposure experiments intended to mimic the effect of iodine on outside satellite components for environmental iodine partial pressures p of 1e-2, 1e-3, and 1e-4 Pa and a mission duration of 10 years. This is achieved by reducing the partial pressure of iodine inside the reaction vessel by increasing its volume V or by reducing the amount of iodine m inside the vessel according to Eq. (3) or by reducing the exposure time Δt.

Some additional aspects need to be considered to justify our approach. A reduction of the iodine partial pressure reduces the number of collisions very effectively, but a reduced partial pressure (below the saturation vapor pressure) has also an influence on the chemical reactions from a thermodynamic point of view going beyond the ideal gas approximation. A chemical reaction will be exergonic (spontaneous) only, if the change of Gibbs free energy is negative, i.e., free energy is released over the course of the reaction. The change of Gibbs free energy for a specific chemical reaction ($\Delta_r G^T$) at temperature T is given by

$$\Delta_r G^T = \sum \nu_i \cdot \Delta_f G_i^T \tag{4.5}$$

Large negative values of $\Delta_r G^T$ indicate a self-driven (more exergonic) reaction. At constant pressure and constant temperature, the Gibbs free energy for the reaction depends only on Gibbs free energy ($\Delta_f G^T$) and molar coefficients (ν_i) of the reactants and products involved in the chemical reaction. The molar coefficient for the reaction educts is of a negative sign whereas that the reaction products is positive by convention. The standard enthalpy of formation $\Delta_f H^T$ and standard entropy S^T for all kinds of substances, e.g., $\mathrm{I_{2(g)}}$, $\mathrm{FeI_2}$, etc. can be found in the literature for the temperature T of interest [103]. This data is used to calculate the available energy ($\Delta_f G^T = \Delta_f H^T - T^* S^T$). Above, we have assumed that the outcome of the exposure experiment is the same if the product of $p \cdot \Delta t$ is equal for the two scenarios and the temperature kept constant. This implies

that the change of Gibbs free energy $\Delta_r G$ according to Eq. (4) for the surface reaction involving iodine is independent of iodine partial pressure. Nevertheless, the validity and the boundaries of this assumption needs to be verified. The molar coefficients ν_i do not depend on iodine partial pressure. However, the Gibbs free energy of iodine exhibits a dependence on partial pressure for iodine in its gaseous form:

$$\Delta_f G^{T^*}(I_2) = \Delta_f G^T(I_2) + \mathrm{R}T \cdot \ln\left(\frac{p(I_2)}{p^c}\right) \tag{4.6}$$

where R is the ideal gas constant, $p(\mathrm{I_2})$ the partial pressure of iodine inside the reaction vessel, and p^{c} is the reference pressure of the standard conditions (10^5 Pa). The effect of the additional term is given in Table 1 for different partial pressures of iodine.

Table 4.1: The change of Gibbs free energy for gaseous iodine at different iodine partial pressures for $p^c = 10^5$ Pa and $T = 100\,°\mathrm{C}$. Values are given in kJ/mol.

$p(\mathrm{I_2})$ [Pa]	$\mathrm{R}T \cdot \ln\left(\frac{p(I_2)}{p^c}\right)$	$\Delta_f G^{T^*}(\mathrm{I_2}, p(\mathrm{I_2}))$
1e-04	-64.27	-104.20
1e-03	-57.12	-97.06
1e-02	-49.98	-89.92
1e-01	-42.84	-82.78
15	-27.30	-67.24
200	-19.27	-59.21
2000	-12.13	-52.07
6000	-8.72	-48.66

In this work, we consider the reaction of gaseous iodine with a solid metal A. As example, the chemical reaction between Fe and $\mathrm{I_2}$ can be written as $\mathrm{Fe_{(s)}} + \mathrm{I_{2(g)}} \rightarrow \mathrm{FeI_{2(s)}}$. The molar coefficients are -1, -1, and 1, respectively from left to right. Hence, Eq.4 is rewritten as:

$$\Delta_r G^T(\mathrm{FeI_2}) = \Delta_f G^T(\mathrm{FeI_2}) - \Delta_f G^T(\mathrm{Fe}) - \Delta_f G^{T^*}(\mathrm{I_2}, p(\mathrm{I_2})) \tag{4.7}$$

The literature values for $\Delta_f G^T$ of the substances at T = 100 °C are -174.0 kJ/mol and -12.3 kJ/mol for $\mathrm{FeI_2}$ and Fe, respectively. The tabulated values for $\Delta_f G^{T^*}(\mathrm{I_2}, p(\mathrm{I_2}))$ at the different iodine partial pressures are given in Table 1. We find that $\Delta_r G^T$ is always negative, thus, the reaction is exergonic. Furthermore, $\Delta_r G^T(\mathrm{FeI_2})$ is only about 16% lower at a partial iodine pressure of 15 Pa compared to the value at 6 kPa partial iodine pressure, which is the saturation pressure of the test conditions. A change of this magnitude is to a first approximation negligible in terms of chemical reactiveness, since the reaction remains strongly exergonic in all conditions. Nevertheless, reducing the iodine partial pressure by multiple orders of magnitude, as present in space, leads to a significant reduction of $\Delta_r G^T$ and, therefore, a less, but still, exergonic reaction. Conclusions similar to those drawn from the $\mathrm{FeI_2}$ reaction hold true for all expected

products as shown in Table 2. Conducting the same calculation for atomic iodine using the corresponding thermo-chemical data [104] yields the same trends for $\Delta_r G^T$ with 1.5 times higher values. As pointed out above, this means in both cases that the back reaction is suppressed. Whether the reaction of the metal with I or I_2 is more likely cannot be decided based on the corresponding $\Delta_r G^T$ values.

Table 4.2: Calculated values of Gibbs free energy ($\Delta_r G^T$) at 100 °C of possible iodine reaction scenarios following Equation 4.7. Literature values for $\Delta_f G^T$ are taken from [103] and are given in kJ/mol.

Product P p(I_2) [Pa]	AlI_3	CrI_2	CrI_3	CuI	FeI_2	MgI_2	MoI_2	NiI_2	TiI_4
1e-04	-202.6	-106.9	-113.3	-41.7	-57.5	-304.0	-49.7	-25.2	-257.5
1e-03	-213.3	-112.1	-124.0	-45.3	-64.6	-311.1	-56.8	-32.4	-271.8
1e-02	-224.0	-119.3	-134.8	-48.8	-71.7	-318.2	-64.0	-39.5	-286.1
1e-01	-234.7	-126.4	-145.5	-52.4	-78.9	-325.4	-71.1	-46.6	-300.4
15	-258.0	-142.0	-168.8	-60.2	-94.4	-340.9	-86.6	-62.2	-331.4
200	-270.1	-150.0	-180.8	-64.2	-102.5	-348.9	-94.7	-70.2	-347.5
2000	-280.8	-157.1	-191.5	-67.8	-109.6	-356.1	-101.8	-77.4	-361.8
6000	-285.9	-160.5	-196.6	-69.5	-113.0	-359.5	-105.2	-80.8	-368.6
$\Delta_f G^T(P)$	-371.6	-221.9	-280.5	-108.4	-174.0	-422.3	-166.6	-142.9	-479.3

Another aspect, which we ignore in the design of the experiment, is that during exposure the sample surface is converted into reaction products, i.e., less metal atoms per m^2 are available as reaction partners as the exposure progresses. Our scaling law, which assumes that scenarios with the same $(p \cdot \Delta t)$ yield similar effects, may no longer be valid, if the chemical reaction region extends deep into the interior of sample as the transport of iodine within the solid will very likely depend on Δt despite the same T. Thus, the exposure experiments conducted are the more representative for the long-term exposure to iodine under space conditions, the thinner the surface region where the chemical reaction takes place. As will be seen later, this condition is fulfilled for all samples analyzed in this work. The maximum thickness found after treatment with the harshest conditions (scenario 4) is about 20 µm.

The assumption that the saturation pressure of iodine is independent of the presence of Ar in the gas mixture inside the reaction vessel is an approximation only. The presence of an argon atmosphere alters the phase diagram of iodine only slightly. The correlation between saturation vapor pressure p^* and the total pressure p_{tot} in a gas mixture is expressed by the inequality

$$\frac{\delta \ln(p^*)}{\delta p_{\mathrm{tot}}} \geq 0. \tag{4.8}$$

Equation 7 shows that by increasing p_{tot} the vapor pressure may increase. Hence, the iodine vapor is possibly somewhat denser in the presence of the argon atmosphere in the exposure experiments than it would be in the presence of vacuum. This implies that the damage in space due to corrosion will be slightly overestimated.

In summary, the reaction of iodine with a sample depends mainly on the collision frequency and the chemical potentials. In case of metals reacting with iodine, the impact of the partial pressure p and the type of species I_2 or I on the chemical potentials and thus on the likelihood of the reaction taking place is rather small as the reactions are very exergonic. Thus, samples treated in scenarios A and B according to the relation $(p_A \cdot \Delta t_A) = (p_B \cdot \Delta t_B)$ where p_i $(i = A, B)$ is the iodine pressure and Δt_i the exposure time in each case will not show quite the same degree of corrosion despite the same number of collisions of iodine molecules with the surface during exposure. However, the discussion shows that the degree of erosion of the sample treated in scenario A must be higher than in scenario B, if $p_A > p_B$. Therefore, our approach of mimicking the damage at low pressure p_B and long duration Δt_B (i.e., during a space mission) by exposure experiments at higher p_A and shorter duration Δt_A (i.e., in the laboratory) yields an upper limit for the degree of damage caused during the space mission, as the assessment of the damage is based on the sample treated in scenario A. In this sense, simulating long-term and low-pressure cases in space by short-term and high-pressure cases in laboratory is justified. However, it needs to be kept in mind that the results give an upper boundary for the severity of the corrosion effects, i.e., this intrinsically gives a safety margin.

4.3.4 Experimental setup

We studied a variety of elemental metals as well as metal alloys. The composition of the metal alloys are listed in Table 3.

Iodine exposure experiments were conducted in four different scenarios corresponding to four different $(p \cdot \Delta t)$ values to mimic space flights of 10 years in environments with iodine partial pressures of 1e-4, 1e-3, 1e-2, and 1e-1 Pa. A comparison of the conditions in space and those used to simulate them in the laboratory are given in Table 4. It should be noted that the realization in the laboratory employs a gas mixture of iodine and argon. The partial pressure p of I_2 in the reaction vessel is listed in the table, that of Ar was constant at about 10^5 Pa in all scenarios. As discussed in the previous section, the presence of Ar does not affect the outcome of the experiment.

The workflow of the exposure experiments including the subsequent XPS characterization is shown in Figure 4.11. The metallic samples with sizes of 11 mm × 11 mm × 2 mm were ultrasonically cleaned in isopropanol, prior to inserting them into the glass reaction vessel. The desired amount of solid iodine was added. The entire loading process took place at ambient temperature inside a glove box with a dry Ar atmosphere to exclude contact of the samples and the high-purity iodine with air and humidity as, in particular, iodine is hygroscopic [105]. The iodine used was provided by Th. Geyer Company was of 99.999 % purity. The argon atmosphere inside the glove box was not directly monitored; however, a flow of pure argon and a bowl of dry beads reduced the O_2 and H_2O content to a minimum. After loading, the glass reaction vessel inside the glove box was sealed with a glass lid and a rubber seal. Thus, it contains the Ar atmosphere, the samples, and the solid iodine. The sealed reaction vessels were removed from the glove box and placed inside a preheated oven at 100 °C where the iodine evaporates (i.e., only partially in case of scenario 4) yielding the desired iodine partial pressures given in Table 4. After

Table 4.3: List of samples studied. Top list: stainless steel, aluminum, and titanium alloys of various compositions (data from ISO standards). Only the mass fractions of the dopant constituents are listed, not of the hosts, i.e., iron (Fe), aluminum (Al), and titanium (Ti). Bottom list: elemental metal samples and their purity (given by the supplier).

Alloy name	**Maximal mass fraction of alloy element**
Stainless steel	
1.4404	17.5 % Cr, 12.5 % Ni, 2.5 % Mo
1.4544	19.0 % Cr, 12.0 % Ni, 0.7 % Ti
1.4546	19.0 % Cr, 11.5 % Ni, 1 % Nb
1.4571	18.5 % Cr, 13.5 % Ni, 2.5 % Mo, 0.7 % Ti
1.4301	19.5 % Cr, 10.5 % Ni
1.4401	18.5 % Cr, 13.0 % Ni, 2.5 % Mo
Aluminum alloys	
EN AW-5754	0.2 % Zn, 3.6 % Mg, 0.1 % Cu, 1.3 % Si
EN AW-6082	0.2 % Zn, 1.2 % Mg, 0.1 % Cu, 1.3 % Si
EN AW-7075	6.1 % Zn, 2.9 % Mg, 2.0 % Cu, 0.4 % Si
Titanium	
Ti 2 (3.7035)	0.3 % Fe, 0.08 % C, 0.03 % N, 0.25 % O
Element Name	**Bulk Purity**
Elemental Samples	
Al	$>97.5\,\%$
Cr	99.99 %
Fe	99.5 %
Mo	$>98\,\%^*$
Nb	99.9 %
Ni	99.99+ %
Ta	99.9 %
W	$>98\,\%^*$

*based on our analysis of the XPS survey spectra

Table 4.4: Conditions in space and those used to simulate them in the laboratory experiments. In the laboratory experiments a gas mixture of iodine and argon is employed. The partial pressure p of I_2 in the reaction vessel is listed, that of Ar was about 10^5 Pa in all scenarios. In scenario 4, the ratio m/V fulfills the inequality in Eq. (2), i.e., $p = p^*$ for iodine

	Space conditions @ 100 °C		**Lab conditions** @ 100 °C		**Realization**	
	p [Pa]	Δt [y]	p [Pa]	Δt [min]	m [g]	V [mL]
Scenario 1	1e-4	10	15	36	1.3e-3	1062
Scenario 2	1e-3	10	200	30	1.74e-2	1062
Scenario 3	1e-2	10	2000	30	0.174	1062
Scenario 4	1e-1	10	6000	180	1	135

the desired exposure time, the sealed vessels were taken out of the oven for cooling down. Afterwards, the reaction vessel was transferred back into the glove box. There, the samples were removed from the vessel and stored in the Ar atmosphere to evaporate residual I_2. All characterization experiments took place in the absence of air, either inside the glove box or in vacuum. The gravimetric analysis was performed on the balance inside the glove box. In case of the XPS experiments, a transfer module was used to insert the sample into the XPS without contact to air and humidity.

The color photographs of the interior of the glass reaction vessel heated to 100 °C reveal how the optical transparency of the iodine vapor decreases and the purple color intensifies with increasing iodine partial pressure, when going from scenario 1 to 4. The right graph shows the plots of constant $(p \cdot \Delta t)$ which connect the laboratory conditions of scenario 1 to 4 with the corresponding space conditions.

The XPS measurements were conducted with a PHI Versaprobe II spectrometer at room temperature. A monochromatic Al-K_α (1486.6 eV) x-ray anode provides the excitation at an angle of 45° to the surface normal in an ultra-high vacuum environment (pressure of about 10^{-6} Pa). Narrow-range spectra of the core level signals were recorded with a pass energy of 23.5 eV at an energy resolution of 0.2 eV, while the survey spectra were recorded with a pass energy of 93.9 eV and an energy resolution of 0.8 eV. From each sample, narrow-range spectra were measured of the core levels O 1s, C 1s, and I 3d. Additionally, spectra of the core level regions of the constituting elements, e.g., Al 2p, Cr 2p, Fe 2p, Mo 3d, Nb 3d, Ni 2p, Ta 4f, Ti 2p, and W 4f depending on the sample composition, were recorded. Set of measurements were recorded at the surface of the sample, after 120 s, and after 240 s of Ar^+-etching with 1 kV acceleration voltage. The etching depth is in the order of nm (< 10 nm). Charge neutralization was achieved during etching and data collection by compensating the positive charges from the Ar^+-gun by negative charges from an electron-gun. The collected XPS data was analyzed using the CasaXPS™ software. The spectra $S_{\text{ref}}(E)$ and $S_{\text{treated}}(E)$ were post-referenced to the

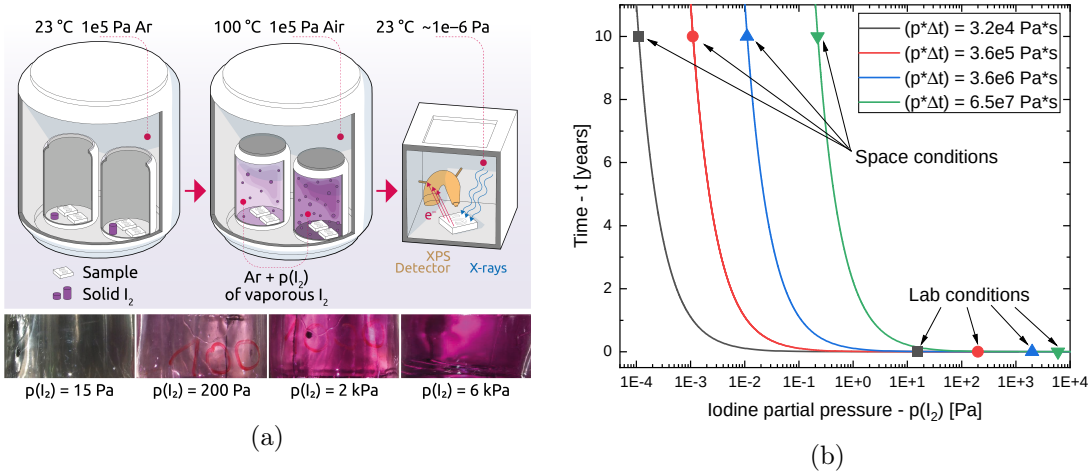

Figure 4.11: (a) Top: Workflow of the sample exposure to iodine and subsequent characterization by XPS. Bottom: Photographs of iodine vapor of different density inside the reaction vessels in scenario 1 (left) to 4 (right). The partial pressures of iodine realized are given below the photographs. (b) Plots of exposure time Δt versus logarithm of the iodine partial pressure p for constant $(p \cdot \Delta t)$ for the four test scenarios. Space conditions and laboratory conditions are indicated on the curves.

peak position of adventitious carbon (284.8 eV). All spectra were background corrected with a Shirley-background $B(E)$ and fitted with multiple Voigt-functions of a 60 % or 30 % Lorentz quota to analyze the energy position and area of the core level signals. The metallic signals were fitted with a Lorentzian asymmetric line shape according to the given references.

The spectra of the reference and iodine treated sample, $S_{\mathrm{ref}}(E)$ and $S_{\mathrm{treated}}(E)$, are combined to a difference spectrum $\Delta S(E)$ which highlights the changes caused by the iodine treatment. The difference spectrum is calculated as follows

$$\Delta S = \frac{2 \cdot [(S_{\mathrm{treated}} - B_{\mathrm{treated}}) - (S_{\mathrm{ref}} - B_{\mathrm{ref}})]}{S_{\mathrm{treated}} + S_{\mathrm{ref}}}. \tag{4.9}$$

The calculation of ΔS does not include any normalization, because it was not possible to generate comparable result for all materials. Consequently, the calculation procedure has the disadvantage that it does not compensate a reduced detection signal by a damping iodine layer. Thus, we generally expect a slightly negative area, if an iodine layer without chemical reaction in form of I_2 covers the surface.

The portions of solid iodine inserted into the reaction vessels and the metallic samples prior and after iodine exposure were weighed inside the glove box using a Mettler Toledo AB analytical balance with an accuracy of 0.1 mg.

The time-of-flight secondary ion mass spectrometry (ToF-SIMS) measurements for determination of iodine diffusion were performed with a M6 Hybrid SIMS instrument

(IONTOF GmbH) equipped with a 30 keV Bi cluster primary ion gun for analysis. All ToF-SIMS measurements were conducted in negative ion mode using Bi_3^+ ions as primary ion species since iodine forms predominately negative ions in SIMS analyses. The depth profiling was realized by using an additional dual-source column, which was operated with 2 keV Cs^+ in a non-interlaced mode (sputter current about 100 nA). Measurement cycle of ToF-SIMS depth profiling with alternating analysis and sputtering steps results in diffusion profiles, mass spectra, and 3D mass image maps. Charge compensation was realized by flooding the surface with low-energy electrons for 3 s between each analysis and sputtering step. The following signals were used for mass calibration: F^-,C_2^-,S^-,Cl^-,C_3^-,I_2^-. For analysis, the primary ion gun was operated in the spectrometry mode (bunched mode). This operation mode enables simultaneously a high mass resolution (FWHM $m/\Delta m > 6000$ at m/z 126.90 (I^-)) and high signal intensities. The primary ion current was about 0.6 - 0.65 pA and the cycle time was set to 70 µs. An analysis area of (50×50) µm^2 was chosen inside the (250×250) µm^2 crater (created with 40 frames per sputter step) and rasterized with 128×128 pixels at 1 shot per pixel and frame. The data analysis of the ToF-SIMS measurements was carried out with the Surface Lab Software version 7.2 (IONTOF GmbH, Muenster, Germany).

After the depth profiling, the sputter crater depths of the Scenario 3 samples were determined with a PLu neox 3D (Sensofar, Terrassa, Spain) confocal microscope. The obtained depth values were used to calibrate the sputter time axis and to determine the erosion rates for the different metals.

4.3.5 Results

Analysis of elemental metals

Figure 4.12 shows photographs of the elemental metal samples in the untreated state and after iodine treatment according to scenario 4, the roughest scenario, corresponding to 10 years of exposure in an iodine atmosphere of 0.1 Pa in space. The optical appearance of the elements Al, Fe, Ni, and Ti changed significantly during iodine treatment, suggesting that chemical reactions with iodine take place at their surfaces during treatment. The elements Cr, Mo, Ta, Nb, and W seem to have reacted much less with iodine, since their optical appearance did not change notably.

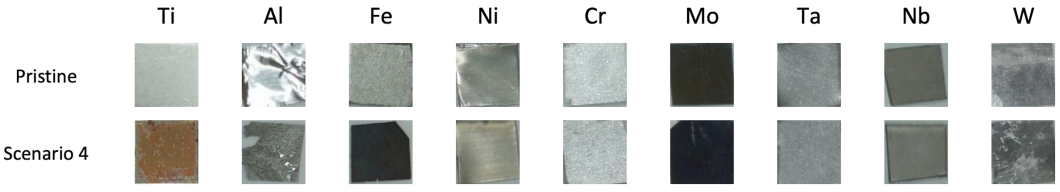

Figure 4.12: Photographs of the different elemental metals in the untreated state and after treating according to scenario 4.

Further clarification of the chemical effect of the presence of iodine in the atmosphere

surrounding the metal samples is obtained by comparing the XPS data of a corresponding untreated sample and one treated according to scenario 4 representing an upper boundary for 10 years in space in an iodine atmosphere of 1e-1 Pa. We do not expect iodine to react with the elements bonded to oxygen, since oxygen is a stronger oxidizing agent than iodine. Therefore, the focus during spectra comparison lies on the behavior of the elemental signal. Figure 4.13 shows three examples of samples which exhibit strong changes of the optical appearance on iodine treatment, i.e., Ti, Al, and Fe.

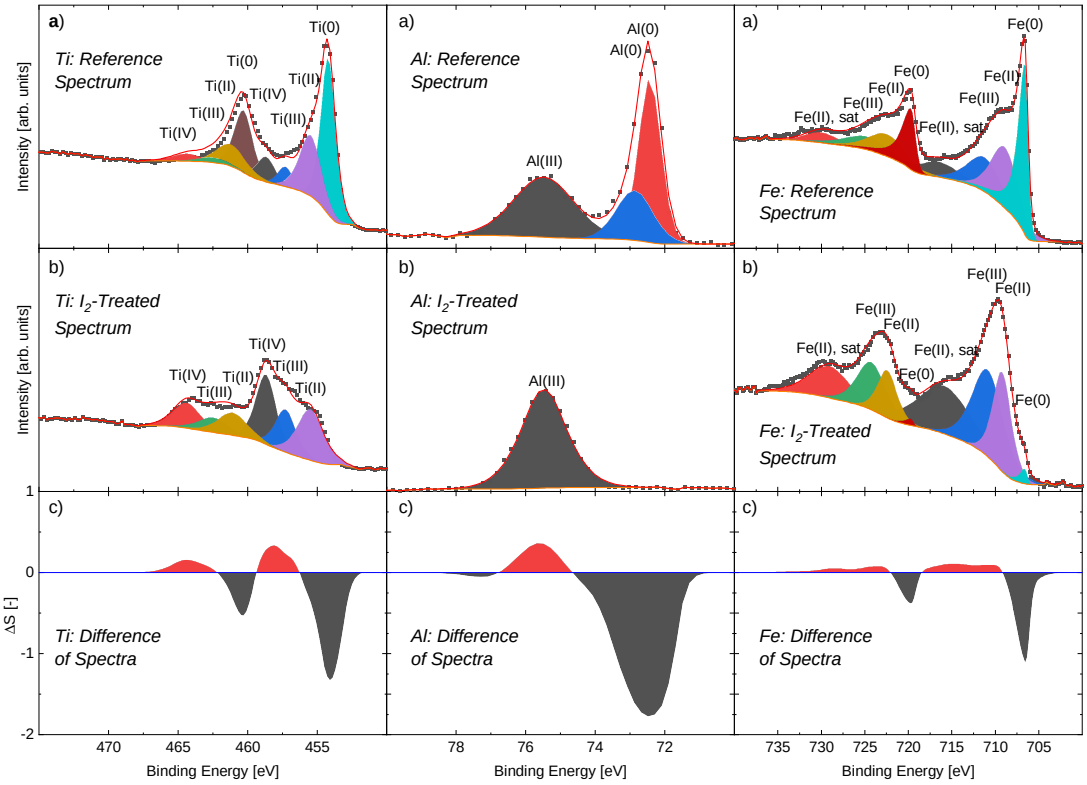

Figure 4.13: XPS spectra of Ti (left), Al (center), and Fe (right) recorded from (a) an untreated reference sample and (b) an iodine-treated sample according to scenario 4. (c) Shows the difference spectra according to Equation 4.9. The XPS spectra of Ti, Al, and Fe were recorded in narrow-ranges about the Ti 2p, Al 2p, and Fe 2p core level signals, respectively, after 240 s of Ar^+ etching.

The Ti sample showed the most severe changes of surface appearance after iodine treatment (see Figure 4.12). The XPS spectra of the treated and untreated Ti sample were recorded in the vicinity of the Ti 2p core level signals which are sensitive to the bonding environment and analyzed according to Ref. [106]. The XPS spectrum of the untreated Ti shows four spin doublets in the Ti 2p range. The turquoise peak (Ti(0)) with a binding energy (BE) of about 454 eV and the brown peak (Ti(0)) shifted by 6.1 eV

to higher BE values form the doublet $2p_{3/2}$ and $2p_{1/2}$ of metallic Ti. The black/red peak doublet (459 eV and 464 eV) is assigned to Ti(IV) oxide, i.e. TiO_2. The other two 2p doublets are indicative for other titanium oxides Ti(II), i.e. TiO ($2p_{3/2}$ at 456 eV, $2p_{1/2}$ at 461 eV) and Ti(III), i.e. Ti_2O_3($2p_{3/2}$ at 457 eV, $2p_{1/2}$ at 463 eV). On the surface without Ar^+ sputtering (spectrum not shown), the dominating oxide species is TiO_2 as expected for titanium stored in ambient atmosphere. The cleaning procedure (in an ultrasonic bath) used does not affect the oxide. A distinct signal of Ti(0) was also detected. The presence of different titanium oxides in the reference XPS spectrum shown is not surprising because the Ar^+ sputtering (here 240 s) causes preferential etching in case of TiO_2, i.e., the oxygen content is reduced in the ion etching process.

After treating the sample with iodine, the XPS spectrum has changed significantly. The spin doublet of the metallic Ti (Ti(0)) is no longer visible and the relative signal strengths of the other spin doublets is altered. The relative strength of signals of spin doublets of Ti with higher oxide numbers has increased. The disappearance of the metallic Ti(0) signals and an increase, especially, of the Ti(IV) signals are explained by the reaction of the sample with iodine as there is no additional oxygen in the reaction vessel present which may react with the sample. Thus, the alteration of the signals originate from to the formation of titanium iodides. For example, the increase of the Ti(IV) signal is explained by the formation of titanium(IV) iodide (TiI_4). TiI_4 is a red-brown solid, which agrees with the observation of the change of the optical appearance of the treated sample compared to the reference sample. The XPS trends can be seen even more clearly in the difference spectrum. The metallic signals strongly decrease (black curve), while the signals at positions where titanium iodides are expected experience a significant increase in signal strength (red curve). Thus, the XPS spectra reveal the strong reactivity of titanium with iodine despite the supposedly protective oxide layer. This is probably a sign that the native oxide has not formed a closed film.

Both elemental samples, that of aluminum and that of iron, also show distinct color changes after iodine treatment (see Figure 4.12). The XPS spectra for Al and Fe were recorded in the regions of the corresponding 2p major core level signals. The Fe spectra are evaluated according to Ref. [107] Since Fe has a very complex peak structure with multiple peak doublets for the species of Fe(0), Fe(I), Fe(II), Fe(III) and additional satellites (with partly overlapping BE values), we use a simplified model by fitting only one peak for Fe(0), Fe(I), and Fe(III). We also are considering only one satellite labeled as "Fe(II), sat". The fit of "Fe(II), sat" might include a satellite structure of Fe(III) which was not fitted separately. The Al spectra were analyzed following Refs [108, 109].

The XPS spectra of both reference samples again show signals characteristic for the corresponding native oxides in addition to the typical spin doublets of the metallic phase (i.e., $2p_{3/2}$ at 72 eV and $2p_{1/2}$ at 73 eV for Al(0); $2p_{3/2}$ at 707 eV and $2p_{1/2}$ at 720 eV for Fe(0)). In case of the untreated Al samples, the typical broad signature Al_2O_3 (Al(III)) is observed at 75.5 eV, whereas the untreated Fe sample shows spin doublets of FeO, i.e., Fe(II) ($2p_{3/2}$ at 709 eV and $2p_{1/2}$ at 722 eV) and Fe_2O_3, i.e., Fe(III) ($2p_{3/2}$ at 711 eV and $2p_{1/2}$ at 725 eV). After the iodine treatment, the spin doublets of the metallic phases are drastically reduced or even disappear in the corresponding XPS spectra, while

the detected signal of the spin doublets corresponding to higher oxidation states of the elements increase. Similar to Ti, Al and Fe can form iodides with high oxidation numbers of the metal ions, e.g., FeI_3 (Fe(III), black solid), FeI_2 (Fe(II), grey solid) and AlI_3 (Al(III), white solid). Thus, the signals of the metal oxides and metal iodides of the same metal oxidation state overlap. Consequently, the disappearance of the metallic signals in the XPS spectra of the iodine-treated samples and the increase of the XPS signals corresponding to the metal elements with higher oxidation states confirm the reactivity of Fe and Al with iodine despite an oxide layer. The findings are in accordance with change of the optical appearance of the iodine treated Al and Fe sample compared to the reference samples shown in Figure 4.12.

Weighing the samples of the three elemental specimens of Al, Fe, and Ti, discussed above, before and after the treatment showed a detectable change of weight. The titanium sample (416.0 mg) lost 0.9 % of its weight in form of red-brown material crumbs, i.e., TiI_4, after a treatment according to scenario 4. The treatment according to the scenarios 1 to 3 did not result in a detectable weight change of the corresponding Ti sample. The Fe samples (646.2 mg in scenario 3 and 721.1 mg in scenario 4) gained about 0.14 % of weight after the exposure to iodine according to scenario 3 and 0.35 % after treatment as stated for scenario 4. This suggests a strong reaction of the sample with iodine, forming an increasing surface layer of iron iodides. The light weight and much thinner Al sample (7.9 mg in scenario 3 and 4) with a thickness of 20 µm compared to the 2 and 1 mm of the Ti and Fe samples, respectively, experienced a weight gain of 10 % and 95 % after treatment according to scenario 3 and 4, respectively. However, the high surface-to-volume ratio of the Al foil in conjunction with the small atomic mass of Al explains the very high relative weight gain when the aluminum iodides such as AlI_3 surface layers are formed. XPS results, optical inspection as well as the weighing results agree well and corroborate that all three metals Al, Ti, and Fe strongly react with iodine.

The narrow-range spectra of the major core level signals Cr 2p, Ta 4f, W 4f (shown in Figure 4.14) were evaluated based on the Refs [107] for Cr [110, 111], for Ta, and [110] for W. Reference and treated sample of all the three metals exhibit a similar behavior. In all three cases, the surface spectrum prior to Ar^+ etching shows a weak metallic signal along with signals of corresponding metal oxides. The signals of the compound with the metal in the highest oxidation state (i.e. Cr(III) hydroxide (Cr(III) $2p_{3/2}$: 577.2 eV), Ta_2O_5 (Ta(V) $4f_{5/2}$: 26.4 eV), and WO_3 (W(VI) $4f_{7/2}$: 35.8 eV)), dominate the XPS spectrum. After Ar^+ etching, the oxide compounds at the surface are removed and the asymmetric metallic peaks dominate the spectra, i.e. Cr(0) at 574.2 eV, Ta(0) at 21.2 eV, and W(0) at 30.9 eV. The iodine treatment has no effect on the XPS spectra. Oxide compounds are detectable prior to Ar^+ etching. However, after Ar^+ etching the metal signals of oxidation number 0 dominate. The iodine content (in molecular form) on the samples after etching was 14 at. % (Cr-sample), 5 at. % (Ta-sample), and 7 at. % (W-sample) at the surface. The difference spectra of all three samples underline again that iodine treatment has almost no effect on these specimens.

The surface of the Ni sample after iodine treatment shows a change of optical appearance compared with the surface of the reference sample (see Figure 4.12) which suggests

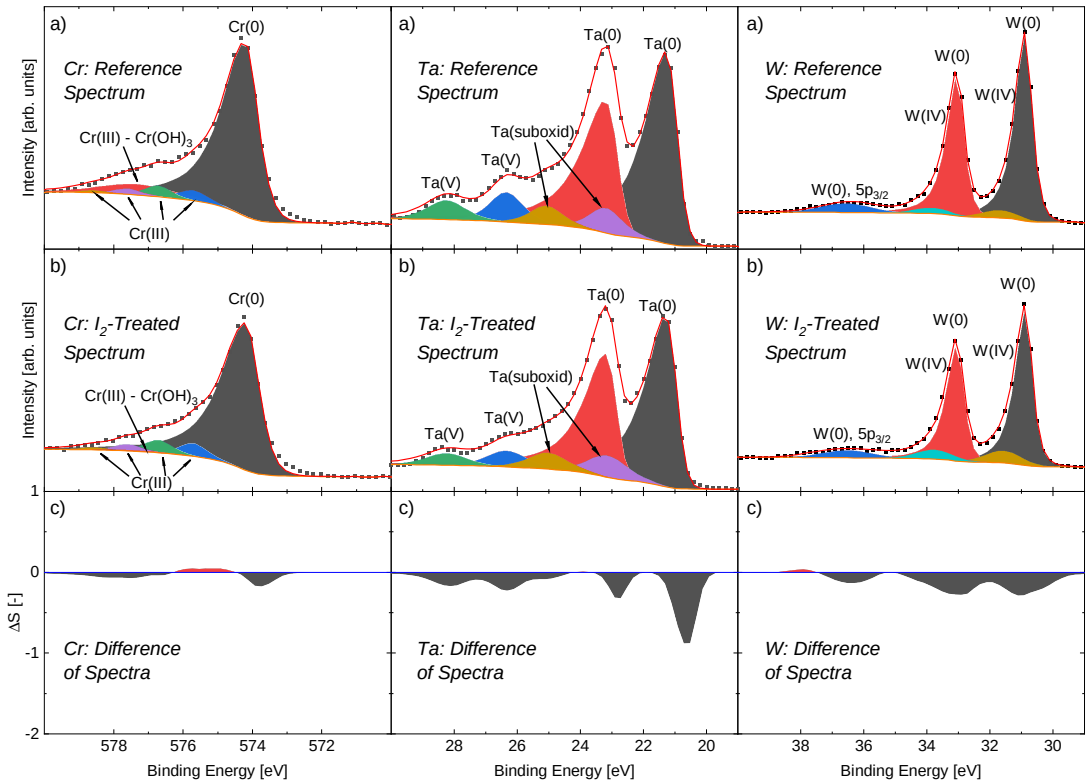

Figure 4.14: XPS spectra of Cr (left), Ta (center), and W (right) recorded from (a) an untreated reference sample and (b) an iodine-treated sample according to scenario 4. (c) Shows the difference of spectra according to Equation 4.9. The XPS spectra of Cr, Ta, and W were recorded in narrow-ranges about the Cr 2p, Ta 4f, and W 4f core level signals, respectively, after 240 s of Ar^+ etching.

that the sample has reacted with iodine. However, a close analysis of the XPS spectra taken in the Ni 2p region (Figure 4.15), revealed no difference between the reference and treated sample. The XPS spectra of the reference and the treated sample were fitted based on parameters given by Biesinger [112]. In both spectra, the Ni $2p_{3/2}$ region shows only the main metallic signals (Ni(0) at about 853 eV). None of the detected peaks arise from Ni in a higher oxidation state, e.g. Ni(II) of NiI_2 [113]. However, a distinct iodine signal was detected in the I 3d region at 619.6 eV (not shown) indicative for molecular iodine. Even after 240 s of Ar^+ etching, the iodine made up about 24 at. % of the detected elements. The surface spectra (prior to Ar^+ etching) showed typical oxide and metallic peak structures of Ni. Therefore, Ni seems to be resistant against the iodine treatment and did not form iodide compounds. The change in optical appearance of the Ni is therefore attributed to a deposition of molecular iodine on the surface.

The model for fitting the Mo 3d XPS region is based on the publication by Alov [110].

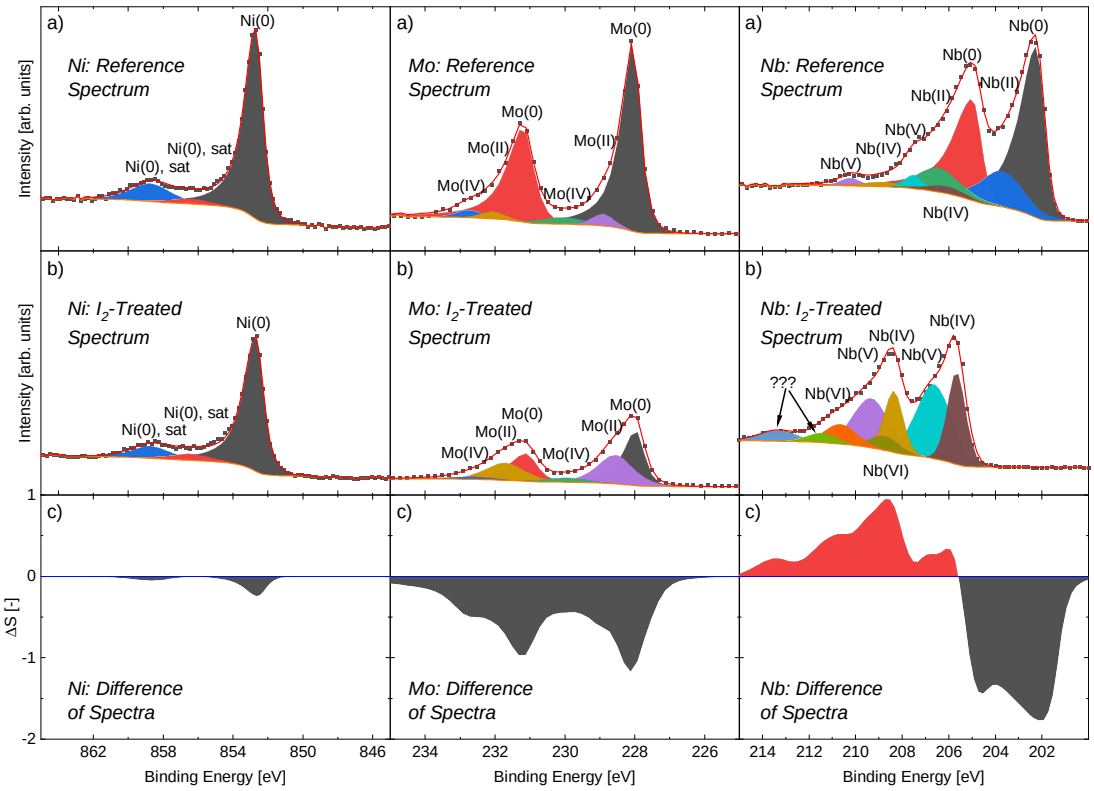

Figure 4.15: XPS spectra of Ni (left), Mo (center), and Nb (right) recorded from (a) an untreated reference sample, (b) an iodine-treated sample according to scenario 4. (c) Shows the difference of spectra according to Equation 4.9. The XPS spectra of Ni, Mo, and Nb were recorded in narrow-ranges about the Ni 2p, Mo 3d, and Nb 3d core level signals, respectively, after 240 s of Ar^+ etching.

The character of the changes of the XPS spectra is similar to those of the metals Cr, Ta, and W in the sense, that the XPS spectra recorded at the surface prior to Ar^+ etching show strong oxide-related peaks in the same spectral region as those of metallic species.

Prior to Ar^+ etching, the XPS spectra (not shown in the figure) recorded on the surfaces of the reference and the iodine-treated sample exhibit a signal corresponding to Mo(IV) in MoO_2, which dominates over a small metallic peak Mo(0). After 240 s of Ar^+ etching, as can be seen in Figure 4.15, the metallic peaks (Mo(0) $3d_{5/2}$: 228.0 eV) dominate and multiple oxide peaks with lower oxidation number (Mo(II), Mo(IV)) occur in the spectra of both, the reference and the iodine-treated sample. The intensity ratio of the Mo(0) signal and the Mo(II) signal in the iodine-treated sample is somewhat smaller than in the reference sample, but the Mo(0) signal is still dominant. The corresponding difference spectrum shows a distinct negative area which reflects the significant difference in signal strength between the iodine-treated and the reference XPS spectrum. The detected Mo

3d signals from the treated Mo sample are much lower, about 20 % of the corresponding reference signals. The amount of molecular iodine detectable in the sample region studied by XPS was about 26 at. % after iodine treatment. The presence of iodine damps the Mo XPS signals obtained in case of the treated sample, which is not compensated by the calculation procedure of the difference spectrum (ΔS). Since the difference spectrum does not show a positive area nor a peak movement, the overall differences of the reference and iodine treated spectrum is small and let us conclude that Mo, if at all, only weakly chemically reacts with iodine.

The XPS spectra of Nb 3d region were interpreted following the peak assignments Yang et al. [114] and Geyer-Lippmann et al. [115]. The recorded surface XPS spectra of the iodine-treated and the reference sample (not shown) are almost identical. In both cases, the peak structure is similar to the XPS spectrum reported by Yang et al. [114] for Nb-samples exposed to molecular oxygen (air). The dominant peak doublet of Nb(V) (Nb(V) $3d_{5/2}$: 207.1 eV) is assigned to Nb_2O_5, while the less pronounced peak doublets are representing NbO_2 (Nb(IV)) and NbO (Nb(II)) compounds as well as metallic Nb (Nb(0) $3d_{5/2}$: 201.7 eV). After 240 s of Ar^+ etching, the peak structure of the reference sample shifts towards lower BE values. The dominant XPS signal is now the metallic Nb(0) doublet. However, weaker signals of Nb(II), Nb(IV), and Nb(V) can also be seen in Figure 4.15. In contrast, the XPS spectrum of the iodine-treated Nb sample after 240 s of Ar^+ etching is dominated by the double peak structure of Nb(V) and the Nb(0) doublet has vanished. Furthermore, multiple additional peak doublets appear either side of the Nb(V) doublet peaks. In particular, the relative increase in signal strength of the Nb(IV) doublet peaks compared to the other signals suggests that NbI_4 is formed in addition to the residual NbO_2 also present in the reference sample. The signals marked by question marks at higher BE values of about 212 eV and 214 eV are tentatively assigned to Nb in oxidation states larger than $+5$, which is somewhat uncommon for metallic samples after etching. Nevertheless, similar observations were made by Geyer-Lippmann et al. [115] in their analysis of various niobium-iodides. Those authors have assigned the additional peaks to higher oxidized compounds and oxide iodides. Thus, Nb seems not to react with an iodine atmosphere when treated according to scenario 4, since the surface spectra of the treated and reference sample look identical, including the metallic peak. Nevertheless, the combination of Ar^+ etching and prior iodine treatment changes the surface structure in an untypical way for metallic samples. Hence, Nb is not really inert to reactions with iodine.

Analysis of alloys

In the previous section, we have shown that the main constituents of most metal alloys such as Al, Fe, and Ti strongly react with iodine, while the majority of tested minor constituents of the alloys such as the elements Cr, Ni, Mo, W, or Ta are not affected by the iodine treatment. In our experiments, all alloy samples studied (stainless steel and aluminum alloys) eventually changed their optical appearance with extended iodine exposure, as presented in Figure 4.16, suggesting chemical reactions with iodine. However, none of the treated samples shows any visual change of appearance when treated with

iodine according to scenario 1 and 2. Treatment in scenario 3 leads to an obvious color change of some of the samples, e.g., the stainless-steel sample 1.4544 or the aluminum alloy AW-7075. The survey XPS spectra of many of the samples show a distinct iodine signal, proving the iodine contamination of the surface. Thus, the amount of iodine must reach a certain threshold to have a distinct visual effect on a sample, since the different treatment scenarios do not change the chemical reactions between iodine and the respective elements, as explained in in the first section. The color change is a strong indication that an iodine related layer with thicknesses at least a couple of hundred nanometers forms at the surface during treatment.

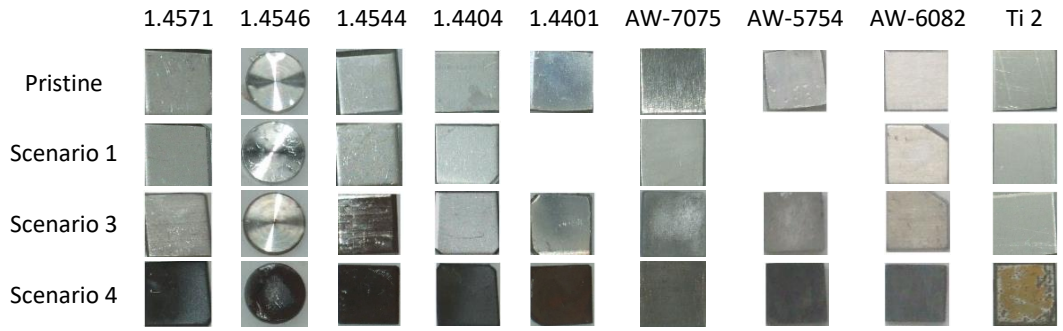

Figure 4.16: Alloy samples (1.XXXX - stainless steel alloys, AW-XXXX - aluminum alloys) after an iodine treatment according to the different scenarios.

To examine the thickness of the surface layer and the iodine diffusion behavior, ToF-SIMS depth profiling was applied. For these measurements, the samples Ti 2, AW-7075, and 1.4544 were selected as representative of the three materials groups, i.e., titanium, aluminum alloy, and stainless steel. Furthermore, the selected samples are those exhibiting the strongest color change in their respective material group. Therefore, we assume that they are most affected by the iodine treatment. For evaluation of iodine diffusion, the diffusion profiles of the I^- signal were used. Figure 4.17a) depicts the recorded depth profiles of the I^- signal of the samples of the selected material groups treated according to the scenarios 3 and 4, respectively. Near the surface, all diffusion profiles start with a flat, relatively constant iodine signal, which we assign to an iodine layer on the surface. The depth ranges where iodine signals are detected with constant intensity agree with the corresponding values of the surface roughness of the samples. This finding somewhat suggest that the depth range does not correspond to the layer thickness of the iodine surface layer, but is rather caused by the surface roughness which leads to a partial screening of the surface from the ion beam used for etching. Therefore, we believe that the surface coverage by iodine is much thinner.

Below, iodine diffusion within the bulk surface is shown. Here, the I^- signals decrease rapidly (almost exponentially) with increasing depths until constant background signal intensities of I^- are reached. In depth ranges prior to approaching the background signal, the iodine signal decreases more slowly with depth (i.e., the slope in the logarithmic plot,

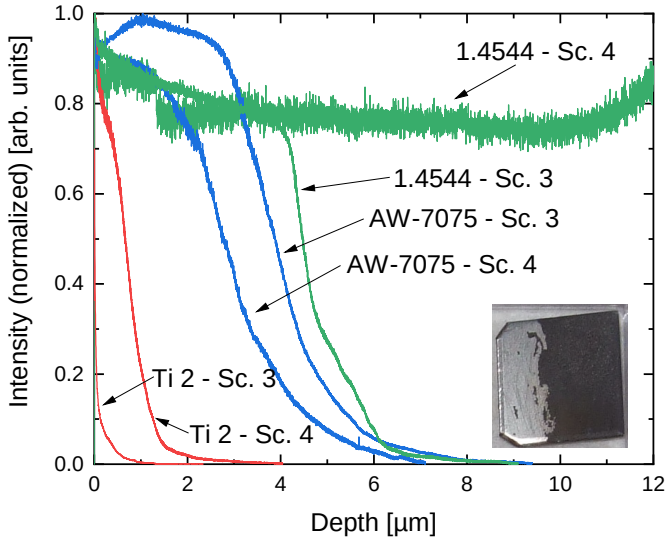

(a)

Sample (Treatment Scenario)		Surface layer thickness [µm] profilometer (ToF-SIMS in italics)
Ti 2	(3)	*1*
	(4)	*2*
1.4544	(3)	~9 ; 8
	(4)	19.5
1.4571	(4)	6.6
1.4404	(3)	3.4
	(4)	10.8
1.4401	(4)	15.8
AW-7075	(3)	*7*
	(4)	*9*
Fe	(4)	7.9

(b)

Figure 4.17: (a) ToF-SIMS surface depth profiles show the iodine diffusion behavior of the iodine-contaminated samples Ti 2 (red), AW-7075 (blue), and 1.4544 (green), treated according to scenarios 3 and 4. The inset shows the sample 1.4404 as prepared for the profilometer measurements. (b) Thickness of the discolored surface layers using ToF-SIMS and profilometer measurements of samples treated according to scenarios 3 and 4.

not shown, becomes flatter). These signals are probably due to iodine atoms diffusing along grain boundaries, since the activation energy of this migration process is lower than that for lattice diffusion in the bulk of the grains [116].

The iodine signal detected for the stainless-steel sample 1.4544 (treatment scenario 4) shows a different diffusion behavior. Throughout the complete depth profile of about 12.4 µm, the signal intensity of iodine does not decrease, suggesting that iodine could diffuse deeper than 12 mm into the sample. Therefore, in a subsequent measurement, we removed the chemically reacted, black surface layer with a paper towel on parts of the sample's surface until the shiny metallic surface reappeared. The detected height difference between the dark treated surface and the shiny cleaned surface area is about 19.5 µm (see Figure 4.17b)) and marks the maximal depth of the eroded surface layer. We believe that the chemical reaction between iodine and iron oxide at the surface destroyed the surface morphology, since a reaction between these two reactants is accompanied by a significant volume change that cracks grain boundaries and enables additional iodine to diffuse to larger depths [98].

The iodine diffusion depth for all samples analyzed is in the range of a few tens of µm only, which is, in comparison to a total sample thickness of 1 - 3 mm, not significant. Corrosion of the metals and metal alloys by iodine can be considered a surface effect and does not affect the integrity of the bulk of the material. Therefore, it can be assumed

that the stability of macroscopic structural elements of the satellite made of such metals or metal alloys will be given for the entire duration of the mission.

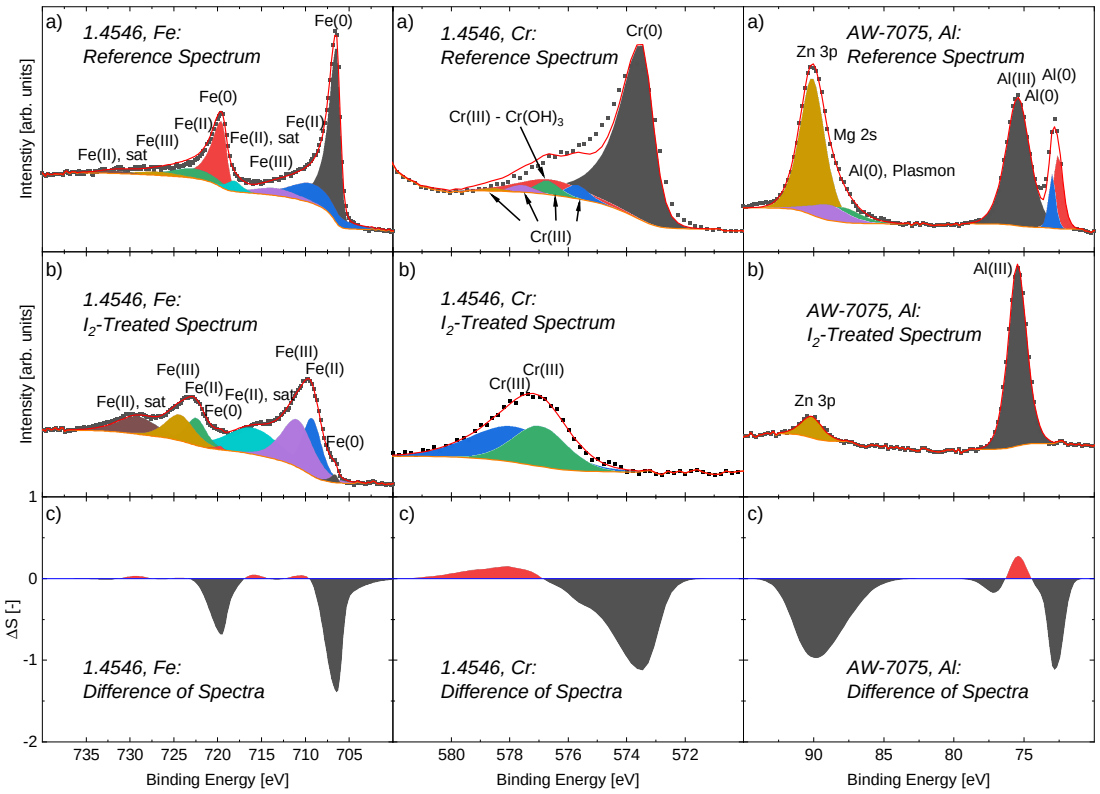

Figure 4.18: Fe 2p and Cr 2p XPS spectra (left and center) recorded from (a) an untreated and (b) an iodine-treated piece of stainless steel 1.4546 sample. Al 2p XPS spectra (right) recorded from (a) an untreated and (b) an iodine-treated Al-based metal alloy EN AW-7075 sample. The iodine treatment corresponds to 10 y in 1e-1 Pa iodine partial pressure (scenario 4). The corresponding difference spectra (c) are shown below.

For a detailed analysis of the chemical reactions, the stainless steel samples 1.4546 and 1.4544 were closely analyzed using XPS prior and after iodine treatment according to scenario 4. An untreated sample served as reference sample. We attempted to record narrow-range spectra of the major core level signals of all elemental constituents of the stainless steel alloy. Unfortunately, only signals of the elements present in larger quantities, i.e., Fe, Cr, and Ni were detectable. An adequate Ni 2p signal was only measured for the reference samples and will not be further discussed. The recorded XPS spectra from the sample 1.4546 are shown in Figure 4.18 for the Fe 2p and the Cr 2p region (note, the XPS spectra of the stainless steel 1.4544 show the same trends and are not discussed further). As expected based from the analysis of the elemental metals, the Fe 2p signal of the reference sample shows three spin-doublets and a pair of satellites after

240 s of Ar^+ etching. The strongest doublet (purple and yellow) originates from Fe(0) of metallic iron, while the other signals originate from higher oxidation states of iron, i.e., Fe(II) and Fe(III). In the XPS spectrum of the corresponding iodine-treated sample, the Fe(0) doublet has virtually disappeared and the Fe(II) and Fe(III) doublets dominate indicating that Fe has reacted with iodine forming, e.g., FeI_2 or FeI_3, as discussed in the elemental metals section. The corresponding Cr 2p XPS spectrum recorded from the untreated sample 1.4546 agrees with that recorded from the untreated elemental Cr-sample (see Figure 4.14), including a spin-doublet representing pure chromium. In contrast, the analysis of the Cr 2p core-level XPS spectrum of the iodine-treated stainless steel sample 1.4546 differs from that of the iodine-treated elemental Cr sample in Figure 4.14. The iodine-treated stainless steel sample exhibits no Cr(0) signal in its XPS spectrum, but only two spin doublets at higher BE values both assigned to Cr(III) $2p_{3/2}$. Thus, it seems that Cr atoms in the alloy react and form bonds with iodine other than in the elemental Cr metal. This finding suggests that the chemical reaction of an element with iodine is not only to depend on the element itself, but also on the nearest-neighbor atomic environment. On the one hand, this makes it difficult to judge the iodine-resistance of an alloy solely by the properties of its elemental constituents. On the other hand, there is also a certain probability that in alloys exist which are inert to iodine.

Samples of the Al-based alloy EN AW-7075 were also analyzed by XPS. The narrow range Al 2p spectra of the reference and iodine-treated sample after 240 s of Ar^+ etching are shown on the right of Figure 4.18. The Al 2p signals in the XPS spectra of both samples behave similarly to the signals recorded on comparable elemental Al samples presented in Figure 4.13. The peaks representing aluminum in the metallic state Al(0) disappear after iodide treatment and only one Al 2p peak remains, which represents aluminum oxide or iodide. In contrast to the elemental spectrum after iodine treatment, a significant peak at the high BE side confirms the presence of the alloy elements Mg and Zn. The detected peak comprises contributions from signals of Zn 3p, Mg 2s, and an Al-plasmon (also shown in the Al elemental spectrum). It is worth noting, that the intensity of the elemental constituents Mg and Zn drastically decreases with increasing duration of the iodine treatment, suggesting that they are removed by an erosion process. The aluminum alloy chemically reacts with the iodine as it was expected based on the analysis of the elemental Al sample. The comparatively high mass fractions of the minor elemental constituents do not provide protection of the aluminum. On the contrary, the results show that iodine severely erodes aluminum alloys. Therefore, stainless steel alloys should be favored over aluminum alloys when a usage in iodine-environments is anticipated.

Conclusion

Using iodine as propellant for electric propulsion systems has many advantages. The chemical reactivity of iodine is commonly considered as the major disadvantage. Hence, materials for structural parts of a satellite have to be carefully selected or protected. We define and justify a measurement protocol enabling us to mimic the conditions experienced by satellite components in typical mission scenarios of satellites propelled with iodine-fed electric thrusters and to extract an upper limit for the damage caused during a 10-year

mission. In such dry, non-humid environments with low-iodine partial pressures below 1e-1 Pa and anticipated mission durations of 10 years, the elemental metals such as Cr, Mo, Ni, Ta, and W are resistant against iodine in its elemental form. However, Nb, Al, Ti, and Fe similar to Cu [45, 52–54] strongly react with iodine under these conditions. Our results confirm the findings of Beck et al. [117] that the reactiveness towards iodine decreases from Fe via Ni to Cr. In case of Al and Ti treated by these conditions, the chemical reaction products even cause brittleness of the surface and deterioration of the structural integrity of the material in the vicinity of the surface. Nevertheless, the corrosion can be considered a surface effect despite the long duration of the mission. The maximum depth of the corroded layer in the samples studied was about 20 µm for stainless steel treated according to the harshest scenario 4. We also studied metal alloys, in particular, various stainless steels and aluminum alloys. The main elemental constituents of the two types of alloys, Fe and Al, both react with iodine. In case of the Al alloy studied, the elements acting as minor constituents of the alloy are Zn, Mg, and Cu which all three can react strongly with iodine [51, 118]. Thus, it is not surprising that the aluminum alloy basically behaves like the elemental Al metal under iodine treatment. Alloying with minor fractions of iodine-resistant elements such as Cr, Mo, Ni, Ta, or W, as it is done in case of stainless steels 1.4546 (with Cr, Ni, Nb) and 1.4546 (with Cr, Ni, Ti), cannot remedy the effect of iodine on the main stainless steel constituent Fe. It even turns out that Cr in stainless steel reacts with iodine, although it is resistant to iodine in Cr metal. This reflects the basic knowledge that the reactivity of chemical element at given conditions not only depends on the reaction partner (here iodine), but also on the element's atomic nearest-neighbor environment. In other words, surrounding a Cr atom by other Cr atoms as in the corresponding metal constitutes a stable environment suppressing the reaction with iodine. A change of atomic environment of a chemical element may either strengthen or weaken its resistance to reacting with iodine. Following this line of reasoning implies that it cannot be ruled out that an iodine resistant material may be obtained by atomic alloying, however, such alloy compositions have not been identified yet. An option may be high-grade alloy steels with high fractions of the resistive constituents Cr, Mo, Ni, Ta, and W such that the Fe nearest-neighbor environment is significantly altered compared to Fe metal. A possible candidate for such an alloy is stainless steel 1.4536 (X1NiCrMoCu25–20-5), which should be investigated. Another rather self-evident option of improving the resistance of a metal or metal alloy to iodine is applying a protective surface coating with an iodine-resistant metal such as Cr, Mo, Ni, Ta, or W or a closed oxide film. It is of paramount importance that such a protective surface coating is dense and closed. In particular, our experiments show that the native oxides, for example, in case of Al are not sufficient to suppress a reaction between iodine and Al. As oxygen is a stronger oxidizing agent than iodine, this shows that the native Al_2O_3 layer is not dense enough to provide a suitable protection layer as it can be overcome by iodine. However, we have shown that the deteriorating effect of iodine is basically nonexistent even for highly reactive materials such as Ti or Al at low iodine partial pressure below 1e-3 Pa at an anticipated exposure time of 10 years (scenario 1 and 2). Since higher partial pressures of iodine are only expected inside the propellant feed system and the thruster, the principal satellite

structures and components should not be affected by the surrounding iodine atmosphere and do not need adaptation.

In conclusion, all elemental metals and metal alloys studied are only affected by iodine in a thin surface layer anticipating a space environment with an iodine partial pressure of 1e-1 Pa and a mission duration of 10 years. The structure of the bulk of the metals studied is not affected, only the optical appearance is altered. This implies that macroscopic structural elements of the satellite made of those metals should preserve their stability for the entire duration of the mission. Furthermore, several metals are in these dry reaction conditions basically inert to iodine even over the long time span of a typical space mission duration. The possibilities of identifying additional iodine resistant alloys and of applying protective coatings of iodine-resistant metals or other materials offers various ways of overcoming the challenge of iodine reactivity on components exposed to a dense iodine atmosphere on satellites or other spacecraft equipped with iodine-fed thrusters.

4.4 Additional results

4.4.1 Behavior of epoxy resins on iodine exposure

The material group of fiber-reinforced polymers are composite materials consisting of a fiber (carbon or glass) and an epoxy resin. The materials have a very good weight to tensile strength ratio. Thus, they are especially interesting for all applications where the weight is limited such as for spaceflight, aircraft, boats, or automobiles. On a spacecraft propelled with iodine, the behavior in contact with iodine of all implemented materials must be known to ensure safety on long mission durations.

In this section, three different epoxy materials are treated in an iodine atmosphere according to the previously defined treatment scenarios 1 to 4 (see Table 4.5). The samples 201257 and 200743 were treated at 50 °C because they cannot sustain temperatures of 100 °C.

Table 4.5: List of epoxy resins tested in contact with iodine vapor at the given treatment temperature $T_{\text{Treatment}}$.

Name	Full name	$T_{\text{Treatment}}$	Composite
G-Epoxy	Glass Woven Epoxy G11	100 °C	Glass fiber and resin
201257	L20/EPH960	50 °C	Resin without fiber
200743	LY556/HY906/DY070	50 °C	Resin without fiber

Figure 4.19 shows images of the samples before and after the respective iodine treatment. The G-Epoxy sample changed its color from green (pristine) via dark green (after scenario 3) to black (after scenario 4). The color change is accompanied by a weight gain of 0.6 % after treatment scenario 4. Sample 201257 showed a similar behavior. The sample turned from transparent (pristine) to black after the last treatment scenario with

a weight gain of 1.3 %. Iodine diffused into the G-Epoxy and 201257 samples and fully penetrated the bulk material with unknown effects on the mechanical properties.

However, the samples of 200743 did not experience any color change nor a weight gain during the treatment scenarios.

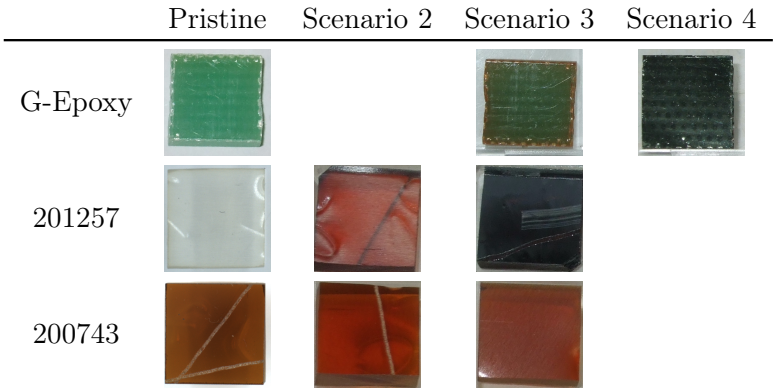

Figure 4.19: Epoxy resin samples treated with iodine according to the the different treatment scenarios 1 to 4.

All three materials were analyzed by XPS after the last treatment scenario. Independent of the different behavior in color change and weight gain, the XPS spectra showed the same results for all treated materials. About 90 at.% of the measured elements in the survey XPS spectra (Figure 4.20a) is carbon, while the remaining 10 at.% are due to the elements I and O. The spectra of the core level signal I $3d_{5/2}$ in Figure 4.20b shows two peaks. The first peak in the spectrum is assigned to molecular iodine I_2, while the second

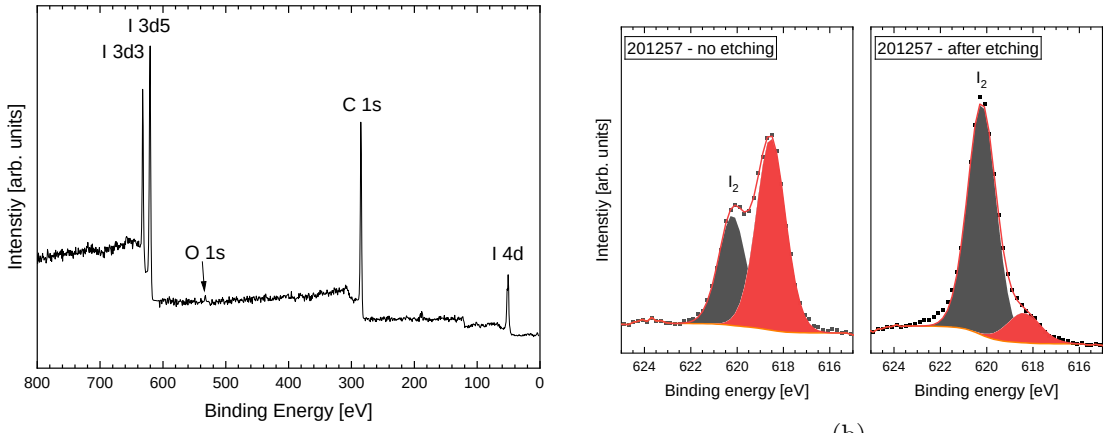

(a) (b)

Figure 4.20: XPS spectra of the sample 201257 after treatment scenario 3: (a) survey spectrum and (b) the core level signal I $3d_{5/2}$ before and after Ar^+ etching.

peak indicates a reaction between iodine and carbon, possibly CH_3I. The measurements

are not conclusive to identify specific molecular structures with certainty. Nevertheless, the reactions seem to be only a surface effect. After the argon etching the singular peak of molecular iodine dominates by far.

Iodine diffusion poses a threat to the stability and durability of fiber-reinforced polymers. Different types of resin seem to withstand iodine diffusion better than others. Using such materials on satellites equipped with iodine-fed thrusters may be possible but extra analysis of the iodine diffusion and mechanical properties must be conducted.

4.4.2 Metal samples after exposure to air

The corrosion of metals by iodine is influenced by the environment. Thus, the iodine treatment took place in carefully controlled atmosphere to simulate the space environment. After the final analysis of the samples they were stored for several moths inside the protective argon atmosphere of a glovebox. During this time all samples maintained their coloring state as shown in the figures 4.12 and 4.15. After removing the samples from the glovebox and exposing them to the ambient atmosphere, some of the samples changed their optical appearance and, for them, the corrosion process continued for a few days. Images of the air exposed samples are shown in Figure 4.21.

Figure 4.21: Samples treated according to scenario 4 and after a few days of exposure to ambient conditions, i.e., humid air.

The Al sample as well as the not shown aluminum alloy samples did not change their appearance. The iodine already damaged the surfaces of the samples with severe erosion of the pure Al sample. This indicates that all iodine already reacted with the aluminum under space conditions. Titanium shows the same behavior. Entering air did not lead to any further surface deterioration.

On the contrary, all Fe containing samples experienced strong reactions after the contact to air. The Fe and stainless steel samples were covered by a black surface layer after the iodine treatment. With the exposure to air, the color changed rapidly to a rusty red-brown. Furthermore, all surfaces showed newly developed bumps and an increased surface roughness, which indicates an erosion of the samples. The most damaged sample is the Fe sample. After being exposed to air, the sample experienced severe erosion including pitting beyond the effects of the stainless steel samples. The partly cleaned surfaces of some of the stainless steel samples originate from the profilometer measurements. All other samples, not shown here, did not change their optical appearance.

These results illustrate the importance of mimicking space conditions by excluding oxygen and water from the atmosphere. The contact with air is especially damaging for materials containing Fe.

4.4.3 Ion beam sputter effects of iodine and xenon

Iodine propelled spacecraft are not only confronted with iodine vapor at different partial pressures but also with energetic iodine ions. Hence, the sputter effect of iodine ions must be investigated to assess the risk for spacecraft components. The material degradation caused by sputtering strongly depends on the setting given by ion energy, incident angle, ion mass, and sputter target. To fundamentally assess if iodine ions present a sputter problem, which might be enhanced by chemical reactions on the samples' surfaces as seen in Section 4.3, this experiment compares the sputter impact of xenon ions with that of iodine ions under comparable conditions. The sputter experiment is setup similarly to the sputter experiment described in Section 3.1.1 but here with the focus on a wide range of structural materials, including titanium, aluminum alloys, stainless steels, and epoxy resins.

The test chamber was the iPott and as ion source served a RIM-10, which provided ions with an energy of +1500 eV. The ion current density hitting the samples was detected (25 mA/cm^2) and the accumulated charge density (300 - 600 mAs/cm^2) over the sputter time of 30 - 80 min was kept equal for all materials. Therefore, for each material, a set of samples was fabricated, consisting of one iodine and one xenon sputtered sample, where half of the surface area was protected by graphite foil. Subsequently, the height difference between the sputtered and protected area of all samples was measured with a profilometer. The sputter yields, reflecting the lost surface atoms per incident ion, are calculated based on equations 3.1 - 3.3.

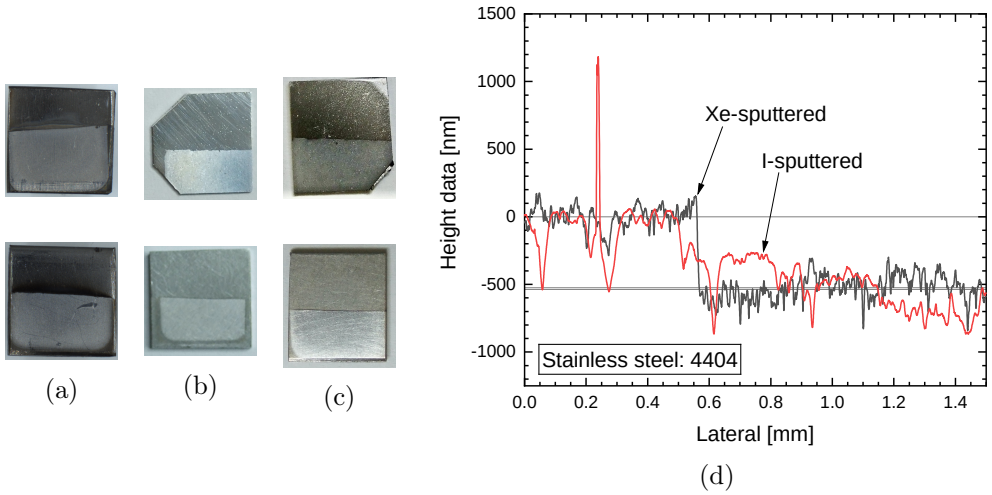

Figure 4.22: Exemplary samples sputtered with iodine (top) and xenon (bottom) for the materials from left to right: (a) AISI-316 (stainless steel), (b) Al7075 (aluminum alloy), and (c) titanium. (d) Surface profile of sample 4404 (stainless steel) of the xenon (black graph) and iodine (red graph) sputtered sample in comparison. The average surface heights of the protected (0 nm) and exposed surfaces are indicated (537 nm for iodine and 525 nm for xenon).

A selection of photographs of the resulting sample sets is shown in Figure 4.22a - c. All samples show clear differences between the areas exposed to the ion beam and those protected by the graphite foil. Due to the sputter polishing, the sputter exposed areas are shinier (bottom half on each sample) than the protected areas. The visual inspection does neither show a deterioration by chemical reactions, nor a difference between the samples sputtered with iodine or xenon.

The profilometer measures over a length of 1 – 2 mm across and perpendicular to the boundary between the two areas. The results show the impact of the ion sputtering and reveal differences between xenon and iodine sputtering. Figure 4.22d shows an example of the recorded surface profiles from the sample set of stainless steel 4404. At about 0.6 mm of lateral distance, a clear edge is visible. The graphite foil protected the surface on the left side of the edge, while the right side was subjected to the ion beam. The removed surface material by the sputtering resulted in a height difference of 537 nm for iodine and 525 nm for xenon between these two areas. The height difference is defined as sputter edge, which was measured for all samples. Table 4.6 lists the measured sputter edges as well as the calculated sputter yields (γ) for all samples. Overall, the xenon sputter

Table 4.6: A list of the measured sputter edges of all samples with the respective sputter yields (γ) at an incident ion energy of 1.5 keV and an incident angle of 0°. For a detailed material description see Section 4.3.

Sample	Iodine sputter edge [nm] (γ)	Xenon sputter edge [nm] (γ)
Titanium	715 (1.37)	239 (0.46)
Al-6082	304 (0.60)	1486 (3.11)
Al-7075	275 (0.54)	1314 (2.55)
Al-5754	533 (1.05)	1716 (3.29)
AISI-304	1038 (2.22)	943 (2.20)
AISI-316	1354 (3.94)	1450 (4.29)
4544	471 (2.09)	1367 (6.26)
4546	1004 (2.51)	905 (2.54)
4571	534 (1.53)	1286 (3.82)
4404	537 (1.53)	525 (1.49)
Cyanat[a]	3000 (6.41)	6250 (13.20)
G-Epoxy[b]	2068 (7.07)	2481 (7.48)

[a]Cyanat-Ester RS9, [b]Glassfiber woven epoxy G11

yields are either larger or similar to the iodine sputter yields. The lower sputter yields for iodine can be explained by the molecular nature of iodine. Substantial fractions of the extracted ions are I_2^+-ions, which have twice the mass than an I^+–ion and, therefore, a lower velocity. Titanium is the only material showing a distinctively higher sputter yield for iodine than for xenon. Due to the combination of relatively short exposure times and low iodine partial pressures inside the chamber, the sputter rates are not expected to

be artificially increased by chemical reactions. However, the material deterioration may be enhanced by the high corrosiveness of iodine against titanium, despite the low iodine exposure.

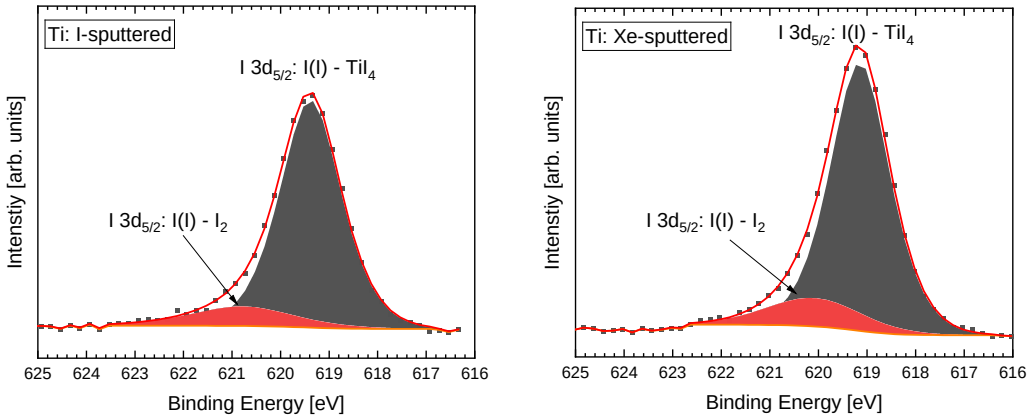

Figure 4.23: Detail XPS spectra of the iodine I3d$_{5/2}$ core level signal after 240 s of Ar^+ etching of the titanium sample sputtered with iodine (a) and xenon (b).

A further assessment of the titanium sample set via XPS measurements revealed similar spectra for the xenon and iodine sputter treatment as shown in Figure 4.23. Both samples show two signals for the I 3d$_{5/2}$ core level. The stronger signal represents iodine bound to another chemical element, such as titanium, forming an iodide. The weaker signal indicates residual molecular iodine. The presence of iodine, especially in the case of xenon sputtering, is not surprising, since both sputter treatments took place in our iodine test facility iPott and residual iodine is always present inside this chamber. However, the iodine content on the surface was very low, below 1 at.% and below 10 at.% (below 3 at.% after 240 s of Ar^+ etching) for the iodine and xenon sputter treatment, respectively. Hence, the sample sputtered with xenon shows a higher iodine content. Nevertheless, the survey spectra contain signals indicating elemental titanium, which increased with Ar^+ etching. This behavior is similar to the behavior seen for the reference samples (untreated) analyzed in Section 4.3, indicating no extensive chemical deterioration by iodine and no artificial increase of the sputter yield. However, it is possible that the iodine ions already removed the majority of reaction products of Ti and I, leaving non for the XPS analysis. Therefore, the data is not fully conclusive. It cannot be decided whether the sputter yield is artificially increased by chemical reactions in the case of titanium. All other samples show no reason to assume chemically enhanced sputtering.

Scanning electron microscope (SEM) images reveal further information about the morphology of the surfaces. Images with a magnification factor of up to 12.000 were recorded of the samples AISI-304, AL-7075 and Ti for both, the samples sputtered with xenon and those sputtered with iodine. The SEM images, shown in Figure 4.24, validate that sputtering does not change the surface morphology. The surfaces exposed to and pro-

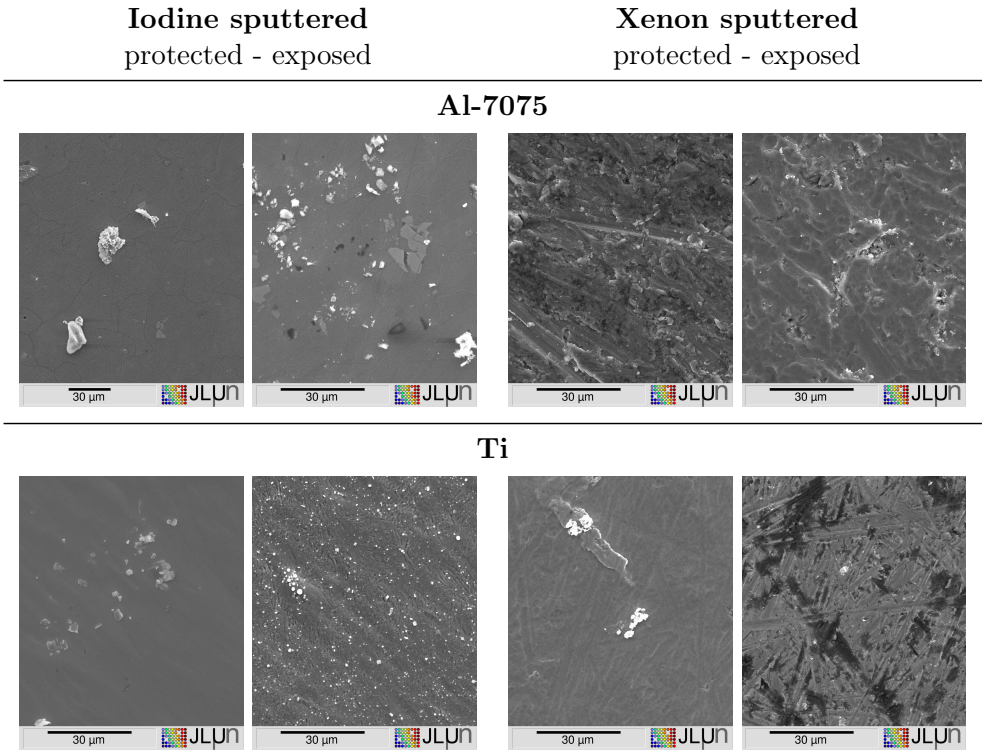

Figure 4.24: SEM surface images of protected and sputtered areas for the samples Al7075 and Ti with a magnification factor of 900.

tected from sputtering show the same basic structures. The Al-7075 sample sputtered with xenon has a rough surface, which is flattened by the sputtering; additionally, some deeper holes developed. The Al-7075 iodine sputtered sample had a flatter surface to begin with. Here, also some deeper holes developed and some edged, bright features appeared. These features are probably a form of iodide. The alterations of the surface agree with the measurements of the sputter edges, where xenon sputtering caused much higher material ablation.

The xenon sputtered titanium sample shows a very rough surface. Some areas seem to have lost more material than others, deep holes and trenches develop. The uneven sputtering can partly explain the low sputter yield, since the tip size of the profilometer is also in the low micrometer range. Consequently, small holes and narrow trenches cannot accurately be measured with the profilometer. This also points towards sputtering without chemical enhancement. On the other hand, the iodine sputtered sample shows a more evenly sputtered surface with many bright spots. These spots, most likely indicating iodine, which is present on all surfaces; however, the surface exposed to iodine sputtering shows by far the most bright spots.

The sample AISI-304 shows no difference in sputter yield between iodine and xenon sputtering. The only visible difference between the SEM images in Figure 4.25 of the

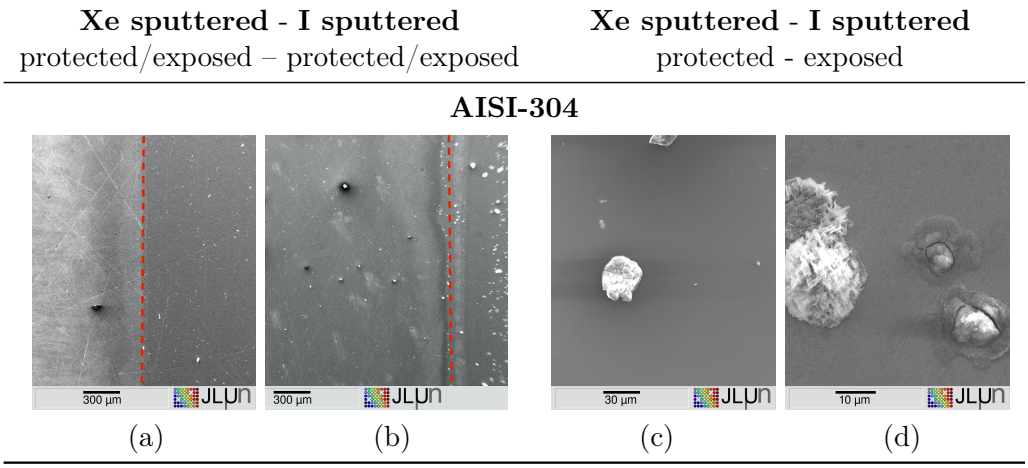

Figure 4.25: AISI-304 samples SEM surface images of the transition area between protected and exposed surface to (a) xenon or (b) iodine sputtering. SEM images with larger magnification of a surface area exposed to (c) xenon and (d) iodine sputtering.

xenon (a) and iodine (b) treated surface is the number of bright spots, showing residual iodine on the surface. Closer views on single bright spots reveal an additional small difference. While the bright spot seems to lie on the surface exposed to xenon sputtering or protected from iodine sputtering (Figure 4.25c), the surface exposed to iodine sputtering shows spots streaked with cracks. It seems that the higher iodine exposure caused reactions of iodine with the surface, extending deeper into the surface. Iron chemically reacts with iodine and oxygen. This is accompanied by a large change in volume [98], which can explain the observed cracks in the surface region. Although physical sputtering is not enhanced in this limited experiment, chemical reactivity is present as seen on the example of AISI-304. With higher iodine background pressures, sputtering can be increased by chemical reaction and must be considered.

In summary, physical xenon and iodine sputtering is equally damaging; therefore, the experiences from xenon sputtering can be transferred to iodine sputtering. However, a combination between an iodine residual atmosphere and iodine sputtering may be much more damaging than in a comparable setup with xenon. The iodine atmosphere may react with the material's surface, while the energetic ions may then easily remove the soft, newly formed iodide. Additionally, the energetic ions may remove the initial protective oxide layer and expose the pure elements to the iodine atmosphere. Consequently, much higher, artificial sputter rates may result, especially, if the structural material is highly reactive in contact with iodine.

4.4.4 Damaging effect of iodine plasma

The previous sections described the effects of iodine sputtering and iodine atmospheric treatment on various materials. While atmospheric contact can be devastating for certain materials such as Al, Fe, or Ti, iodine sputtering turned out to possess a comparable damaging potential as xenon sputtering. The physical sputtering dominates over chemical reactions. In an iodine plasma, these two conditions, chemical deterioration and physical sputtering, can occur simultaneously and, therefore, possibly amplify the material damaging effect of iodine. The damaging effect strongly depends on the plasma condition with the expected highest corrosion conditions to occur in a dense iodine plasma with high energetic ions. Additionally, the iodine plasma might generally be more reactive than a pure I_2 atmosphere due to the presence of more than just one particle species, i.e., ions (positive and negative), neutral atoms, charged molecules, and neutral molecules.

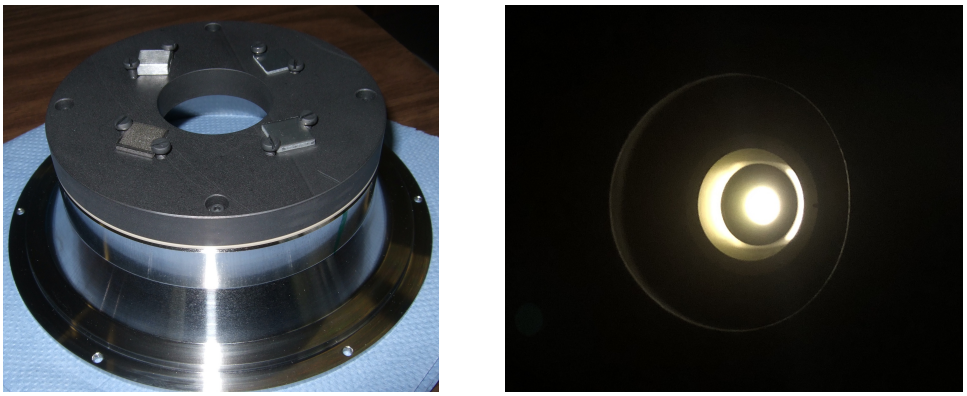

(a) (b)

Figure 4.26: (a) The sample holder used for the plasma treatments instead of the RIT's grid system. (b) Operation of the modified thruster during the plasma treatment.

In this experiment, the iodine plasma treatment of the samples is achieved inside a RIM-10 because the plasma conditions are well quantified due to the work of Dietz et al. [81, 119], which is necessary to compare the damaging effect of the iodine plasma with the two damaging conditions: sputtering and atmospheric treatment. The treatment of the samples with an iodine plasma was achieved by replacing the grid system of the RIM-10 with a graphite sample holder (shown in Figure 4.26a) with a central aperture. The samples are mounted on the inner surface and, therefore, they are directly exposed to the plasma at a floating potential. Figure 4.26b shows the setup from the outside in operation. The transmissivities of the grid system and the aperture of the sample holder are equal for neutral gas particles; hence, the plasma conditions in terms of partial pressures and electron density are comparable in both cases. The plasma parameters of the iodine plasma are calculated using a theoretical model for the RIM-10 and are given in Table 4.7. The dominant particle species inside the plasma are neutral iodine atoms (nI)

and molecules (nI2). The partial pressure of the neutral iodine particles can roughly be

Table 4.7: Iodine plasma conditions in the RIM-10 during the plasma treatment based on the work of Dietz at al. [81, 119].

Property	Variable	Unit	Value
Electron density	n	[m^{-3}]	$9.9{\cdot}10^{16}$
I^- - density	nIm	[m^{-3}]	$2.8{\cdot}10^{16}$
I_2 – density	$nI2$	[m^{-3}]	$8.2{\cdot}10^{18}$
I – density	nI	[m^{-3}]	$2.5{\cdot}10^{19}$
I^+ - density	nIp	[m^{-3}]	$7.2{\cdot}10^{16}$
I_2^+ - density	$nI2p$	[m^{-3}]	$5.5{\cdot}10^{16}$
Electron temperature	T_e	[eV]	$3.5{\cdot}10^{4}$
Neutral gas temperature	T_g	[K]	405

estimated employing the equation for an ideal gas and using the values given in Table 4.7.

$$p \cdot V = N \cdot k_B \cdot T \tag{4.10}$$

A partial pressure of 0.182 Pa ($1.8{\cdot}10^{-6}$ mbar) is derived assuming the values $V = 1m^3$, $N = 3.3 \cdot 10^{19}$ (nI + nI2), $k_B = 1.38 \cdot 10^{-23}$ J/K, $T = 400\,K$. The low partial pressure, the high temperature (400 K), and the long exposure time of 6 h lead to $3.25{\cdot}10^{25}$ iodine particle collisions per m^2 (see Section 4.3) with the sample's surfaces. The total number of collisions is about one order of magnitude lower than the lowest calculated value in Section 4.3 for scenario 1. Consequently, a sample deterioration caused by chemical reactions is expected to be low and the effects of the plasma can be analyzed.

In summary, the samples Ti, AISI-304, AISI-316, Al-6082, Al-7075, Al-5754, and G-Epoxy were treated for 6 hours in the iodine plasma, fueled by 0.37 milligrams per second of iodine mass flow. The radio-frequency generator (RFG) couples about 45 W of rf-power into the plasma, while the sample holder and samples were electrically in a floating condition (insulated towards ground potential).

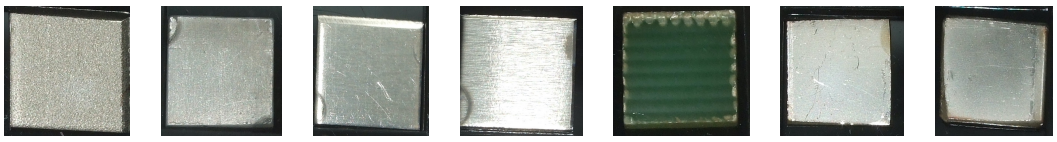

Ti Al-5754 Al-6082 Al-7075 G-Epoxy AISI-304 AISI-316

Figure 4.27: Images of the samples subsequent to their iodine plasma treatment, without visible discoloring.

Subsequent to the plasma treatment, the samples were analyzed via optical inspection and XPS. As shown in Figure 4.27, none of the samples showed a distinct surface color change. Only the edges of some samples are slight discolored, where the sample holder

was connected to the samples. The first observation agrees with the expectation that the low pressures do not cause significant damage due to chemical reactions. Thus, the plasma is not orders of magnitude more reactive than the neutral gas.

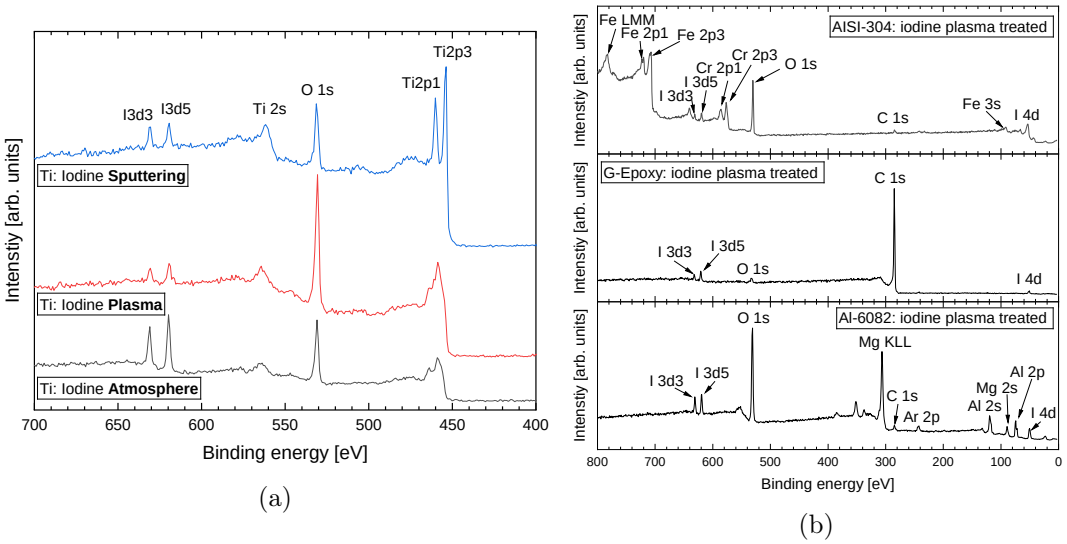

Figure 4.28: XPS survey spectra after 240 s of Ar^+ etching of (a) three differently treated titanium samples (treatment conditions: plasma, sputtering according to Section 4.4.3, and atmospheric according to Scenario 4 in Section 4.3) and (b) plasma treated AISI-304, G-Epoxy, and Al-6082.

Titanium showed to be highly reactive with iodine; therefore, even small effects of the iodine treatment should be detectable. Figure 4.28a shows XPS survey spectra of titanium samples treated according to the three different treatment conditions discussed. All three spectra show the distinct signals for Ti, O, and I, where the detail spectra of the iodine core level signal I $3d_{5/2}$ showed all iodine to be part of an iodide. The shown survey spectra differ in respective signal intensity (respective: signal intensities always in comparison among other signals of the same spectrum). The atmospherically treated sample shows the strongest signal of iodine in comparison to its respective Ti $2p_{3/2}$ signal, while in the other two spectra, the titanium signal dominates over the iodine signal. On the other hand, the oxygen signal is the lowest for the sputtered sample, indicating the removal of the protective passivation layer formed under air. The relatively strong oxygen signal measured at the plasma treated sample indicates a still existing titanium oxide layer, while the iodine signal is very weak. In comparison, the iodine signal is stronger and the oxygen signal strength is reduced at the sample treated in a pure iodine atmosphere, which can be caused by a deterioration of the passivation layer. Thus, physical sputtering is not the primary interaction mechanism for a sample in contact with the plasma since the samples are electrically insulated towards ground and float with the plasma potential. Consequently, no highly energetic ions hit the samples during

the plasma treatment and the energetic sputtering does not occur. Overall, the plasma treated titanium sample shows a similar XPS spectrum than the sample treated in an iodine atmosphere. The stronger iodine and weaker oxygen signal can be caused by the different particle densities of the treatment conditions. The low neutral gas pressure of the plasma causes orders of magnitudes less collisions of gas particles with the surface than accumulated during the Scenario 4 atmospheric treatment. Thus less iodine interacted with the sample's surface, which explains the difference in signal intensities. Therefore, the dominant sample deterioration mechanism is due to chemical reactions.

The XPS survey spectra of AISI-304 and Al-6082 are shown in Figure 4.28b. Both spectra show strong oxygen signals and weak iodine signals, which strengthens the conclusion drawn from the analysis of the results of the titanium sample. The plasma interacts via random atmospheric collisions with the surfaces without energetic sputtering. The detail spectrum of the iodine peak also shows only iodine in form of an iodide. In contrast, the analysis of the G-Epoxy sample reveals two signals for the core level I $5d_{5/2}$. One representing an iodide and the other molecular iodine. Nevertheless, the iodine content was below 1 at.% after the Ar^+ etching, indicating no iodine penetration in the depth of the sample. In summary, there is no indication that iodine plasma is much more reactive than an iodine atmosphere as long as no high-energy sputtering occurs.

Generally, the damaging effect of an iodine plasma strongly depends on the plasma conditions. As shown above, iodine plasma conditions are not necessarily more hazardous than neutral atmospheric iodine conditions, though they may be. The degree of damage mainly depends on the plasma density (magnitude of chemical reactions) and the contact between sample and plasma (magnitude of sputtering). A dense, highly energetic plasma (combination of sputtering and chemical reactions) erodes most materials very quickly, which has to be avoided in all designs. Plasma conditions typical for the inside of ion thrusters, as shown, seem not to be more dangerous than iodine atmospheric treatment for the tested materials.

5 Conclusion

Replacing the common propellant xenon by iodine in electric propulsion systems used on satellites launched to space is technologically feasible despite the chemical reactivity of iodine. The cost savings achievable with iodine as alternative propellant are enormous. Conventional thruster concepts already run on iodine for hundreds and thousands of hours in ground facilities cultivating heritage to safely conduct long life satellite missions. As identified In the introduction, the unknown lifetime corrosion effects of iodine and the missing iodine compatible neutralizer technology are the two main issues holding back fully iodine-fueled propulsion systems (illustrated in Figure 1.1). The aspect of iodine material corrosion is always a concern and difficult to investigate in fully integrated thrusters due to a regular contact with the ambient atmosphere and the difficulty of extracting samples for further analysis. Additionally, a missing piece to operate a fully iodine-fueled electric propulsion system is the development of an iodine compatible cathode. Common insert materials of hollow cathode seem to be incompatible with iodine. Thus, alternatives must be developed.

In this work, a hollow cathode was developed that operates with the new insert material C12A7:2e$^-$, which seems to be iodine compatible. The main issue of insert melting and degradation due to high temperature effects were mitigated and the cathode operated for tens of hours with xenon. This shows that with a good thermal design and a carefully configurated hollow cathode, the operation of a C12A7:2e$^-$ insert is possible. In the future, the issue of insert sputtering must be reduced by additional iteration steps of the design presented in this thesis, including an optimized thermal design and plasma configuration to enable hundreds of hours of insert operation. Additionally, the C12A7:2e$^-$ based hollow cathode must give definite proof that it operates with iodine for hundreds of hours.

In the second part of this work, the corrosion effects of iodine on metal parts in relation to the space environment were closely investigated. The results identify critical elements in contact with iodine and show the importance of working in a water and oxygen free environment to accurately predict the effects of iodine in space. A blueprint is detailed to estimate the effects of iodine corrosion even over long satellite mission scenarios. It shows how to properly simulate iodine effects on satellites in a laboratory environment. The results help to identify critical components on a satellite in terms of iodine corrosion and increase the understanding of the impact of a local iodine atmosphere developing around a satellite during long thrust maneuvers with an iodine-fueled propulsion system.

Overall, a first step towards a fully iodine-fueled electric propulsion system is given by showing the development of a hollow cathode with the alternative insert material C12A7:2e$^-$. Furthermore, the close investigation of iodine corrosion on a wide range of

materials are important for the development of satellites equipped with iodine fueled electric propulsion systems operating for years in space. Thus, this work provides substantial research to fill the shown research gaps and to enable a fully iodine-fueled propulsion system operating on a satellite in space.

Bibliography

[1] Daniel A. Herman et al. "Development and Qualification Status of the Electric Propulsion Systems for the NASA PPE Mission and Gateway Program." In: IEPC2022. Boston, June 2022. DOI: IEPC-2022-465.

[2] K. Holste et al. "Ion thrusters for electric propulsion: Scientific issues developing a niche technology into a game changer." In: *Review of Scientific Instruments* 91.6 (June 1, 2020), p. 061101. ISSN: 0034-6748, 1089-7623. DOI: 10.1063/5.0010134.

[3] Safran Aircraft Engines. *Safran PPS5000 plasma thruster chosen for new Galileo satellites*. Press release. Jan. 26, 2022.

[4] *Busek scales thruster production for Airbus OneWeb Satellites*. Busek scales thruster production for Airbus OneWeb Satellites. June 23, 2022. URL: https://www.militaryaerospace.com/communications/article/14278616/busek-scales-thruster-production-for-airbus-oneweb-satellites.

[5] Wikipedia. *Starlink*. 2022. URL: https://en.wikipedia.org/wiki/Starlink#cite_note-sn2674441-5 (visited on 10/27/2022).

[6] Dan M. Goebel and Ira Katz. *Fundamentals of electric propulsion: ion and Hall thrusters*. JPL space science and technology series 1. OCLC: ocn233939832. Hoboken, N.J: Wiley, 2008. 507 pp. ISBN: 978-0-470-42927-3.

[7] Harold R. Kaufman. "Technology of Electron-Bombardment Ion Thrusters." In: *Advances in Electronics and Electron Physics*. Vol. 36. Elsevier, 1975, pp. 265–373. ISBN: 978-0-12-014536-2. DOI: 10.1016/S0065-2539(08)61121-X.

[8] Dan R Lev. "Recent progress in research and development of hollow cathodes for electric propulsion." In: *Reviews of Modern Plasma Physics* (2019), p. 89. DOI: https://doi.org/10.1007/s41614-019-0026-0.

[9] Dan M Goebel, Ron M Watkins, and Kristina K Jameson. "LaB6 Hollow Cathodes for Ion and Hall Thrusters." In: *Journal of Propulsion and Power* (2007), p. 7. DOI: 10.2514/1.25475.

[10] G-C Potrivitu, L Xu, and S Xu. "A low-current LaB6 open-end knife-edge emitter hollow cathode for low-power Hall thrusters." In: *Plasma Sources Science and Technology* 30.8 (Aug. 1, 2021), p. 085012. ISSN: 0963-0252, 1361-6595. DOI: 10.1088/1361-6595/ac1b34.

[11] Olivier Duchemin et al. "Qualification Status of the PPS®5000 Hall Thruster Unit." In: IEPC2019. Vienna, Sept. 2019. DOI: IEPC-2019-906.

[12] Sarah W. Shark et al. "High Power Demonstration of a 100 kW Nested Hall Thruster System." In: *AIAA Propulsion and Energy 2019 Forum*. AIAA Propulsion and Energy 2019 Forum. Indianapolis, IN: American Institute of Aeronautics and Astronautics, Aug. 19, 2019. ISBN: 978-1-62410-590-6. DOI: 10.2514/6.2019-3809.

[13] Dan M. Goebel et al. "Plasma hollow cathodes." In: *Journal of Applied Physics* 130.5 (Aug. 7, 2021), p. 050902. ISSN: 0021-8979, 1089-7550. DOI: 10.1063/5.0051228.

[14] Dan Lev et al. "The technological and commercial expansion of electric propulsion." In: *Acta Astronautica* 159 (June 2019), pp. 213–227. ISSN: 00945765. DOI: 10.1016/j.actaastro.2019.03.058.

[15] Sindelhauser Materials. *LaB6 Properties*. LaB6 Properties. Sept. 11, 2022. URL: https://www.sindlhauser.de/en/lab6-keramik-und-kathoden.html.

[16] H E Gallagher. "Poisoning of LaB6 Cathodes." In: *Journal of Applied Physics* 40 (1968), p. 44.

[17] J.L. Cronin. "Practical Aspects of Modern Dispenser Cathodes." In: *Microwave Journal* 22 (Sept. 1979), pp. 57–62.

[18] David Torréns-Martín et al. "Raman Spectroscopy of Anhydrous and Hydrated Calcium Aluminates and Sulfoaluminates." In: *Journal of the American Ceramic Society* 96.11 (2013), p. 7. DOI: 10.1111/jace.12535.

[19] Satoru Matsuishi et al. "High-Density Electron Anions in a Nanoporous Single Crystal: [Ca24Al28O64]4+(4e-)." In: 301 (2003), p. 5.

[20] Yoshitake Toda et al. "Field Emission of Electron Anions Clathrated in Subnanometer-Sized Cages in [Ca24Al28O64]4+(4e-)." In: *Adv. Mater.* 8 (2004), p. 5.

[21] Christian Drobny, Florian Nürmberger, and Martin Tajmar. "Development of a compact Hall thruster with a C12A7 low-power hollow cathode." In: (2016), p. 9.

[22] Malina Reitemeyer et al. "Applicability of electride materials for hollow cathodes." In: IEPC-2019. 2019.

[23] Yoshitake Toda et al. "Work Function of a Room-Temperature, Stable Electride [Ca24Al28O64]4+(e-)4." In: *Adv. Mater.* (2007), p. 6. DOI: 10.1002/adma.200700663.

[24] A Heiler et al. "Work function performance of a C12A7 electride surface exposed to low pressure low temperature hydrogen plasmas." In: *Journal of Vacuum Science and Technology* (Dec. 29, 2020), p. 8. DOI: https://doi.org/10.1116/6.0000749.

[25] Natalie R.S. Caruso and Michael S. McDonald. "Thermionic Emission Measurements of 12(CaO)-7(Al2O3) Electride in a Close-Spaced Diode." In: IEPC-2017. 2017.

[26] Sung Wng Kim et al. "Synthesis of a Room Temperature Stable 12CaO 7Al2O3 Electride from the Melt and Its Application as an Electron Field Emitter." In: *Chem. Mater.* (2006), p. 7.

[27] Nils Gerrit Kottke et al. “Comparison of the thermionic emission properties of LaB6 and C12A7.” In: IEPC-2019. 2019.

[28] Phuong-Vu Ong, Hideo Hosono, and Peter V Sushko. “Structure and Electronic Properties of [Ca24Al28O64]4+(4e–) Surfaces: Opportunities for Termination-Controlled Electron Transfer.” In: *J. Phys. Chem. C* (2019), p. 7.

[29] Sung-Wng Kim et al. “Fabrication of room temperature-stable 12CaO 7Al2O3 electride: a review.” In: *J Mater Sci* (2007), p. 10. DOI: 10.1007/s10854-007-9183-y.

[30] Toshihiro Yoshizumi and Katsuro Hayashi. “Thermionic Electron Emission from a Mayenite Electride–Metallic Titanium Composite Cathode.” In: *Appl. Phys. Express* (2013), p. 4. DOI: http://dx.doi.org/10.7567/APEX.6.015802.

[31] Xin Zhang et al. “Sr-doping enhanced electrical transport and thermionic emission of single crystal 12CaO 7Al2O3 electride.” In: *Current Applied Physics* 20 (2020), pp. 96–101. DOI: https://doi.org/10.1016/j.cap.2019.10.008.

[32] Sung Wng Kim et al. “Thermal conductivity and Seebeck coefficient of 12CaO 7Al2O3 electride with a cage structure.” In: *PHYSICAL REVIEW B* (2009), p. 6. DOI: 10.1103/PhysRevB.80.075201.

[33] Sung Wng Kim, Terumasa Shimoyama, and Hideo Hosono. “Solvated Electrons in High-Temperature Melts and Glasses of the Room-Temperature Stable Electride [Ca24Al28O64]4+(4e)-.” In: 333 (2011), p. 5. DOI: 10.1126/science.1204394.

[34] Luis Palacios et al. “Crystal Structures and in-Situ Formation Study of Mayenite Electrides.” In: *Inorganic Chemistry* 46.10 (May 1, 2007), pp. 4167–4176. ISSN: 0020-1669, 1520-510X. DOI: 10.1021/ic0700497.

[35] Lauren Rand, John Williams, and Robert Hoyt. “Hollow Cathode with Electride Insert.” In: *47th AIAA/ASME/SAE/ASEE Joint Propulsion Conference & Exhibit*. 47th AIAA/ASME/SAE/ASEE Joint Propulsion Conference & Exhibit. San Diego, California: American Institute of Aeronautics and Astronautics, July 31, 2011. ISBN: 978-1-60086-949-5. DOI: 10.2514/6.2011-5992.

[36] Lauren Paula Rand et al. *C12A7 Electride Hollow Cathode*. 2013, p. 8.

[37] Lauren P. Rand and John D. Williams. “A Calcium Aluminate Electride Hollow Cathode.” In: *IEEE Transactions on Plasma Science* 43.1 (Jan. 2015), pp. 190–194. ISSN: 0093-3813, 1939-9375. DOI: 10.1109/TPS.2014.2338737.

[38] Christian Drobny and Martin Tajmar. “Development of a C12A7 Electride Hollow Cathode.” In: IEPC-2017. Oct. 2017.

[39] Christian Drobny, Jan-Philipp Wulfkühler, and Martin Tajmar. “Development of a C12A7 Electride Hollow Cathode and Joint Operation with a Plasma Thruster.” In: IEPC-2019. 2019.

[40] Michael S. McDonald and Natalie R.S. Caruso. “Ignition and Early Operating Characteristics of a Low- Current C12A7 Hollow Cathode.” In: IEPC-2017. 2017.

[41] Zhiwei Hua et al. "Experimental characterization of the C12A7 hollow cathode and its joint operation with a low-power Hall thruster." In: *Vacuum* 192 (Oct. 2021), p. 110443. ISSN: 0042207X. DOI: 10.1016/j.vacuum.2021.110443.

[42] Kristof Holste et al. "Performance of an iodine-fueled radio-frequency ion-thruster." In: *The European Physical Journal D* 72.1 (Jan. 2018), p. 9. ISSN: 1434-6060, 1434-6079. DOI: 10.1140/epjd/e2017-80498-5.

[43] John Dankanich et al. "Mission and System Advantages of Iodine Hall Thrusters." In: 50th AIAA/ASME/SAE/ASEE Joint Propulsion Conference. Cleveland, OH: American Institute of Aeronautics and Astronautics, July 28, 2014. ISBN: 978-1-62410-303-2. DOI: 10.2514/6.2014-3905.

[44] Dmytro Rafalskyi et al. "In-orbit demonstration of an iodine electric propulsion system." In: *Nature* 599.7885 (Nov. 18, 2021), pp. 411–415. ISSN: 0028-0836, 1476-4687. DOI: 10.1038/s41586-021-04015-y.

[45] Richard Branam. *Iodine Plasma (Electric Propulsion) Interaction with Spacecraft Materials*. Final Report AFRL-AFOSR-VA-TR-2016-0381. Dec. 28, 2016.

[46] Daniel Zschätzsch et al. "Corrosion of metal parts on satellites by iodine exposure in space." In: *Journal of Electric Propulsion* 1.1 (Sept. 28, 2022), p. 14. ISSN: 2731-4596. DOI: 10.1007/s44205-022-00014-x.

[47] John Dankanich et al. "The Iodine Satellite (iSat) Project Development through Critical Design Review (CDR)." In: 52nd AIAA/SAE/ASEE Joint Propulsion Conference. Salt Lake City, UT: American Institute of Aeronautics and Astronautics, July 25, 2016. ISBN: 978-1-62410-406-0. DOI: 10.2514/6.2016-4540.

[48] Zachary R. Taillefer, John J. Blandino, and James Szabo. "Characterization of a Barium Oxide Cathode Operating on Xenon and Iodine Propellants." In: *Journal of Propulsion and Power* 36.4 (July 2020), pp. 575–585. ISSN: 1533-3876. DOI: 10.2514/1.B37315.

[49] A. Post et al. "Key design and operation factors for high performance of C12A7:e-based cathodes." In: *IOP Conference Series: Materials Science and Engineering* 1226.1 (Feb. 1, 2022), p. 012092. ISSN: 1757-8981, 1757-899X. DOI: 10.1088/1757-899X/1226/1/012092.

[50] Zhiwei Hua et al. "Early experimental investigation of the C12A7 hollow cathode fed on iodine." In: *Plasma Science and Technology* 24.7 (July 1, 2022), p. 074004. ISSN: 1009-0630. DOI: 10.1088/2058-6272/ac4fb4.

[51] Gabriel F Benavides et al. "Iodine Hall-Effect Electric Propulsion System Research, Development, and System Durability Demonstration." In: Joint Propulsion Conference. 2018, p. 32. DOI: 10.2514/6.2018-4422.

[52] Gustavo Costa et al. *Corrosion Behavior of Stainless Steel 304 and Nickel 625 Under Iodine Vapor at 300 °C*. Technical Report NASA/TM—2020-5001422. NASA, 2020, p. 21.

[53] J. Martínez Martínez and D. Rafalskyi. "Design and development of iodine flow control systems for miniaturized propulsion systems." In: *CEAS Space Journal* (Aug. 1, 2021). ISSN: 1868-2502, 1868-2510. DOI: 10.1007/s12567-021-00384-2.

[54] James Szabo et al. "Iodine Propellant Space Propulsion." In: IEPC-2013. Oct. 2013. DOI: IEPCPaper2013-311.

[55] John R. Brophy. "NASA's Deep Space 1 ion engine (plenary)." In: *Review of Scientific Instruments* 73.2 (Feb. 2002), pp. 1071–1078. ISSN: 0034-6748, 1089-7623. DOI: 10.1063/1.1432470.

[56] JPL. *JPL Image Use Policy*. JPL Image Use Policy. Jan. 26, 2023. URL: https://www.jpl.nasa.gov/jpl-image-use-policy (visited on 01/26/2023).

[57] NASA. *NASA: Media Usage Guidelines*. NASA: Media Usage Guidelines. Jan. 26, 2023. URL: https://www.nasa.gov/multimedia/guidelines/index.html (visited on 01/26/2023).

[58] R. Deltschew et al. "Sputter yield measurements of graphite and carbon-carbon material for ion thruster grids." In: *37th Joint Propulsion Conference and Exhibit*. 37th Joint Propulsion Conference and Exhibit. Salt Lake City,UT,U.S.A.: American Institute of Aeronautics and Astronautics, July 8, 2001. DOI: 10.2514/6.2001-3493.

[59] Yasushi Ohkawa et al. "Current Statuses of Graphite Hollow Cathode Life Tests." In: *46th AIAA/ASME/SAE/ASEE Joint Propulsion Conference & Exhibit*. 46th AIAA/ASME/SAE/ASEE Joint Propulsion Conference & Exhibit. Nashville, TN: American Institute of Aeronautics and Astronautics, July 25, 2010. ISBN: 978-1-60086-958-7. DOI: 10.2514/6.2010-6945.

[60] Andreas Küchler. *Hochspannungstechnik: Grundlagen - Technologie - Anwendungen*. Berlin, Heidelberg: Springer Berlin Heidelberg, 2009. ISBN: 978-3-540-78412-8 978-3-540-78413-5. DOI: 10.1007/978-3-540-78413-5. (Visited on 11/09/2022).

[61] Vincent K Rawlin and William R Kerslake. "SERT II - Durability of the hollow cathode and future applications of hollow cathodes." In: (1970), p. 7.

[62] Pierre-Yves C. Taunay, Christopher J. Wordingham, and Edgar Choueiri. "An empirical scaling relationship for the total pressure in hollow cathodes." In: *2018 Joint Propulsion Conference*. 2018 Joint Propulsion Conference. Cincinnati, Ohio: American Institute of Aeronautics and Astronautics, July 9, 2018. ISBN: 978-1-62410-570-8. DOI: 10.2514/6.2018-4428.

[63] L. Rehn and H. Kaufman. "Correlation of inert gas hollow cathode performance." In: *13th International Electric Propulsion Conference*. 13th International Electric Propulsion Conference. San Diego,CA,U.S.A.: American Institute of Aeronautics and Astronautics, Apr. 25, 1978. DOI: 10.2514/6.1978-707.

[64] Matthew T Domonkos, Alec D Gallimore, and Michael J Patterson. "An Evaluation of Hollow Cathode Scaling to Very Low Power and Flow Rate." In: (1997), p. 7.

[65] Ira Katz et al. "Plasma Heating of Inert Gas Hollow Cathode Inserts." In: IEPC-2007. 2007.

[66] Wayne B. Nottingham. *Thermionic Emission*. 1956.

[67] Conyers Herring and M H Nichols. "Thermionic Emission." In: (1949), p. 87.

[68] Frederick Measham Lea and Peter C. Hewlett. *Lea's chemistry of cement and concrete*. 4th edition. Amsterdam London Paris: Elsevier-Butterworth-Heinemann, 2004. ISBN: 978-0-7506-6256-7.

[69] Satoru Matsuishi et al. "Localized and Delocalized Electrons in Room-Temperature Stable Electride [Ca24Al28O64]4+(O2-)2-x(e-)2x: Analysis of Optical Reflectance Spectra." In: *J. Phys. Chem. C* (2008), p. 8.

[70] Sung Wng Kim and Hideo Hosono. "Synthesis and properties of 12CaO · 7Al $_2$ O $_3$ electride: review of single crystal and thin film growth." In: *Philosophical Magazine* 92.19 (July 2012), pp. 2596–2628. ISSN: 1478-6435, 1478-6443. DOI: 10.1080/14786435.2012.685770.

[71] Karim Khan et al. "A comprehensive review on synthesis of pristine and doped inorganic room temperature stable mayenite electride, [Ca24Al28O64]4+(e-)4 and its applications as a catalyst." In: *Progress in Solid State Chemistry* (Dec. 2018), p. 20.

[72] Toshihiro Yoshizumi et al. "Iodometric Determination of Electrons Incorporated into Cages in 12CaO · 7Al2O3 Crystals." In: *J. Phys. Chem. C* (2010), p. 4.

[73] NIST. *NIST WebBook: Iodine*. NIST WebBook Iodine. URL: https://webbook.nist.gov/cgi/cbook.cgi?ID=7553-56-2.

[74] Daniel R. Stull. "Vapor Pressure of Pure Substances. Organic and Inorganic Compounds." In: *Industrial & Engineering Chemistry* 39.4 (Apr. 1947), pp. 517–540. ISSN: 0019-7866, 1541-5724. DOI: 10.1021/ie50448a022.

[75] M. Ruszak et al. "THE ROLE OF INTERMEDIATE CALCIUM ALUMINATE PHASES IN SOLID STATE SYNTHESIS OF MAYENITE (Ca12Al14O33)." In: *Functional Materials Letters* 04.2 (June 2011), pp. 183–186. ISSN: 1793-6047, 1793-7213. DOI: 10.1142/S1793604711001907.

[76] Wenwei Zou et al. "Direct fabrication of C12A7 electride target and room temperature deposition of thin films with low work function." In: (2017), p. 8.

[77] Alexander V Naumkin et al. *X-ray Photoelectron Spectroscopy Database XPS,Version 4.1, NIST Standard Reference Database 20*. Type: dataset. 1989. DOI: 10.18434/T4T88K. URL: http://srdata.nist.gov/xps/.

[78] G Greczynski. "X-ray photoelectron spectroscopy_ Towards reliable binding energy referencing." In: *Progress in Materials Science* (2020), p. 46.

[79] Sarah Fearn. *An Introduction to Time-of-Flight Secondary Ion Mass Spectrometry (ToF-SIMS) and its Application to Materials Science*. IOP Publishing, 2015. ISBN: 978-1-68174-088-1. DOI: 10.1088/978-1-6817-4088-1.

[80] John C Vickerman. "ToF-SIMS—An Overview." In: (2001).

[81] Patrick Dietz et al. "Molecular propellants for ion thrusters." In: *Plasma Sources Science and Technology* 28.8 (Aug. 1, 2019), p. 084001. ISSN: 0963-0252, 1361-6595. DOI: 10.1088/1361-6595/ab2c6c.

[82] Andrew H. Simon. "Sputter Processing." In: *Handbook of Thin Film Deposition*. Elsevier, 2012, pp. 55–88. ISBN: 978-1-4377-7873-1. DOI: 10.1016/B978-1-4377-7873-1.00004-8.

[83] John G. Webster, ed. *The measurement, instrumentation, and sensors handbook*. The electrical engineering handbook series. Boca Raton, Fla: CRC Press published in cooperation with IEEE Press, 1999. 1 p. ISBN: 978-0-8493-8347-2.

[84] J R Salasin et al. "Direct Formation and Structural Characterization of Electride C12A7." In: (2019), p. 22.

[85] Wolfgang Demtröder. *Experimentalphysik 2*. Springer-Lehrbuch. Berlin, Heidelberg: Springer Berlin Heidelberg, 2017. ISBN: 978-3-662-55789-1 978-3-662-55790-7. DOI: 10.1007/978-3-662-55790-7.

[86] Daniel Zschätzsch and Peter J. Klar. "Iodine Materials Interaction Database." In: (Dec. 15, 2021). DOI: http://dx.doi.org/10.22029/jlupub-441.

[87] Michael Nakles et al. "A Performance and Plume Comparison of Xenon and Krypton Propellant on the SPT-100." In: *48th AIAA/ASME/SAE/ASEE Joint Propulsion Conference & Exhibit*. 48th AIAA/ASME/SAE/ASEE Joint Propulsion Conference & Exhibit. Atlanta, Georgia: American Institute of Aeronautics and Astronautics, July 30, 2012. ISBN: 978-1-60086-935-8. DOI: 10.2514/6.2012-4116.

[88] Daniela Pedrini et al. "Development of Hollow Cathodes for Space Electric Propulsion at Sitael." In: *Aerospace* 4.2 (May 6, 2017), p. 26. ISSN: 2226-4310. DOI: 10.3390/aerospace4020026.

[89] James Szabo et al. "Measurements of a Krypton Fed 1.5 kW Hall Effect Thruster with a Centrally Located Cathode." In: *IEPC-2017-26*. 35th International Electric Propulsion Conference 2017. 2017.

[90] Dillon O'Reilly, Georg Herdrich, and Darren F. Kavanagh. "Electric Propulsion Methods for Small Satellites: A Review." In: *Aerospace* 8.1 (Jan. 18, 2021), p. 22. ISSN: 2226-4310. DOI: 10.3390/aerospace8010022.

[91] Manuel La Rosa Betancourt et al. "Comparative Overview of Nuclear Electric Propulsion Programs and Concepts." In: 72st International Astronautical Congress (IAC). Oct. 2021. DOI: IAC-21,C3,5-C4.10,2,x64835.

[92] Marco Manente et al. "REGULUS: Iodine Fed Plasma Propulsion System for Small Satellites." In: IEPC-2019. Sept. 2019.

[93] P.S Sidky. "Iodine stress corrosion cracking of Zircaloy reactor cladding: iodine chemistry (a review)." In: *Journal of Nuclear Materials* 256.1 (July 1998), pp. 1–17. ISSN: 00223115. DOI: 10.1016/S0022-3115(98)00044-0.

[94] Takeshi Fukuda and Shunzo Omori. *Corrosion of AISI 316 and AISI 304 stainless steel with iodine vapor*. ORNL-tr–4694, JAERI-M–5946, 7039340. Dec. 1, 1974. DOI: 10.2172/7039340.

[95] J. A. Beavers, W. E. Berry, and J. C. Griess. *Materials performance in off-gas systems containing iodine*. ORNL/Sub-7327/11, 6040920. Nov. 1, 1981, ORNL/Sub–7327/11, 6040920. DOI: 10.2172/6040920.

[96] J. Amend et al. "1000 h-Langzeituntersuchungen zur Iod-Korrosion an ausgewählten Edelstahlproben unter simulierten Auflöserbedingungen." In: *Kernforschungszentrum Karlsruhe* (1985).

[97] F Funke et al. "Iodine-steel reactions under severe accident conditions in light-water reactors." In: *Nuclear Engineering and Design* 166 (1996), pp. 357 –365. DOI: 10.1016/S0029-5493(96)01253-8.

[98] J C Wren, G A Glowa, and J Merritt. "Corrosion of stainless steel by gaseous 12." In: *Journal of Nuclear Materials* 265 (1999), pp. 161–177.

[99] Wilfried Ley, Klaus Wittmann, and Willi Hallmann. *Handbuch der Raumfahrttechnik*. 5., aktualisierte und erweiterte Auflage. München: Hanser, 2019. 934 pp. ISBN: 978-3-446-45429-3.

[100] Dmitry Levko and Laxminarayan L. Raja. "Fluid modeling of inductively coupled iodine plasma for electric propulsion conditions." In: *Journal of Applied Physics* 130.17 (Nov. 7, 2021), p. 173302. ISSN: 0021-8979, 1089-7550. DOI: 10.1063/5.0063578.

[101] Patrick Dietz et al. "Performance of a rf neutralizer operating with noble gases and iodine." In: *The European Physical Journal Applied Physics* 91.1 (July 2020), p. 10901. ISSN: 1286-0042, 1286-0050. DOI: 10.1051/epjap/2020190213.

[102] P. W Atkins and Julio De Paula. *Atkins' Physical chemistry*. OCLC: 66528976. New York: W.H. Freeman, 2006. ISBN: 978-0-7167-8759-4.

[103] O. Kubaschewski et al. *Materials thermochemistry*. 6th ed., rev. and enl. Oxford ; New York: Pergamon Press, 1993. 363 pp. ISBN: 978-0-08-041888-9.

[104] M. W. Chase and National Institute of Standards {and} Technology (U.S.), eds. *NIST-JANAF thermochemical tables*. 4th ed. Washington, DC : New York: American Chemical Society ; American Institute of Physics for the National Institute of Standards and Technology, 1998. 2 pp. ISBN: 978-1-56396-831-0 978-1-56396-819-8 978-1-56396-820-4.

[105] R A Washington and S N Naldrett. "Preparation of Pure, Dry Iodine." In: *J. Am. Chem. Soc* 77.16 (Jan. 29, 1955), p. 4232. DOI: 10.1021/ja01621a020.

[106] Mark C. Biesinger et al. "Resolving surface chemical states in XPS analysis of first row transition metals, oxides and hydroxides: Sc, Ti, V, Cu and Zn." In: *Applied Surface Science* 257.3 (Nov. 2010), pp. 887–898. ISSN: 01694332. DOI: 10.1016/j.apsusc.2010.07.086.

[107] Mark C Biesinger et al. "Resolving surface chemical states in XPS analysis of first row transition metals, oxides and hydroxides: Cr, Mn, Fe, Co and Ni." In: *Applied Surface Science* 257 (2011), pp. 2717–2730. DOI: 10.1016/j.apsusc.2010.10.051.

[108] John A. Rotole and Peter M. A. Sherwood. "Aluminum Foil by XPS." In: *Surface Science Spectra* 5.1 (Jan. 1998), pp. 4–10. ISSN: 1055-5269, 1520-8575. DOI: 10.1116/1.1247850.

[109] Nirmal Kumar and Krishanu Biswas. "Cryomilling: An environment friendly approach of preparation large quantity ultra refined pure aluminium nanoparticles." In: *Journal of Materials Research and Technology* 8.1 (Jan. 2019), pp. 63–74. ISSN: 22387854. DOI: 10.1016/j.jmrt.2017.05.017.

[110] N. V. Alov. "Determination of the States of Oxidation of Metals in Thin Oxide Films by X-Ray Photoelectron Spectroscopy." In: *Journal of Analytical Chemistry* 60.5 (May 2005), pp. 431–435. ISSN: 1061-9348, 1608-3199. DOI: 10.1007/s10809-005-0114-x.

[111] M. Zier et al. "XPS investigations of thin tantalum films on a silicon surface." In: *Analytical and Bioanalytical Chemistry* 375.7 (Apr. 2003), pp. 902–905. ISSN: 1618-2642. DOI: 10.1007/s00216-003-1788-2.

[112] Mark C Biesinger et al. "X-ray photoelectron spectroscopic chemical state quantification of mixed nickel metal, oxide and hydroxide systems." In: *Surf. Interface Anal.* 41 (2009), pp. 324–332. DOI: DOI10.1002/sia.3026.

[113] Mark C Biesinger et al. "The role of the Auger parameter in XPS studies of nickel metal, halides and oxides." In: *Phys.Chem.Chem.Phys.* 14 (2012), pp. 2434–2442. DOI: 10.1039/c2cp22419d.

[114] Ziqin Yang et al. "XPS studies of nitrogen doping niobium used for accelerator applications." In: *Applied Surface Science* 439 (May 2018), pp. 1119–1126. ISSN: 01694332. DOI: 10.1016/j.apsusc.2017.12.214.

[115] J. Geyer-Lippmann, A. Simon, and F. Stollmaier. "Photoelektronenspektroskopie an Niobiodiden." In: *Zeitschrift fuer anorganische und allgemeine Chemie* 516.9 (Sept. 1984), pp. 55–66. ISSN: 0044-2313, 1521-3749. DOI: 10.1002/zaac.19845160909.

[116] Paul G. Shewmon. *Diffusion in solids*. 2.ed. Warrendale, Pa: Minerals, Metals & Materials Society, 1989. 246 pp. ISBN: 978-3-319-48564-5.

[117] Chelsie L Beck et al. "Molecular Iodine Interactions with Fe, Ni, Cr, and Stainless Steel Alloys." In: (2021), p. 8. DOI: https://dx.doi.org/10.1021/acs.iecr.0c04590.

[118] L. B. Parsons. "THE INFLUENCE OF WATER ON CERTAIN CHEMICAL REACTIONS. III. THE REACTIONS BETWEEN CERTAIN METALS AND IODINE." In: *Journal of the American Chemical Society* 47.7 (July 1925), pp. 1830–1835. ISSN: 0002-7863, 1520-5126. DOI: 10.1021/ja01684a007.

[119] Patrick Dietz et al. "Global models for radio-frequency ion thrusters." In: *EPJ Techniques and Instrumentation* 8.1 (Dec. 2021), p. 10. ISSN: 2195-7045. DOI: 10.1140/epjti/s40485-021-00068-5.